

Master Thesis

im Rahmen des
Universitätslehrganges „Geographical Information Science & Systems“
(UNIGIS MSc) am Zentrum für GeoInformatik (Z_GIS)
der Paris Lodron-Universität Salzburg

zum Thema

Roof surface classification with hyperspectral and laserscanning data An assessment of Spectral Angle Mapper and Support Vector Machines

vorgelegt von

Stephanie Brand
U1416, UNIGIS MSc Jahrgang 2008

Zur Erlangung des Grades
„Master of Science (Geographical Information Science & Systems) – MSc(GIS)“

Gutachter:
Ao. Univ. Prof. Dr. Josef Strobl

München, 31.03.2011

Danksagung

Hiermit möchte ich mich bei allen bedanken, die mir bei dieser Masterarbeit geholfen und mich unterstützt haben, insbesondere bei Dr.-Ing. Uwe Weidner vom Karlsruher Institut für Technologie, Institut für Photogrammetrie und Fernerkundung, für die Betreuung, Diskussion und Bereitstellung des Datenmaterials

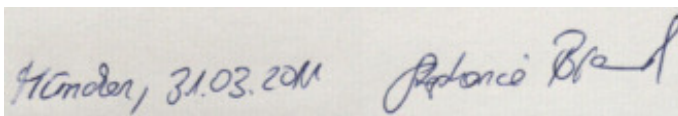
Eidesstattliche Erklärung

Paris Lodron-Universität Salzburg

Zentrum für GeoInformatik (Z_GIS)

Universitätslehrgang „Geographical Information Science & Systems“ (UNIGIS MSc)

"Ich versichere, diese Master Thesis ohne fremde Hilfe und ohne Verwendung anderer als der angeführten Quellen angefertigt zu haben, und dass die Arbeit in gleicher oder ähnlicher Form noch keiner anderen Prüfungsbehörde vorgelegen hat. Alle Ausführungen der Arbeit die wörtlich oder sinngemäß übernommen wurden sind entsprechend gekennzeichnet."



Hörsden, 31.03.2011 *Antonci Brand*

(Ort, Datum)

(Unterschrift der Studentin)

Kurzfassung

Städtische Gebiete sind durch eine Vielzahl verschiedenster Materialien gekennzeichnet. In diesem Kontext haben sich hyperspektrale Datensätze für die Klassifikation von urbanen Materialien bewährt. In dieser Arbeit wird mit Hilfe eines hyperspektralen Datensatzes eine detaillierte Karte von Dachmaterialien erstellt.

Zwei pixel-basierte Klassifikatoren werden miteinander verglichen. Dies ist zum einen der Spectral Angle Mapper, der gut geeignet ist um urbane Gebiete zu klassifizieren, weil er als insensitiv gegenüber Beleuchtungsunterschieden gilt, die gerade im urbanen Raum groß sein können. Zum anderen werden Support Vector Machines verwendet. Dies ist ein nicht-statistischer Klassifikator, der die Klassengrenzen durch Trennebenen bestimmt. Da er gut geeignet ist für hoch-dimensionale Datensätze und kleine Trainingsbiere, Bedingungen, die in dieser Studie erfüllt sind, wurde er ausgewählt.

Eine binäre Dachmaske aus Laserscanner-Daten wird benutzt um Gebäude von Boden zu unterscheiden. Damit soll die Verwechslung zwischen Materialien aus dem Bodenbereich und denen auf Dächern vermieden werden. Dieses Vorgehen wird durch Einbinden der Dachneigung ergänzt. Es wurden zwei Masken, die eine für geneigte, die andere für flache Dachoberflächen aus einem pixel-basierten Neigungsdatensatz aus Laserscanner-Daten hergeleitet. Der Gedanke dahinter ist, dass einige Materialien ähnliche Spektralkurven aufweisen und daher im Klassifikationsprozess schwer zu unterscheiden sind. Dies sind oft Materialien mit niedriger Reflexion und keinen nennenswerten Absorptionsbanden, die aber auf Dächern mit unterschiedlicher Neigung vorkommen. Da es sich während der Arbeit herausgestellt hat, dass die Laserscanning-Maske einige Fehler in den Neigungswerten enthielt, wurden die Klassifikationen mit einer manuell-erstellten Maske erneut durchgeführt. Es konnte gezeigt werden, dass durch die Einführung von Dachneigung die Verwechslung von Materialien, z.B. von Schiefer und Bitumen-Dachpappe, reduziert und die Gesamtgenauigkeit der Klassifikation damit verbessert werden kann. Der Vergleich zwischen den beiden Klassifikationsmethoden wird zum einen visuell, als auch quantitativ mit Hilfe von Konfusionsmatrizen durchgeführt. Beide Klassifikatoren erwiesen sich als gut geeignet um Dachmaterialien zu klassifizieren. Der Spectral Angle Mapper hat dabei im Vergleich mit den Support Vecotr Machines die besten Resultate erzielt, sowohl für die Klassifikation mit, als auch ohne Dachneigung.

Abstract

The urban environment is characterised by a variety of different surface materials. In this context, hyperspectral datasets have proved well suited for urban material mapping. In this study, a detailed map of roof materials is created using a hyperspectral dataset from the HyMap sensor.

Two pixel-based classifiers are used for this task and their results compared. Spectral Angle Mapper, the first classification method, is well suited for the classification of urban areas because of its insensibility to illumination changes, which are high for urban areas. Support Vector Machines are the second classification method used. It is also a non-statistical classifier which determines separating planes between the classes and has been proved to work well with high-dimensional datasets and small training classes, both conditions being fulfilled in this study.

A binary roof mask created from laserscanning data is used to distinguish buildings from non-buildings to reduce the confusion between materials on the ground and on the roofs. This approach is extended by a second step in which inclination information of the roofs is incorporated in the process. Two masks, one for flat roofs, the other for inclined roofs from a pixel-based inclination dataset are derived from laserscanning data. The idea behind this is, that some materials show similar reflectance curves and are therefore hard to distinguish in the classification process. These are materials with low reflectance and no distinct absorption features, but which occur on roofs with different inclination. As the laserscanning mask showed some errors in inclination values, the classifications were repeated with manual inclination masks. When introducing inclination, it can be shown that the confusion e.g. between slate and bitumen roofs, can be reduced and thus the overall accuracy improved.

The comparison between the two classification approaches, as well as between the results for the classification with and without roof inclination is done visually and quantitatively with confusion matrices. Both classifiers have proved suitable for the classification of roof materials. The Spectral Angle Mapper provided the best classification results in comparison with Support Vector Machines for the classification with and without roof inclination.

Contents

	Seite
<i>Danksagung</i> _____	<i>i</i>
<i>Eidesstattliche Erklärung</i> _____	<i>ii</i>
<i>Kurzfassung</i> _____	<i>iii</i>
<i>Abstract</i> _____	<i>iv</i>
<i>Contents</i> _____	<i>v</i>
<i>List of figures</i> _____	<i>vii</i>
<i>List of tables</i> _____	<i>ix</i>
<i>Abbreviations</i> _____	<i>x</i>
1 Introduction _____	1
2 Fundamentals _____	5
2.1 Fundamentals of imaging spectrometry _____	5
2.1.1 Electromagnetic radiation _____	5
2.1.2 Interactions with the atmosphere _____	6
2.1.3 Surface material reflectance _____	7
2.2 Challenges of urban surface classification _____	11
2.3 Classification concepts _____	15
2.3.1 Spectral Angle Mapper _____	17
2.3.2 Support Vector Machines _____	18
3 Methodology _____	24
3.1 Study Area _____	24
3.2 Data basis _____	25
3.2.1 The HyMap sensor _____	25
3.2.2 Laserscanning data _____	27
3.2.3 Aerial imagery _____	27
3.3 Reference data _____	28

3.3.1	Spectral characteristics of the roof materials	28
3.3.2	Development of the reference dataset	31
3.4	Workflow of processing steps	33
3.4.1	Preparation of data	33
3.4.2	Selection of training areas	40
3.4.3	Workflow of image classification	42
3.4.4	Validation concept	46
4	Results	50
4.1	Classification results without roof inclination	50
4.1.1	SAM	50
4.1.2	SVM	54
4.1.3	Visual Comparison	57
4.1.4	Quantitative comparison	60
4.2	Classification results with roof inclination	62
4.2.1	SAM	62
4.2.2	SVM	64
4.2.3	Improvement of slope mask	66
4.2.4	Visual Comparison	67
4.2.5	Quantitative comparison	68
5	Summary and conclusions	72
	Literature	75
	Appendices	82
A.	Classification results	83
B.	Statistics of classification results	89
C.	Confusion matrices of classification results	92

List of figures

Figure 1: Atmospheric windows (source: Lillesand & Kiefer, 1994).....	7
Figure 2: Principle components of at-sensor-radiance.....	8
Figure 3: Spectral reflectance curves for vegetation, bare soil and water	9
Figure 4: Reflectance spectrum of roofing copper.....	10
Figure 5: Differences in building sizes	12
Figure 6: Examples of roof structures.....	12
Figure 7: Shadow and its influence on the spectral signature of a gravel roof.....	12
Figure 8: Graphs of different reflectance curves extracted from the HyMap image	13
Figure 9: Concept of mixed pixels.....	16
Figure 10: Plot of a reference spectrum and test spectrum for a two-band image (source: Kruse, et al., 2003, p.157).	18
Figure 11: The classification hyperplane	21
Figure 12: Classification of the non-separable case.....	21
Figure 13: HyMap true colour composite of the study area and its location in Karlsruhe	24
Figure 14: Detail from aerial photo.....	28
Figure 15: Roof spectra in the study area.....	29
Figure 16: Reference dataset (yellow) with hyperspectral colour composite image in the background.....	32
Figure 17: Vector reference dataset with roof surface materials	33
Figure 18: Signal-to-noise ratio of a patch of grass	34
Figure 19: Hyperspectral dataset (band combination 15/9/3) with the main campus area marked in yellow (left). Enlarged detail (right)	35
Figure 20: Initial binary building mask including non-building objects.....	36
Figure 21: Hyperspectral dataset with pixel NDVI > 0.5 marked in green.	36
Figure 22: Final roof mask.....	36
Figure 23: Final hyperspectral dataset with roof mask applied (hyperspectral band combination 15/9/3).	37

Figure 24: classified map of flat and inclined roofs.....	39
Figure 25: Final masks of flat and inclined roofs	39
Figure 26: Location of training areas of the roof materials	41
Figure 27: Spectral reflectance curves of all training areas (mean of the pixel values per area).....	42
Figure 28: Flowchart of SAM classification.....	43
Figure 29: Flowchart of SVM classification.....	45
Figure 30: Flowchart of classification workflow with roof inclination	46
Figure 31: Detail of the reference dataset with the training areas clipped.....	47
Figure 32: Model in ArcGIS for the calculation of the data basis for the confusion matrix	48
Figure 33: SAM classification examples (angle 0.5 rad).....	52
Figure 34: Wrong classification of pixels on aluminium roofs (SAM, angle 0.5 rad). For the legend, refer to figure 32	53
Figure 35: Example of overfitting of the training data.	55
Figure 36: SVM classification examples	56
Figure 37: Visual comparison of SAM and SVM classification of selected roofs	58
Figure 38: Example of wrongly classified roof border pixels.	58
Figure 39: Different reflectance signatures of an aluminium roof leading to wrong class assignment.....	59
Figure 40: Improvement of the classification due to inclination	63
Figure 41: Effects of inclination mask on the classification	64
Figure 42: Comparison of a detail of the classification with and without inclination. ...	66
Figure 43: Manual inclination mask	67

List of tables

Table 1: The wavelength bands of electromagnetic radiation	6
Table 2: System parameters of HyMap (source: HyVista, 2011)	26
Table 3: Spectral configuration of HyMap (source: HyVista, 2011).....	26
Table 4: Acquisition information of the HyMap scene.....	26
Table 5: Acquisition information for the aerial imagery	28
Table 6: Characteristics of the training areas	41
Table 7 : Angles used in the SAM classification	51
Table 8 : Overall accuracy for SAM and SVM result.....	60
Table 9 : Producer's accuracy of the classes for SAM and SVM.....	61
Table 10 : Overall accuracy for SAM and SVM result in comparison with and without inclination information for the roofs	69
Table 11 : Comparison by class of producer's accuracy (in %) (with and without inclination)	70
Table 12: Comparison by class of user's accuracy (in %) (with and without inclination).	70

Abbreviations

ANN	Artificial Neural Network
ArcGIS	Product family of GIS software by ESRI
ATCOR	Atmospheric and Topographic Correction
CEST	Central European Summer Time
CV	Cross-validation
DAIS	Digital Airborne Imaging Spectrometer
DIN	German Institute for Standardization
DLR	German Aerospace Center
DSM	Digital Surface Model
ENVI	Environment for Visualisation of Images
ESRI	Environmental Systems Research Institute, Inc.
FOV	Field of view
GIFOV	Ground instantaneous field of view
GIS	Geographical Information System
GPS	Global Positioning System
	Hyperspectral Digital Imagery Collection
HYDICE	Experiment
HyMap	Hyperspectral Mapper
IDL	Interactive Data Language
IFOV	Instantaneous field of view
IPF	Institute for Photogrammetry and Remote Sensing
ITT VIS	ITT Visual Information Solutions
KIT	Karlsruhe Institute of Technology
LIBSVM	A library for Support Vector Machines
NDVI	Normalized difference vegetation index
NIR	near infrared
rad	radians
RBF	Gaussian radial basis function
ROI	Region of interest
SAM	Spectral Angle Mapper
SFF	Spectral Feature Fitting
SID	Spectral Information Divergence
SNR	Signal-to-noise ratio
SV	support vectors
SVM	Support Vector Machine
SWIR I	Short wave infrared I
SWIR II	Short wave infrared II
TM	Thematic Mapper
VIS	Visible part of the electromagnetic spectrum
VLW	Amt für Vermessung, Liegenschaft und Wohnen

1 Introduction

Imaging Spectrometry or hyperspectral imaging as it is also termed (Goetz, et al. 1985), started in the late 1970s to early 1980s. It is concerned with the measurement and analysis of reflectance spectra collected in many small, contiguous spectral bands (Goetz, 2009). Since then, imaging spectrometry has proved useful in a range of applications. The earliest studies focussed on geology, and have since demonstrated to be an effective means for the mapping of minerals, rocks and soils (Crowley, 1993; Van der Meer, 1996; Chabrilat, et al. 2002). Hyperspectral data have also been used in ecological and vegetation studies, e.g. for the mapping on a species level (McMorrow, et al., 2004; Xiao, et al., 2004; Middleton, et al., 2009). Spectrometry has not only been applied for natural materials, but also for man-made materials in an urban environment. There are studies focussing on the spectral curves of urban materials, for example the build-up of spectral libraries (Ben-Dor, et al. 2001; Herold, et al., 2004), or the analysis of the spectral reflectance curve (Moreira & Galvao, 2010; Heiden, et al., 2007; Van der Meer, 2004), as well as factors influencing the appearance of urban features, such as different illumination and sensor viewing-angles (Meister, et al., 2000; Schiefer, Hostert and Damm, 2006; Lacherade, et al., 2005).

In this study, roof surfaces in the city of Karlsruhe, Germany, are mapped using different classifiers. Before classification is performed, the reflectance curves of different roof surfaces and the factors influencing them are analysed. The knowledge of roof surfaces, their materials and distribution in a city can be of great value for a range of applications like studies of the urban heat island effect. One parameter of this effect, i.e. the phenomenon that urban areas have higher temperatures than their surrounding rural areas, is the surface albedo in the city (Taha, 1997). A large quantity of this is contributed by roofs, as the roof temperature is determined in large parts by the heat emission into space (Berdahl and Bretz, 1997). As a second example, a study on the deposition of contaminants in urban areas from roof water run-off has shown the usefulness of roof classification for the input into models describing the deposition of contaminants in urban areas. (Weidner, et al. 2005).

This study's main task is the assessment of the ability of two different pixel-based classifiers to map roof surfaces: Spectral Angle Mapper (SAM) and Support Vector Machines (SVM). The high number of bands in hyperspectral imagery has led to the development of different classification techniques other than the traditional methods of supervised classification such as the Maximum-Likelihood algorithm, which is not suited without reducing dimensionality first. Therefore, classifiers were developed which are able to deal with the high dimensionality of hyperspectral data. Various classifiers have been used in connection with hyperspectral data such as spectral unmixing (Roessner, et al., 2001), artificial neural networks (Subramanian, et al. 1997) or decision trees (Mather & Pal, 2003; Wang & Li, 2008), to name but a few. The classifier SAM was chosen because it has proved to be insensitive to illumination effects and is therefore well suited for the urban environment where large variations in illumination occur (Hostert, 2010). It has been used e.g. in a study to map the surface mineralogy of a region in Israel (Ben-Dor & Kruse, 1995), for the mapping of semi-arid landscapes (Yuhas, et al., 1002), but also in urban environments for the mapping of roof materials to assess their vulnerability for hailstorms (Bhaskaran, et al., 2001). In both cases SAM gave good classification results.

SVM is a more recent classifier that has been reported to give better classification accuracies than other classifiers. Huang, et al., (2002) compared the performance of SVM, Decision Tree classifier, Artificial Neural Networks and Maximum Likelihood for land cover classification with a multi-spectral dataset of Landsat TM. Dixon & Cancade (2008) compared Neural Networks and SVM for land-use classification also using Landsat TM. And Pal & Mather (2004) assessed SVM for the classification of land cover in comparison with Maximum Likelihood and Artificial Neural Networks using a DAIS hyperspectral dataset. A higher level of classification accuracy was achieved for the classification with SVM, even with hyperspectral datasets. Therefore, SVM was chosen as second classifier for this comparison to assess the accuracy in the classification of roof surfaces.

Various studies in the urban environment have also used height information, e.g. digital elevation data, to enhance classification by reducing spectral confusion between urban land cover types (Herold & Roberts, 2010). This way, a third dimension is introduced to the study. Gamba & Houshmand (2000) used AVIRIS and IFSAR data for a 3D profile

reconstruction of buildings. The hyperspectral data were used to differentiate between vegetated and non-vegetated surfaces, thus improving the building reconstruction. Greiwe, et al. (2004) used segment-based fusion of high spatial and high spectral resolution image data (digital orthophoto, HyMap hyperspectral data and a DEM from airborne photography) to classify an urban environment. A similar approach of one part of this study is the survey of Madhok & Landgrebe (1999) who fused HYDICE hyperspectral data and a DEM obtained from airborne photography. They identified and delineated building roof-tops, thereby using the hyperspectral data for the identification and the height information to discriminate roof and ground. In a study by Lemp & Weidner (2005), inclination information on roofs from a laserscanning dataset was included in a segment-based classification process of roof surfaces using the same hyperspectral data. They proved that the incorporation of inclination information leads to an improvement of accuracy. While they used a segment-based classification approach, this study assesses two pixel-based methods to see whether the accuracy can be improved for SAM and SVM results as well by incorporating the inclination of roofs.

This leads to the following topics and questions of this case study which shall be answered:

- A detailed analysis of the **spectral signatures of roof types** in the hyperspectral image will be given, including the collection of various roof surfaces apparent in the HyMap dataset.
- Classification of roof surfaces on a subset of the HyMap dataset of Karlsruhe is performed using the **Spectral Angle Mapper** classifier and **Support Vector Machines**. The classification results will be assessed. Which classifier leads to the best classification result?
- **Roof inclination information** of laserscanning data is incorporated in the classification process. Can this approach improve the accuracy of the classification results?

For data preparation and the classification of Spectral Angle Mapper, the software ENVI 4.7 (Environment for Visualisation of Images) by ITT VIS was used. For the SVM classification, the package “libSVM” was applied which can be used within

ENVI. The development of the reference dataset and the validation of results was performed with the software ArcGIS 9.3.1 by ESRI.

This study is structured as follows: In the first chapter, an introduction to imaging spectrometry is given explaining its fundamentals, and the challenges of urban surface classification on the basis of hyperspectral datasets are analysed. In addition, the theoretical concepts of the two classifiers SAM and SVM are illustrated. The next chapter deals with the description of the methods, from data preparation to the implementation of the classifications and the validation methods used. In addition, the set-up of the reference dataset for accuracy assessment is described, including the description of the reflectance of roof surfaces in the image. In chapter 4, the classification results are presented and analysed by visual and quantitative comparison with the reference dataset using confusion matrices. Finally, a conclusion of the study is given and an outlook to further possible studies provided.

2 Fundamentals

The chapter provides information on the fundamentals of passive remote sensing which are relevant for understanding the principles behind hyperspectral spectrometry. In the following, the characteristics of urban landscapes are discussed. The chapter finishes with the concepts of the classification of hyperspectral data and the two classifiers assessed in this study.

2.1 Fundamentals of imaging spectrometry

Hyperspectral spectrometers allow for the discrimination of features using their distinct absorption and reflection characteristics. They are termed “hyper”spectral because they contain many contiguous bands (often up to 200 bands) in which they record the object’s reflectance across the electromagnetic spectrum. The basic physical and radiometric properties of spectrometry will be explained in the following paragraphs to understand how the reflectance of objects can be measured and how information on objects can be derived from it. Unless otherwise cited, these principles of Remote Sensing are taken from textbooks by Lillesand and Kiefer (1994), Mather (1996) and Campbell (1996).

2.1.1 Electromagnetic radiation

In passive optical Remote Sensing, the source of emitted electromagnetic radiation is the Sun. The amount of radiation reflected depends on the properties of the objects on the ground. Active Remote Sensing uses radiated energy to derive information from the Earth (e.g. radar and laserscanning systems). The concept of laserscanning used in this study to derive information on the geometric properties of the roofs, is described in chapter 3.2.2.

Electromagnetic radiation that is emitted from the sun, travels at the speed of light, passes through the atmosphere and is reflected by the Earth’s surface. It is composed of a range of wavelengths. The wavelength ranges are displayed in Table 1 . Wavelength is usually measured in micrometers (μm) or nanometer (nm).

range	wavelength (μm)
Visible range (VIS)	
Blue	0.4 – 0.5
green	0.5 – 0.6
red	0.6 – 0.7
Near-infrared (NIR)	0.7 – 1.3
Short-wave infrared (SWIR)	1.3 – 3.0

Table 1: The wavelength bands of electromagnetic radiation
(source: Lillesand & Kiefer, 1994)

2.1.2 Interactions with the atmosphere

On the way through the atmosphere, radiation is influenced by atmospheric gases and particles causing absorption and scattering effects which mainly influence the intensity and direction of electromagnetic radiation within the atmosphere.

Scattering is the result of interactions between electromagnetic radiation and gas molecules or particles in the atmosphere. The radiation that is scattered from these particles or molecules is redirected or deflected from its path. There are two different scattering mechanisms: Rayleigh-scattering is caused by particles with diameters that are small relative to the wavelength of radiation and is therefore wavelength dependent. Rayleigh-scattering is inversely proportional to the fourth power of the wavelength, which means that it influences shorter wavelengths more than longer wavelengths. Mie-scattering is caused by larger particles (e.g. water vapour, dust or pollen) in the atmosphere and it influences the wavelengths with the same size as the particle itself. Non-selective scattering is produced by particles which are larger than the wavelengths, such as large water droplets. All wavelengths are affected equally, generating a sort of haze to the image.

The atmosphere also absorbs electromagnetic radiation. Responsible for this are gases like water vapour, carbon dioxide, ozone or aerosols which absorb radiation in specific regions of the electromagnetic spectrum. The major water vapour absorption bands are at around $0.94\mu\text{m}$, $1.14\mu\text{m}$, $1.38\mu\text{m}$ and $1.88\mu\text{m}$, the oxygen band at around $0.76\mu\text{m}$ and carbon dioxide bands near $2.01\mu\text{m}$ and $2.08\mu\text{m}$ (Van der Meer, 2001). Other trace

gases like ozone, are included as well as they also produce absorption bands in the range of 0.4 μm to 2.5 μm . The spectral regions which are not subject to strong absorption and where transmission of radiation is high, are termed “atmospheric windows” (see Figure 1). In these windows enough radiation is reflected to be effectively recorded by a sensor. This is why imaging spectrometers are specifically designed to use these windows.

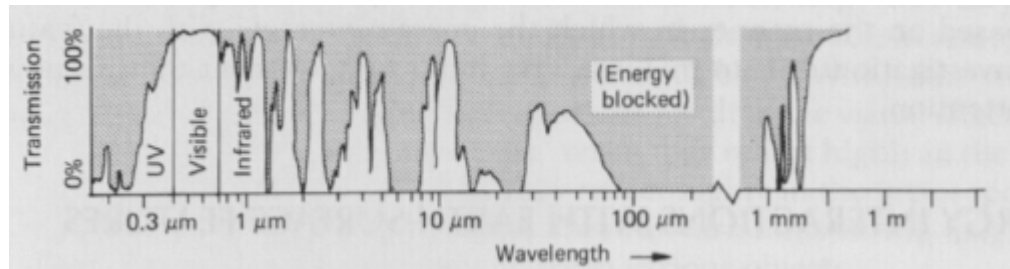


Figure 1: Atmospheric windows (source: Lillesand & Kiefer, 1994)

2.1.3 Surface material reflectance

As described above, radiation incident on the Earth is reflected, absorbed or transmitted. The interrelationship between these interactions can be formulated as follows (energy balance equation):

$$E_I(\lambda) = E_R(\lambda) + E_A(\lambda) + E_T(\lambda) \quad (1)$$

Where E_I is the incident energy, E_R the reflectance, E_A the absorbance and E_T the transmittance. All energy components are a function of wavelength λ . The reflectance is thus: $E_R(\lambda) = E_I(\lambda) - (E_A(\lambda) + E_T(\lambda))$ (2)

The characteristics and nature of objects can be inferred from the spectral response. This is possible because each material has a characteristic manner of interacting with the incident radiation. This is the fundamental concept behind spectrometry and the analysis of spectral reflectance curves of target materials or objects. However, the spectral response of a target not only depends on its properties but also on factors like solar azimuth, solar elevation angle and sensor characteristics.

The hyperspectral sensor records the energy emitted from a target, but as the solar irradiance interacts with the atmosphere, the recorded signal is contaminated. The

energy that is recorded by the sensor, is called at-sensor-radiance. Figure 2 displays the components of the measured at-sensor-radiance. It is the sum of radiance reflected from the surface (I_S), radiation scattered in the atmosphere which reaches the sensor without reaching the surface first (I_O) and diffuse radiation which is directed to the surface, then the atmosphere, then to the sensor (I_D). The components are wavelength (λ) dependent. This can be written as:

$$I = I_S(\lambda) + I_O(\lambda) + I_D(\lambda) \quad (3)$$

While I_S varies with different factors like the surface properties (roughness, texture), and orientation of the object to the sensor, I_O is nearly constant. I_D varies with the surface but is relatively small. One special case and an important factor in urban areas, is shadow. The radiance reflected from the surface I_S is null because no direct solar radiation reaches these areas, but some brightness is still derived from I_D resulting in low reflectance of shadowed areas.

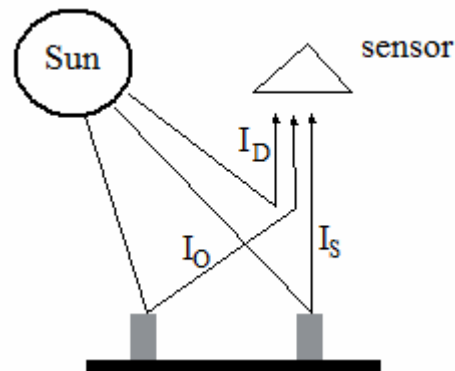


Figure 2: Principle components of at-sensor-radiance.
 I_S = reflected surface radiation, I_O = atmospheric radiance, I_D =
diffuse radiance

The amount of radiation recorded is thus dependent on properties of the surface, solar characteristics and the atmosphere. For spectrometry, the radiance values need to be converted to apparent reflectance, and atmospheric effects need to be corrected for. This is done by simulating the influence of the solar characteristics and the atmosphere and by applying certain algorithms. The resulting reflectance is the proportion between emitted to incident radiance.

After removing the atmospheric influences, the reflectance signal is ideally only influenced by the properties of the surface material (Van der Meer, 2001). Every material has certain specific reflectance properties due to the composition of its atoms and molecules. Depending on the material, the emitted energy is reduced in certain wavelengths due to the interaction of photons of the electromagnetic radiation in the crystal lattice. For the shorter wavelengths, these interactions are due to the change of energy state of electrons, for longer wavelengths, due to the excitement of certain oscillation states. The attenuation of certain wavelengths is visible as absorption bands in the spectral curves of an object. Figure 3 displays the typical spectral reflectance curves for vegetation, bare soil and water. Vegetation shows the highest reflectance with 3 main deep absorption features and a very distinct spectral curve. Bare soil is an example of a more uniform spectral curve with few and only small absorption bands. Water has a very low reflectance in the blue part of the electromagnetic spectrum. The energy is nearly fully absorbed in the infrared wavelengths.

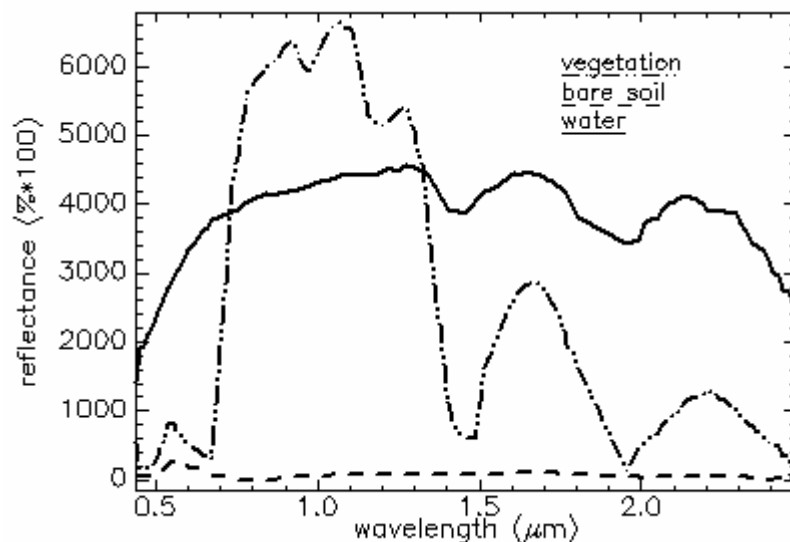


Figure 3: Spectral reflectance curves for vegetation, bare soil and water

To analyse the spectral properties of materials, spectral libraries which include many reflectance spectra, can be built from field or laboratory measurements or from the hyperspectral image. Examples for spectral libraries are the USGS Spectroscopy Lab Spectral library (Clark, et al., 1993) or the Aster spectral library (Baldrige, et al., 2008) containing natural and man-made materials. For urban studies, spectral libraries

were also built (Herold, et al., 2004; Ben-Dor, Levin & Saaroni, 2001; Heiden, et al., 2007).

Exemplarily, the reflectance spectrum of roofing copper is displayed in Figure 4, along with the same material spectrum from a multispectral system to emphasize the strength of a hyperspectral spectrometer for material mapping. It can be seen that the hyperspectral reflectance curve carries more information content and delivers a more detailed reflectance curve for the material than the reflectance curve of the same material recorded by Landsat TM with only a few bands. Characteristic absorption bands can be seen in the hyperspectral curve where they are not visible in the multispectral reflectance curve. This makes it possible for spectrometers to not only distinguish object classes like vegetation, water or build-up area, but different materials.

The challenges to distinguish materials in an urban environment together with spectral curves of roof materials contained in this study, are explained in the next chapter.

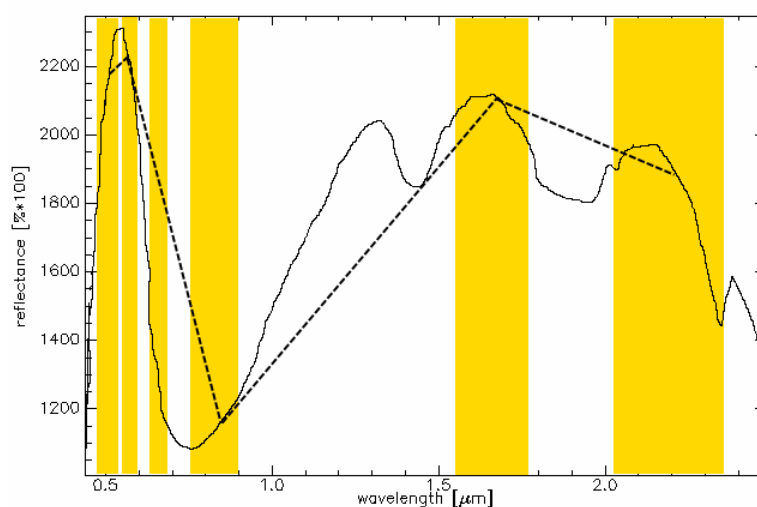


Figure 4: Reflectance spectrum of roofing copper as it would be recorded by hyperspectral data (solid line) and by Landsat TM (dashed line). The Landsat bands are displayed in orange.

2.2 Challenges of urban surface classification

The urban environment is characterized by various types of different materials, natural and man-made, which lead to very heterogeneous reflecting surfaces. A variety of different building sizes, roof geometries and roads can be found, as well as vegetated areas in form of parks, street trees or gardens and recreational zones. This multitude of materials provides a challenge for urban mapping.

Generally, material mapping can be done using the reflectance signature of objects. The reflectance curve is strongly dependent on surface materials and their material composition, but it can also be influenced by other factors. These factors and the general characteristics of urban areas, which are encountered when classifying hyperspectral images, are described in the following chapter.

Urban areas show a strong change in **different surface materials in a small space**. A spatial resolution of finer than 5m for urban case studies is recommended (Small, 2003). However, the resolution still makes it very likely that the pixels of a hyperspectral image include more than one object or material and are therefore mixed pixels containing spectral information of different materials. In this study, roof surfaces shall be mapped with a hyperspectral image of 4m spatial resolution. Figure 5 shows a detail of the campus area and adjacent residential expanses. The different roof sizes are clearly distinguishable. In the residential area, the buildings are directly adjoining and the borders of roofs can not be easily made out with the 4m resolution of the hyperspectral image. The campus area has larger buildings and therefore large roof areas. However, the roofs themselves are not uniform but contain additional roof structures like chimneys, roof windows or ventilation tubes (Figure 6) . This means that great care has to be taken when selecting representative training areas for the different roof surfaces.

Another factor is the amount of **shadow** which is very high in urban areas and presents a problem as in most cases the spectral signature of a shadowed material does not resemble the material signature anymore. Figure 7 displays the effect of shadow on a spectral signature of a gravel roof. Some brightness is still derived from diffuse radiation in shadowed areas but reflectance is low. The shadowed roof also shows a different shape of the spectral curve compared to an illuminated gravel roof.



Figure 5: Differences in building sizes

Large roofs on the campus ground in the Northern part of the image; small, heterogeneous roof types of the residential area South of the campus (true colour composite of HyMap image left, aerial photo right; size of detail appr. 390m x 370m)



Figure 6: Examples of roof structures

(true colour composite of HyMap image on the left, aerial photo on the right, respectively)

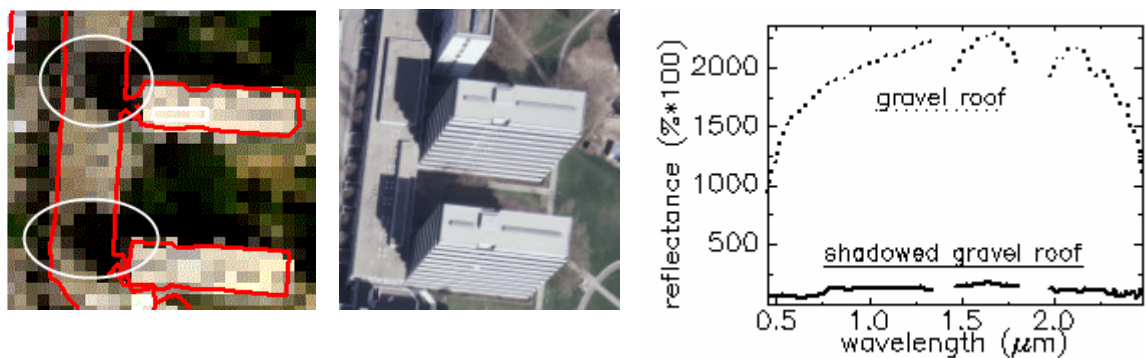
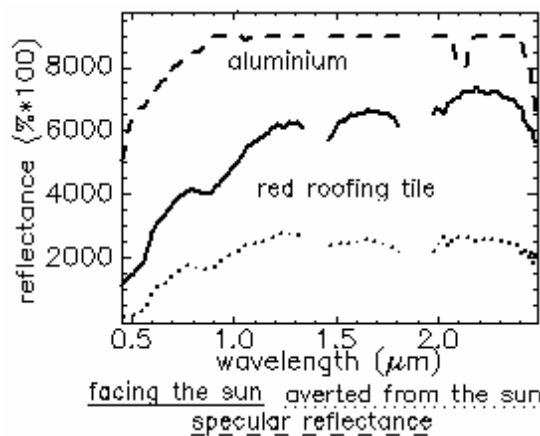


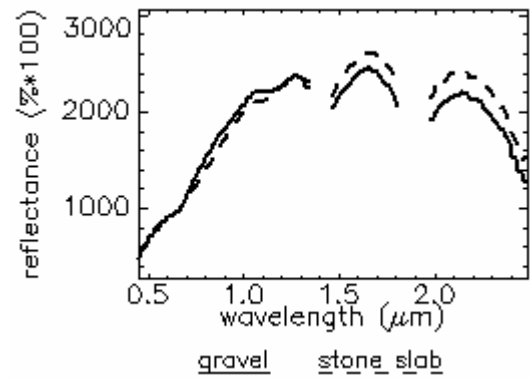
Figure 7: Shadow and its influence on the spectral signature of a gravel roof

Left: Shadow in HyMap image (marked with white circle). Middle: same detail from aerial photo;
Right: spectral signature of illuminated and shadowed gravel roof

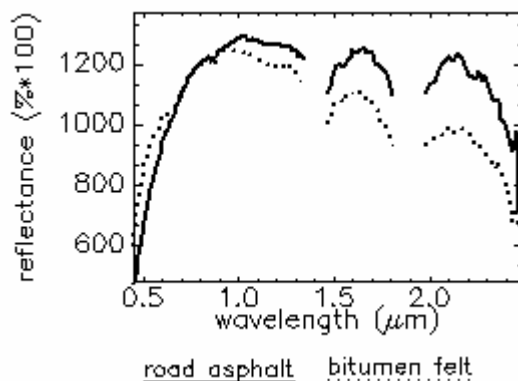
Related to the problem of shadow in urban areas are the **different solar illumination conditions** in combination with the viewing-angle of the sensor and their influence on



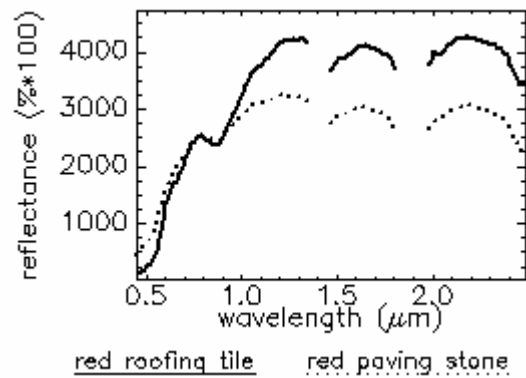
a) Influence of different illumination conditions



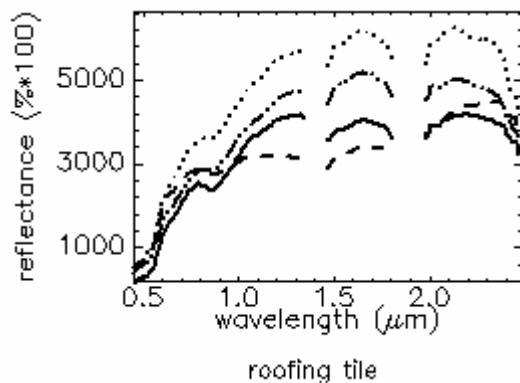
b) Similar spectral signatures of roof surfaces



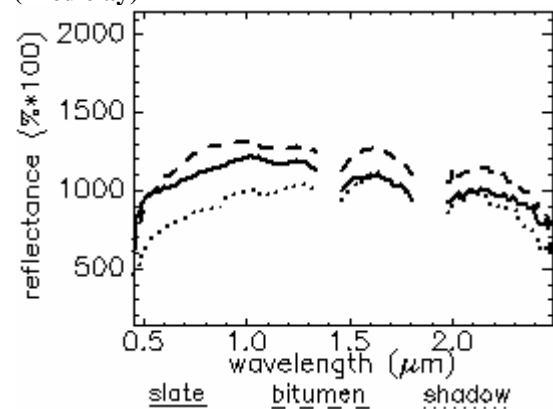
c) Similar spectral signatures of materials on the roof and ground (bitumen)



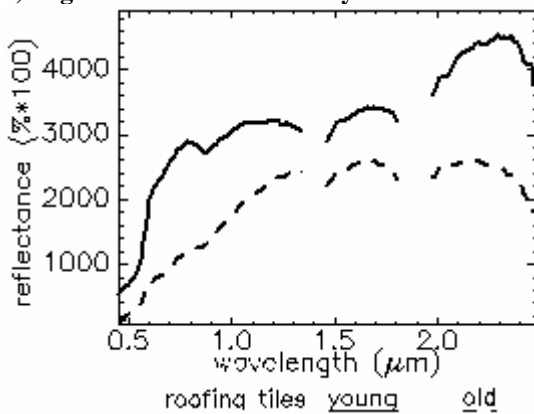
d) Similar spectral signatures of roof surfaces (fired clay)



e) High within-class variability



f) Roofs with low reflectance



g) Reflectance of a roof surface of different age

Figure 8: Graphs of different reflectance curves extracted from the HyMap image

the reflectance of urban objects. The brightness of the reflectance changes, as can be seen in Figure 8a for a tiled roof where one roof area is facing the sun, the other is averted from it. The absorption features do not change in this case. Therefore, the geometry of a roof and the location of the building in the image also play a role in the reflectance. Some materials like glass and metal roofs occasionally show specular reflectance which changes the spectral signature of a material and, as in the example of Figure 8a for an aluminium roof, also exceed the sensor capabilities. A classification of this kind of roof might therefore prove difficult.

Urban areas are also characterized by objects of the same basic material, thus showing **similar spectral reflectance curves**. These can be objects of identical utilization like roofs shown in Figure 8b. Both roof surfaces contain the same basic material which is natural stone, crushed to gravel or in the form of stone slabs. Due to the similarity of materials they also show similar reflectance curves. The same effect can be seen for objects of different uses as in Figure 8c and d for roof as well as ground materials. The bitumen felt of a roof and asphalt on the road show similar spectral characteristics, especially in the visible part of the electromagnetic spectrum. Their reflectance is low (around 12%) and their reflectance curves have relatively uniform shapes. Both surface materials contain bitumen, a residue from the distillation of oil (Wormuth, Dierks and Fleischmann, 2007). Further examples are red roofing tiles and red paving stone. They are made from fired clay and show a distinct absorption feature at $0.85\ \mu\text{m}$ and a small reflectance peak in the visible range at $0.78\ \mu\text{m}$.

Some spectral signatures of urban surfaces possess distinct absorption bands that cannot be found in other features, thereby making them easier recognizable by classifiers. On the other hand there are surfaces which do not show spectral variations of large degrees. Signatures showing a near **constant and low reflectance** without broad absorption features and therefore may easily be confused with shadow (Figure 8f).

Finally, surfaces of the same material can show **spectral modifications** due to different age, condition and coating. The influence of age is shown in Figure 8g. Displayed are two spectral samples of red roofing tiles, one from an older roof, the other from a younger one. It can be seen that the reflectance curve of the older material changed, losing the distinct absorption band at $0.87\ \mu\text{m}$ (absorption due to iron oxide) which

would be typical of fired clay. Additionally, the young roofing tile still shows a rise in reflectance in the SWIR associated with the loss of water during the firing process which is not lower for older tiles. For aged gravel or stone slab roofs the overgrowth with lichen or grass is typical. This would also change reflectance. All these influences lead to a high within-class variability, as is shown in Figure 8e for red roofing tiles.

All the described factors typical for spectrometry of urban areas might lead to some confusion between classes of roof materials. To avoid at least the confusion between similar materials on the roof and on the ground, a roof mask is used in this study. The HyMap image is clipped so that only the roofs are displayed which are then used for classification. However, similar reflectance curves of roof materials might still complicate classification (see chapter 3).

2.3 Classification concepts

There are many possible classification methods in literature which are used for the mapping of landcover. The choice of classifier can depend on different factors such as the dataset used, the level of detail to be mapped and the characteristics of the thematic classes.

The traditional supervised classification methods for multispectral data are multivariate statistical classifiers like e.g. Maximum Likelihood. Each pixel represents a point in n -dimensional feature space (n being the number of bands). Its location depends on its spectral reflectance in each band. Points close together in feature space would be assigned to the same class. Maximum Likelihood calculates the probability that a given point in feature space belongs to a specific class. It requires that certain statistical characteristics of each class like mean and covariance matrix are derived from training classes. The problem for statistical classifiers in high-dimensional feature space is that the number of training samples is relatively small compared to the number of features, which can lead to singular covariance matrices when the number of training samples is below one more than the number of features.

The higher the number of features the more parameters need to be estimated. This is called the Hughes phenomenon which states that classification accuracy declines as the number of features increases, because the reliability of estimates of statistical parameters decreases (Landgrebe, 1999; Mather & Koch, 2011, Pal & Mather, 2005). Therefore, statistical classifiers can only be used when dimensionality of hyperspectral data is reduced first.

Some classifiers for hyperspectral data make use of the physical information of the spectrum, comparing absorption features to known class spectra. They are termed “spectral matching methods”. Some of these methods assign whole pixels to a class like Spectral Feature Fitting (SFF), Spectral Information Divergence (SID) or Spectral Angle Mapper (SAM). In SFF, the depth of absorption features and the shape of the spectral curve are compared to target reflectance curves. SID matches pixels to reference spectra using divergence measures and SAM compares the angle between pixels vectors and target vectors and assigns the pixel to the class to which it has the smallest angle. Different kind of matching approaches are sub-pixels methods like spectral unmixing. They are based on the concept that an image pixel is a mixed pixel, meaning that the spectrum of an image represents different materials and is the result of a linear combination of the spectra of all materials (termed “endmembers”) inside that pixel. This idea is illustrated in Figure 9. Methods for this are e.g. Linear Spectral Unmixing which maps the abundances of endmember within each pixel from the pixel’s spectrum. For this approach all image endmembers need to be known. A method where this is not the case, is e.g. Matched Filtering (partial unmixing).

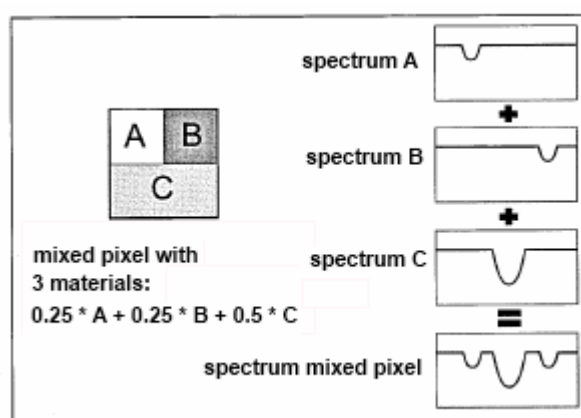


Figure 9: Concept of mixed pixels
(source: modified after Weidner & Brand, 2005, p.27)

Another group of classifiers are non-parametric approaches. Examples of these are Support Vector Machines or Artificial Neural Networks (ANN). Neural Networks build set of linked processing units to solve a classification problem. The network is improved by iteratively classifying the training areas and training the model. Support Vector Machines delineate linearly non-separable classes directly in feature space by fitting a plane between class boundaries.

Out of these possible classifiers two were selected for this study which classify whole pixels. SAM represents the spectral matching approach. This approach is interesting because it does not require much computational time and can work with the full hyperspectral dataset. The non-parametric SVM approach was selected because it achieved high classification accuracies in various studies. The concepts of both classifiers are presented in the next chapter.

2.3.1 Spectral Angle Mapper

The Spectral Angle Mapper maps the spectral similarity of image spectra to reference spectra using data which were corrected from radiance to apparent reflectance, thus correcting for atmospheric effects. The spectral similarity is determined by calculating the spectral angle between the reference spectra and each image spectra. Thereby, the spectra are treated as vectors in n -dimensional space (n is given by the number of bands). The smallest angle to a reference spectrum denotes the class that this image spectrum is assigned to.

The advantage of this method is that it is considered as being insensitive to different illumination conditions of an object or albedo effects (Kruse, et al., 1993). These effects are e.g. caused by shade or inclined roofs. All possible illumination conditions are treated equally. Darker, poorly illuminated pixels will be situated closer to the origin (shorter vectors) than well illuminated pixels in the image (longer vectors). But the angle distance to the vector of the reference spectrum will stay the same. This means that the same material under different illumination conditions will most likely be classified in the same class.

Figure 10 gives a 2-dimensional example with one reference spectrum and one unknown image spectrum. Each spectrum is represented as a point in this 2-D

scatterplot. The lines connecting each point with the origin are the vectors. Only the angle α between the two vectors is considered for the assignment, not the length of the vectors. The smaller the angle, the better it matches the reference spectrum.

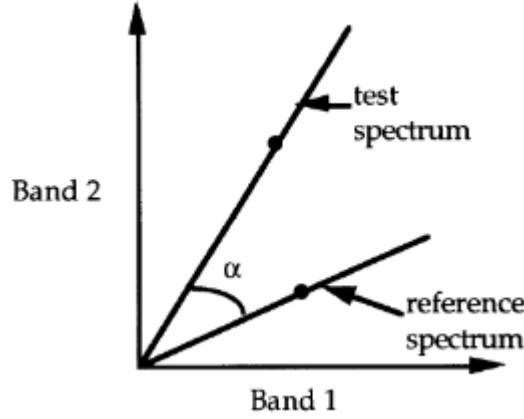


Figure 10: Plot of a reference spectrum and test spectrum for a two-band image (source: Kruse, et al., 2003, p.157).

The similarity of an image test spectrum t to a reference spectrum r is determined by

$$\cos^{-1}\left(\frac{\vec{t} \cdot \vec{r}}{\|\vec{t}\| \cdot \|\vec{r}\|}\right), \quad (4)$$

which can also be written as

$$\cos^{-1}\left(\frac{\sum_{i=1}^{nb} t_i r_i}{\left(\sum_{i=1}^{nb} t_i^2\right)^{1/2} \left(\sum_{i=1}^{nb} r_i^2\right)^{1/2}}\right) \quad (5)$$

with nb being the number of bands (Kruse et al. 1993).

2.3.2 Support Vector Machines

Support Vector Machines (SVM) are derived from the field of machine learning theory and are a set of algorithms. They have already been successfully applied by several authors like Huang, et al., (2002) and Waske et al. (2009). It is a relatively recent classifier although already introduced in the early 1970s (Mather & Tso, 2009).

SVM is a non-parametric classifier which does not assume certain statistical class distributions and is therefore well suited for the high-dimensional hyperspectral dataset.

Additionally, SVM classifiers have been shown to be robust with small training areas sizes (Melgani & Bruzzone, 2004; Pal & Mather, 2006; Foody & Mathur, 2004).

SVM separates two classes by fitting an optimal separating plane (hyperplane) to training data in an n-dimensional feature space. SVM does not use all the training data pixels to find the hyperplane, but only the pixels of a class which lie closest to the pixels of the other class. These are the support vectors. If classes are not linearly separable, the input data are mapped to a higher dimensional space by a kernel function. This enables the fitting of a linear hyperplane and thus the separability of the classes. In the following paragraphs, the SVM concept is explained. This is only a concise explanation of the primary concept of SVM. If not otherwise stated the definitions were derived from Mather & Tso (2009), Pal & Mather (2004) and Bennett & Campbell (2000). For more detailed information, especially the mathematical side of SVM, refer to Burges (1998) and Ivanciuc (2007).

The linearly separable case

For two classes, the SVM will locate a separating hyperplane maximising the distance from each class to the hyperplane. The data points that are closest to the plane, are used to measure the distance. They are called support vectors. The number of support vectors is therefore relatively small as they are only the points close to the boundary.

If there are two linearly separable classes, the training data with n number of samples is represented by $\{x_i, y_i\}$, $i = 1, \dots, n$

where $x \in R^n$ (n-dimensional vector) and $y \in \{-1, +1\}$ (class label).

x_i is the observed feature in a d-dimensional space and y_i the label for training case i

The label is therefore either class 1 (-1) or class 2 (+1).

The classes are said to be linearly separable if a vector w and a scalar b can be defined.

This gives:

$$w \cdot x_i + b \geq +1 \quad \text{for all } y = +1 \quad (6)$$

$$w \cdot x_i + b \leq -1 \quad \text{for all } y = -1 \quad (7)$$

The two equations can be combined to

$$y_i(w \cdot x_i + b) - 1 \geq 0 \quad (8)$$

The aim is to search for an optimal hyperplane which divides the data into two classes in such a way that all the points with the same label are on the same side of the plane (see Figure 11). The distance of the closest points to the plane in each class should be as large as possible. If such a hyperplane is found, the classes are linearly separable. However, theoretically many planes like this can exist. Therefore, the optimal hyperplane is searched which is the one which leaves a margin as large as possible between the classes. To find the plane furthest away from the set of points, the margin between the support planes for each class can be maximised. This means that the margin between the two planes is $\gamma = 2 / \|w\|^2$. Maximising the margin is equal to minimising

$$\frac{\|w\|^2}{2} \quad (9)$$

The minimisation procedure uses Lagrange multipliers and quadratic programming optimisation methods. For an explanation of this please refer to the literature mentioned at the beginning of this chapter.

If singular data points that belong to one class of the training data (i.e. class +1) is located amongst the data cloud of the other class (i.e. class -1), then this is “a non-separable case”. To solve this problem, a slack variable ξ_i , $i = 1 \dots n$ is introduced into the equation, this means the distance to the “correct” side of the classification (soft-margin C-SVM approach). Any point falling on the wrong side of the hyperplane is considered an error (see Figure 12). Erroneous classifications of the training data are allowed but are punished with the slack variable ξ_i . The influence of any single point is thus lessened. The slack variable has the value 0 for correct classifications and > 0 for wrongly assigned points.

The goal is to maximise the margin while minimising the error. Therefore, a penalty parameter C is introduced. It is a weight for the amount of errors. If the parameter C is large, then less errors are tolerated and the margin is small, whereas a small value for C allows more errors and permits a larger margin. C therefore is a trade-off between maximising the margin and penalising the training errors (Janz, et al., 2007).

This changes the equation in (9) to:

$$\min_{w, b, \zeta_1, \dots, \zeta_n} \left[\frac{\|w\|^2}{2} + C \sum_{i=1}^n \xi_i \right] \quad (10)$$

subject to $y_i(w \cdot x_i + b) - 1 + \zeta_i \geq 0$

$\zeta_i \geq 0 \quad \zeta_i = 1, \dots, n$

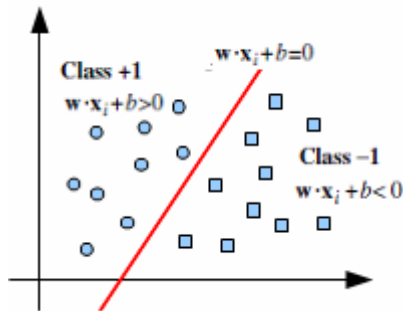


Figure 11: The classification hyperplane

It defines one region for class +1 and one region for class -1.
(Source: modified after Ivanciuc 2007, p. 304)

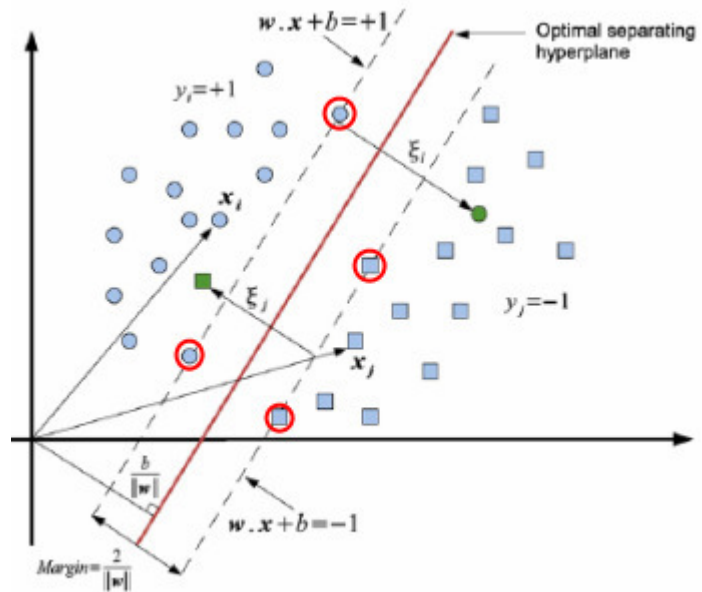


Figure 12: Classification of the non-separable case.
The support vectors are marked in red circles (source: modified after Plaza, et al. 2009, p. S112)

Non-linear separable case

If a hyperplane cannot be defined by linear equations, the method can be extended to also solve non-linear cases. This is done by mapping the training dataset to a higher dimensional feature space. The data is transformed to a higher dimensional space in such a way that makes it possible to find a linear hyperplane.

X is mapped into feature space $\phi(x)$

$$\phi(x): \mathbb{R}^{u1} \rightarrow \mathbb{R}^{u2}$$

where \mathbb{R}^{u1} is the original feature space and \mathbb{R}^{u2} is the higher feature space.

In the higher dimensional feature space, the separating hyperplane between the classes can be found. As the computation of the function $\phi(x)$ is computationally very demanding, SVM uses kernels: for certain mappings of ϕ , the inner product of the mapped points can be evaluated by using a kernel function K :

$$\phi(x_i) \cdot \phi(x_j) = K(x_i, x_j) \quad (11)$$

Different functions of kernels are available from which a user can choose, e.g. Linear Kernel, Polynomial Kernel, Radial Basis Function Kernel (RBF) and Sigmoid Kernel. The RBF kernel is used in this study because it is implemented in imageSVM which is used for the SVM classification. For an explanation of the kernels, please refer to Ivanciuc (2007).

The workflow for the non-linear separable case therefore looks like this:

- a) Transformation of the training data set in n-dimensional space (enlargement of dimensionality)
- b) Calculation of the linear hyperplane
- c) Back-transformation to original feature space

Parameter determination

As can be seen from the explanation so far, the main challenge of SVM is to select suitable parameters which train the SVM well so that classification accuracy is high. Cross-validation is used to find the optimal parameters for every training step during a parameter search. The workflow is such that the training data are divided into a user-defined number of subsets. If a 5-fold cross-validation is chosen, then the data are divided into 5 subsets of equal size. 4 subsets are trained, the 5th is classified. This is done 5 times until every subset has once been classified. As a result, the cross-validation probability “CV” is returned (the percentage of training samples that are correctly classified).

For the SVM classification with the RBF-kernel, there are two parameters to be searched: γ and C . A grid search is done to determine the possible parameter pairs of γ and C values and test it. The parameter pair that produces the best cross-validation accuracy, is then selected for classification.

Multiclass classification

So far, only the two-class problem has been addressed. In remote sensing, however, there are usually multiclass-problems to be solved because more than just two classes exist in the image that is to be classified. The solution for the SVM is to train a series of SVMs. There are several options:

- a) one against the rest: if there are n classes, n SVMs need to be trained. The whole trainings dataset is used for this (one class being tested against the rest) and each pixel either labeled +1 or -1 (depending on whether it is assigned to the searched class +1 or not)
- b) one against one: this is a pairwise comparison: For every pair of possible classes one SVM is trained. If there are n classes this would result in $n(n-1)/2$ runs. After every run, it is memorised in which class this pixel would fall. Every pixel is then assigned to that class in which it was assigned most often leaving no unclassified pixels.

The option “one against one” is implemented in the software package imageSVM and therefore used in this study.

3 Methodology

The chapter describes the methods used for this study to prepare and derive the classification results, including the description of the study area and data basis. Next, the setup of the reference dataset is explained. In the last part of this chapter the study workflow is described, from the preprocessing of the datasets to the classifications themselves and the validation concept of the results.

3.1 Study Area

The study area is situated in the city of Karlsruhe, in South-West Germany (49° 0' 37" N, 8° 24' 17" E). Karlsruhe was planned and built in the 18th century as an absolutist city with the palace in the centre. From the palace, streets are running away radially. The study area is the main campus of the KIT (Karlsruhe Institute of Technology) which is situated to the East of the the palace and to the North of the city centre. To the South and East, the campus is framed by residential buildings in block development. The study area is approximately 1 km x 0.6 km in size and comprises the main campus area including neighbouring residential building blocks (see Figure 13).

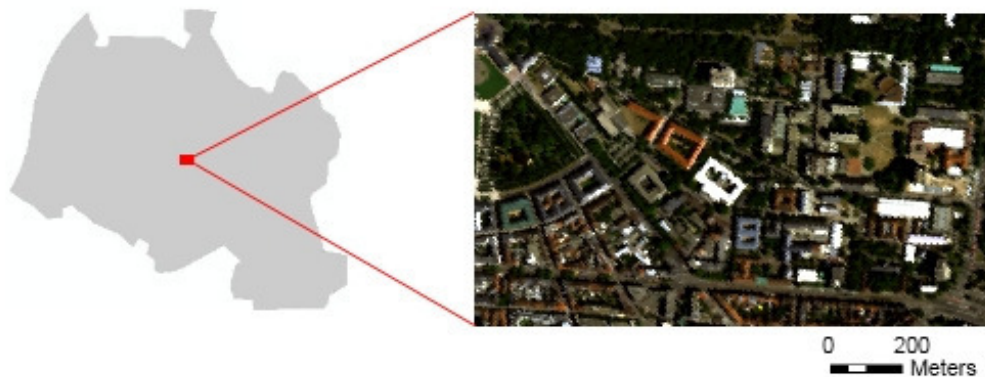


Figure 13: HyMap true colour composite of the study area and its location in Karlsruhe

Buildings on the campus show a mixture of different roof materials of various ages and conditions, as well as different roof types, ranging from residential-like houses with inclined tile and slate roofs to flat-roofed buildings with gravel or stone plate cover, and industrial-like buildings with different metal roofs. The buildings on the campus area

are usually larger than residential buildings. This is advantageous as the HyMap data have a geometric resolution of 4m. The larger the roof, the more pure “roof”-pixels are to be expected. Therefore, the size of the roofs together with the variety of roof materials in a relatively confined space, as well as the accessibility of some roofs make it thus an ideal study area.

3.2 Data basis

The material mapping of roofs was done on the basis of a hyperspectral dataset from the HyMap sensor. Additional data in the form of a binary roof mask and a dataset with roof inclination from a laserscanning dataset was incorporated in the processing. For the identification of training areas, aerial imagery of the main campus area was available. The datasets are described in detail below.

3.2.1 The HyMap sensor

The hyperspectral data used for this study was acquired in July 2003 with the HyMap sensor during the HyEurope campaign organized by the DLR (German Aerospace Center).

The HyMap sensor (Hyperspectral Mapper) is an airborne spectrometer which has been developed by Integrated Spectronics, Baulkham Hills, Australia, for commercial use around the world. It consists of 128 bands in a nearly contiguous wavelength spectrum from 0.44 μm to 2.5 μm . The sensor shows a good signal to noise ratio ($> 500:1$) and image quality which is why it is used in many different types of applications like geological and mineralogical mapping and environmental studies (Cocks, et al., 1998; Hyvista, 2011).

It is an optomechanical system with a rotating mirror recording the reflected radiation in 512 lines. The reflected radiation is recorded in 4 detectors at different wavelength ranges. For later correction, the yaw, pitch and roll effects of the plane are recorded and the integrated GPS (Global Positioning System) allows for the correction of image distortions (Cocks, et al., 1998). The system parameters are listed in Table 2. Table 3 describes the the spectral configuration of the HyMap sensor.

The dataset of this study was acquired on July 19, 2003, at 09:03 CEST (Central European Summer Time) with a solar zenith angle of 41.1° and a solar azimuth angle of 119.6° . The spatial resolution which was achieved with a flight altitude of 2017 m, was 4 m x 4 m (see Table 4). Pre-processing of the dataset was done at the DLR including the atmospheric correction and geocorrection of the dataset. For the atmospheric correction the algorithm ATCOR4 was used.

Table 2: System parameters of HyMap (source: HyVista, 2011)

Platform	airborne
Sensor type	Opto-mechanical
FOV (Field of View)	61.3° (512 pixel)
Ifov (instantaneous FOV)	2.5 mrad along track 2.0 mrad across track
GIFOV (ground instantaneous FOV)	3 – 10 m
Number of bands	128
Radiometric resolution	16bit

Table 3: Spectral configuration of HyMap (source: HyVista, 2011)

Modules	Spectral range (μm)	Average spectral sampling interval	Number of bands
VIS	0.45 – 0.89	15 nm	32
NIR	0.89 – 1.35	15 nm	32
SWIR1	1.40 – 1.80	13 nm	32
SWIR2	1.95 – 2.48	17 nm	32

Table 4: Acquisition information of the HyMap scene

Acquisition date	19.07.2003
Acquisition time	09:03 am CEST
Average flight altitude	2017 m
Latitude	$49^\circ 0' 02''$ N
Longitude	$8^\circ 39' 59''$ E
Solar zenith angle	41.1°
Solar azimuth	119.6°
Spatial resolution	4m x 4m

For the geocorrection, a digital surface model (DSM) from the laserscanning dataset provided by the IPF was used. Further information on the DSM can be found in chapter 3.2.2. The data were also converted from radiance to apparent reflectance. During pre-processing, 2 bands were removed from the dataset resulting in 126 final bands.

3.2.2 Laserscanning data

Information on roofs and the slope of the roofs was available from the IPF in the form of a roof mask from a laserscanning DSM (Digital Surface Model) and a dataset with slope information in percent per pixel. In the following, a general introduction to the underlying laserscanning dataset is given and the two images derived from this dataset are presented.

Laserscanning is a remote sensing method where an object is recorded from pointwise distance measurements. It is an active method where laser pulses with a specific wavelength are emitted from the system and the reflected signal is recorded. Laserscanning sensors are mounted on aircrafts or helicopters. The emitted laser pulse forms a footprint on the ground shaped like an ellipse. This footprint is the unit area from which the reflected signal is recorded. The first pulse only records the uppermost parts of an object, e.g. the top of a tree or the roof of a building. With the last pulse, only the lowest part of the footprint is observed, this is for example the ground below a tree if the signal was able to penetrate the leaf canopy (Vögtle & Steinle, 2005).

The laserscanning data for the DSM used was acquired in March 2002 with the TopoSys II system. The opto-electronic laserscanning system is operated by TopoSys Company in Ravensburg, Germany. For the generation of the DSM at the IPF, first pulse and last pulse data were used. The data were acquired in a spectral range of 1560nm. Conversion was done to 1m x 1m pixels instead of using the original point clouds to facilitate the use in different software packages (Lemp & Weidner, 2004). A binary building mask was then derived from the DSM that discriminates between buildings and ground. A second dataset with the inclination of the roofs in percent per pixel was also calculated and available for this study.

3.2.3 Aerial imagery

Aerial imagery was acquired during a survey flight for the VLW (Amt für Vermessung, Liegenschaften, Wohnen) Karlsruhe in spring 2001 with an analogous standard aerial camera, a Zeiss RMK Top 15. The main campus area is covered by two aerial photographs. They have a scale of 1:4000 (see also Table 5). Figure 14 gives a detail of the aerial photograph.

Table 5: Acquisition information for the aerial imagery

Camera	Zeiss RMK Top 15
Acquisition data	01.04.2001
Acquisition time	11.50 am - 1:30 pm CEST
Altitude	2400 ft above sea level
Scale	1:4000



Figure 14: Detail from aerial photo.
The image detail has about the size of
180 m x 180 m.

3.3 Reference data

Reference data were acquired for several reasons. First of all, to gain knowledge about the roof surface materials present in the image and to be able to choose correct and representative training areas. Secondly, reference data are needed for the accuracy assessment of the classification results.

For this study, a vector reference dataset of the campus roof materials was created. The roof materials were determined by interpretation of aerial images, as well as by visual inspection and ground truth during several field checks. Additionally, a cross-check with the literature was made by comparing spectral reflectance curves of roof materials described in the literature with the reflectance curves of the roof materials in the study area. In the next chapter, the roof materials in the image and their spectral characteristics are described. This is followed by the actual set-up of the reference dataset in ArcGIS 9.3.

3.3.1 Spectral characteristics of the roof materials

In general, the reflectance of an object is related to its physical condition (e.g. particle size) and its chemical composition. Some materials therefore show distinct absorption bands in their spectra. These are caused by electronic and vibrational processes occurring due to interaction with the solar photons. Electronic processes are mostly responsible for absorption in the VIS and NIR region and vibrational processes between the

molecules or in the crystal lattice for absorption mainly in the SWIR (Clark 1999; Hunt, 1977).

In the study area, 11 different roof classes were distinguished. These are: red roofing tiles, slate, stone slab, gravel, bitumen, aluminium, copper, zinc, vegetation and two different metals (metal 1 and 2). For these two metals, the material could not be determined but as they are spectrally unique, they were included as separate classes in the reference dataset. Figure 15 shows representative spectral curves for all classes.

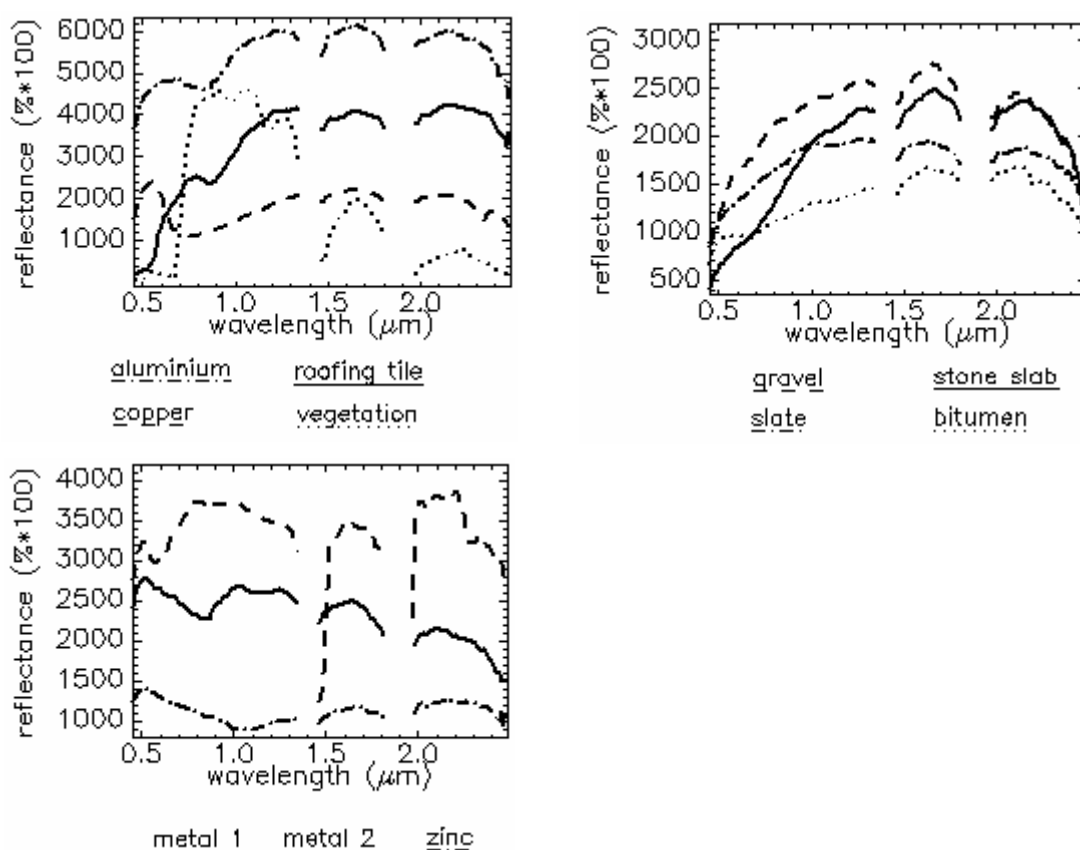


Figure 15: Roof spectra in the study area

The signature of **red roofing tiles** shows several absorption features in the wavelength of 0.52μm, 0.67μm and 0.87μm. The absorption feature at 0.87μm is particularly strong, the other two absorption bands are smaller. The general shape of the curve shows an ascent to NIR and SWIR, with maximum reflectance (around 60%) in SWIR. Tiles contain clay minerals, quartz and ferric oxide. The iron-bearing minerals like Fe₂O₃ are the cause for the absorption bands. During production, tiles are fired a process which leads to an increase in reflectance (Heiden et al, 2001).

Gravel and **stone slab** roofs have very similar spectral signatures dominated by their mineral composition. They show no deep, distinct absorption features in their spectral curves and have rather low reflectance. The reflectance of stone slab lies in the range of 5-25%, the reflectance of gravel being in the same range. The spectral curve, in general, is ascending from the visible to the near-infrared part of the spectrum before descending again. Absorption bands in the SWIR at 2.2 μm and 2.35 μm from silicates and hydrocarbonates (Herold, et al., 2004). There are small absorption bands in the VIS and NIR which can be attributed to iron oxides.

Bitumen has the lowest reflectance of the represented classes. The reflectance ranges between 10-15%. There are no distinct absorption features, only some small absorption bands in the SWIR above 2 μm which can be attributed to hydrocarbons (Cloutis, 1989). In the image, bitumen shows slightly different reflectance in the VIS due to different materials that are included on the bitumen felt like sand or crushed slate.

Slate does not show any distinct absorption features and its reflectance ranges lies between 10-20%. Like bitumen, gravel and stone slab it also shows a reflectance curve that ascends to about 1.6 μm and descends again.

Most metal roofs in the image are made of **aluminium**. It is generally characterized by high reflectance of more than 50%. It has a small peak in the visible at 0.67 μm and a characteristic absorption band at 0.84 μm . Other small absorption bands can be seen at 0.57 μm and 0.63 μm . The reflectance ascends to the NIR and SWIR where it shows a peak.

Zinc has its reflectance peak in the VIS at 0.52 μm . It produces a slowly descending curve to a distinct absorption feature at 1.02 μm . Generally, the reflectance is highest in the SWIR. Zinc has a general low reflectance ranging between 8-20%. From official sources like the building department of the KIT, it could not be determined with certainty what certain metal roofs actually consisted of. Therefore, reflectance curves of the metal buildings were gathered and compared to reflectance curves of spectral libraries (Heiden, et al., 2007, Baldrige, et al., 2008). This showed that the metal roofs with the absorption feature at 1.02 μm was zinc, the one with the absorption feature at 0.84 μm was aluminium. The roofs in the reference dataset were labelled according to these findings.

Copper has a very distinct peak of reflectance in the VIS at $0.55\mu\text{m}$. This means that the material has already oxidised. Copper without patina has its peak in the orange and red part of the electromagnetic spectrum. There is a steep descent of reflectance to a broad absorption band around $0.73\mu\text{m}$ before the reflectance ascends again towards the SWIR. Copper shows medium brightness with reflectance between 10-30%.

As mentioned at the beginning of this chapter, there were two metal roof whose material could not be determined with certainty. In this study they are therefore called “metal 1” and “metal 2”. **Metal 1** shows a distinct absorption feature at $0.57\mu\text{m}$, a smaller one at $0.85\mu\text{m}$ and in the SWIR at $2.27\mu\text{m}$, as well as a peak in the visible at $0.57\mu\text{m}$. The general reflectance curve after the first absorption band is rather flat with a constant reflectance range.

Metal 2 has a peak at nearly the same location, at $0.52\mu\text{m}$, but displays an absorption band at $0.66\mu\text{m}$ and $0.84\mu\text{m}$ in addition to another one between $1.14\mu\text{m}$ and $1.2\mu\text{m}$ there is another small absorption band. The shape of the curve is falling.

Vegetation in this context are trees in the vicinity of buildings, partly obscuring the roofs (because not all trees could be removed from the roof mask, see chapter 3.4.1) or green roofs. The reflectance of vegetation shows a peak in the visible at $0.55\mu\text{m}$ due to chlorophyll which absorbs radiation strongly in the blue and red part of the electromagnetic spectrum but not so much in the green part. There is a very steep ascent of reflectance to the NIR (the so-called “red-edge”). The high reflectance in the NIR is due to multiple scattering of the reflexion in the interior of the plant (Albertz, 2009).

3.3.2 Development of the reference dataset

Because the roof materials in the campus area could be well determined, it was decided to use the full information available, i.e. nearly all roofs on the campus, instead only of few random control areas.

For the creation of the reference dataset, the ArcGIS 9.3.1 software was used. The binary building mask, mentioned in chapter 0, was vectorised. Some buildings were geometrically edited to include borders between roof materials. Afterwards, the class labels were added in form of attributes to the dataset. The HyMap dataset and the aerial imagery were used as reference for this task.

Figure 16 shows the HyMap dataset and the reference dataset overlain. The reference dataset is displayed in yellow. It can be seen that some buildings or parts of building were excluded from the dataset: it only contains buildings which belong to the main campus area where the material could be clearly identified. The residential buildings in the lower left corner of the figure, to the Southwest and South of the campus, were not included. For some buildings, it could not be determined with certainty which roof materials they were covered with. Therefore, these buildings or parts of buildings were left out of the reference dataset. Among these were two buildings with a partial saw-tooth roof (i.e. flat roof with superimposed pitched roofs) covered by a mixture of a corrugated steel roof and glass, a small building mostly covered by overhanging trees and a building site (a future auditorium). The reference dataset finally consisted of 60 buildings and building complexes.

For some buildings, the roof mask derived from laserscanning data does not delineate the roofs precisely. Occasionally, parts of buildings like terraces, courtyards or marquees are also included in the roof mask because they are raised. For the reference datasets these parts of a building were also excluded. The resulting dataset with roof materials is shown in Figure 17 .

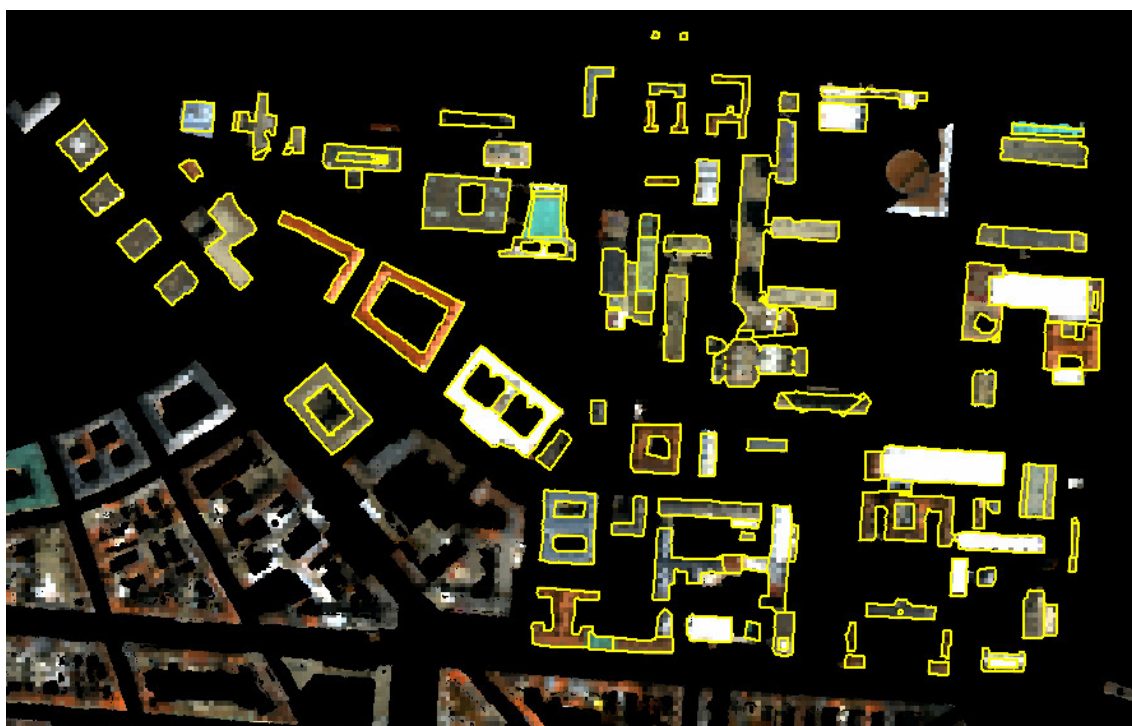


Figure 16: Reference dataset (yellow) with hyperspectral colour composite image in the background



Figure 17: Vector reference dataset with roof surface materials

3.4 Workflow of processing steps

3.4.1 Preparation of data

In this chapter the general workflow of the study will be explained starting with the first processing steps, to the selection of the training and control areas for the classification and finally the different classification methods.

For several reasons, the main campus area was chosen as study area: first of all, many different roofing materials can be found on the campus ground, ranging from typical housing roofs like slate and red tile to different metal roofs which are typical for industrial buildings. This provides an overview of the kinds of roofing materials that can be found in the city of Karlsruhe and other cities in the South of Germany. Secondly, it is advantageous that the roofs are relatively large and thus facilitate classification as less mixed pixels are to be expected.

Removal of “bad bands”

As a first step in the preparation of the HyMap data, the dataset was investigated for bands with a high level of noise in the signal (so called “bad bands”). Signal refers to the information content that is received at the sensor, noise means variations in the signal that are not related to image brightness. It occurs due to variations in the performance of the system (Mather, 1996; Campbell, 1996). Ideally, after radiometric correction (calibration and atmospheric correction), the reflectance values represent only the signal on the ground. However, a certain level of noise may remain in the signal which cannot be removed by radiometric correction. If noise is high, relative to the signal, the image band does not reliably represent the feature of interest.

The 126 bands of the dataset were therefore investigated for their signal-to-noise ratio (SNR) to be able to remove bands with low SNR. The homogeneous area method was used for this task (Smith & Curran, 1996). The SNR is derived from small regions in the image, which are assumed to be homogeneous, to estimate the noise. The idea behind this is that homogeneous regions in the image do not show variations in their signal. Thus, every variation in the signal can therefore be attributed to noise. The SNR is calculated by dividing the mean of the pixel responses in the region (= the signal) by the standard deviation of the pixel responses in the region (= noise) (Smith & Curran, 1996). It can be written as

$$\text{SNR} = \frac{\mu}{\sigma} \quad (12)$$

where μ = average of the signal in an image region, σ = standard deviation of the signal.

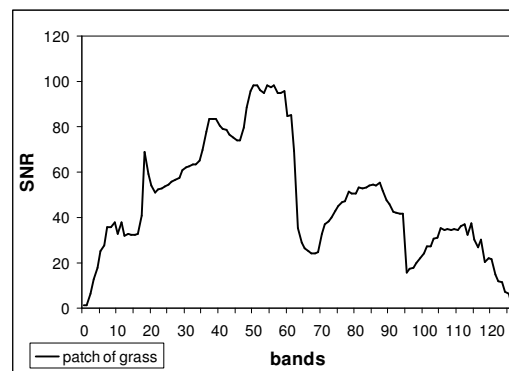


Figure 18: Signal-to-noise ratio of a patch of grass

Exemplarily, the SNR of a grass patch (containing 37 pixels) is shown in Figure 18. There are two major drops of the SNR curve. This is the case in the range of band 63 to 66 (at $1.419\mu\text{m} - 1.447\mu\text{m}$) and band 95 (at $1.951\mu\text{m}$). Additionally, band 1 (at $0.438\mu\text{m}$) also shows low SNR. This corresponds to the first or last bands of the sensor modules. As the SNR is lowest, these bands were excluded from the dataset so that 120 bands remain out of 126.

Masking of the HyMap dataset

The study should not be undertaken on the full image size, therefore the image was clipped to the size of the study area. As explained in chapter 2.2 there are materials on the ground and on roofs that are spectrally similar like e.g. roofing bitumen and road asphalt. Therefore, the roof mask was applied to the hyperspectral dataset to exclude any objects that are not building roofs. The steps are explained in the following paragraphs.

The building mask from the laserscanning data was clipped to an area of appr. 1000m x 600 m, comprising the main campus area and surrounding buildings. This was also done for the original hyperspectral dataset (see Figure 19, the campus ground itself is marked in yellow).



Figure 19: Hyperspectral dataset (band combination 15/9/3) with the main campus area marked in yellow (left). Enlarged detail (right)

The initial roof mask was further processed to create the final roof mask with which the classifications should be undertaken. Figure 20 shows the original roof mask that was available. As there were still a lot of artifacts which were not roofs, e.g. trees or walls, these artifacts were eliminated from the dataset. The elimination was done manually. To

receive information concerning vegetation (e.g. trees) was situated in the image which had to be removed, the NDVI (Normalized Difference Vegetation Index) was calculated from the clipped hyperspectral dataset and all pixel with $NDVI > 0.5$ were displayed. The NDVI is an indicator of live vegetation. It is calculated by dividing the difference of the reflectance in the NIR and red part of the electromagnetic spectrum by the sum of NIR and Red. The result is a number between -1.0 and +1.0, where +1 indicates vegetation presence.

In Figure 21 the pixels with $NDVI > 0.5$ are marked in green. Especially at the left upper part of the image (palace gardens), trees can be seen. By comparison with the aerial image, the pixel with unwanted vegetation were subtracted from the roof mask. This step was done manually because possible vegetation on roofs should be kept in the final hyperspectral dataset. The resulting dataset of the final roof mask is displayed in Figure 22. Before the roof mask was applied to the hyperspectral dataset, the HyMap data were resampled from 4m x 4m to 1m x 1m using nearest-neighbour interpolation to

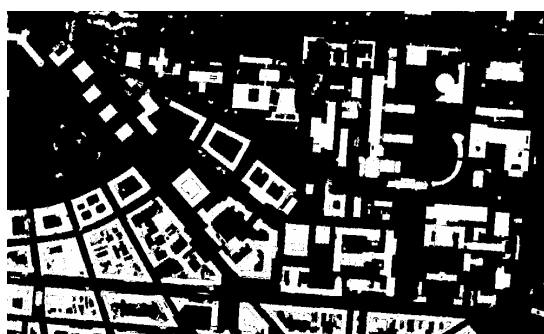


Figure 20: Initial binary building mask including non-building objects

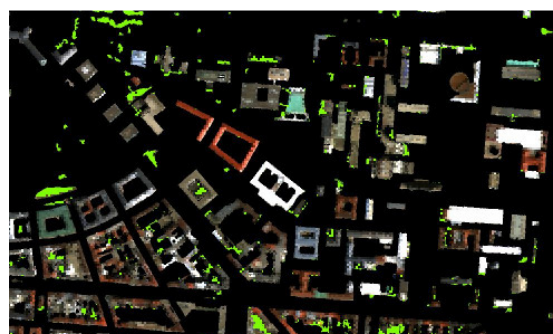


Figure 21: Hyperspectral dataset with pixel $NDVI > 0.5$ marked in green.



Figure 22: Final roof mask

have the same pixel size as the laserscanning dataset from which the roof mask was derived. Tests had already been undertaken at the IPF on the effects of different interpolation concluded that no significant differences between the datasets with bilinear, cubic and nearest-neighbour interpolation were found and thus used nearest-neighbour interpolation. Therefore, this approach was used in this study as well.

Before the roof mask was applied to the hyperspectral dataset, the HyMap data were resampled from 4m x 4m to 1m x 1m using nearest-neighbour interpolation to have the same pixel size as the laserscanning dataset from which the roof mask was derived. Tests had already been undertaken at the IPF on the effects of different interpolation methods using the same hyperspectral dataset (Lemp & Weidner, 2004). They concluded that no significant differences between the datasets with bilinear, cubic and nearest-neighbour interpolation were found and thus used nearest-neighbour interpolation. Therefore, this approach was used in this study as well.

Finally, the roof mask was applied to the hyperspectral dataset and the HyMap dataset clipped to yield the final dataset with which the classification methods were processed (see Figure 23).



Figure 23: Final hyperspectral dataset with roof mask applied (hyperspectral band combination 15/9/3).

Processing of roof slope masks

As has already been stated in chapter 1, one expectation is that the classification of the hyperspectral dataset is improved by integration of roof slope information in the classification. Therefore, two masks of flat roofs and inclined roofs were created. As described in chapter 0, a dataset with the roof inclination in percent per pixel was available from the IPF. A mask for flat roofs and one for inclined roofs was derived from this dataset. The workflow is explained in the following paragraphs.

What is actually termed a flat roof and what an inclined roof? What is the threshold that discriminates them? According to the norm DIN 18531 (DIN, 2008), roof slope is defined as the incline of the pane of a roof against the horizontal. It is measured in percent % or in degree ° (defined as the angle between the pane of a roof and the horizontal). Different definitions exist for the maximum angle for flat roofs. For the construction of roof sealings, the DIN 18531 (DIN, 2008) distinguishes two groups of flat roofs: group I of up to 5° of incline, group II between 5-9° of incline. Another definition takes the incline into account for which it is possible to tile a roof. Flat roofs cannot technically be covered with an imbricated covering like tiles. The lowest achievable incline with roof tiles is 11° (Wormuth, et al., 2007; Grütze, 2007). As the main task of the slope mask is to differentiate between inclined red roofing tiles and slate roofs on one side and flat gravel, stone slab or bitumen roofs on the other side, the definition of the minimum angle for inclined roofs was taken (that is 11°) as threshold, which means that angles of 10° or below define flat roofs in this study.

The available slope dataset gives the incline in percent. 10° of incline correspond to 17,63 %. Thus, all pixels below this threshold are labelled as “flat”, all pixels above as “inclined”. Figure 24 shows the resulting map of flat and inclined roofs in the study area.

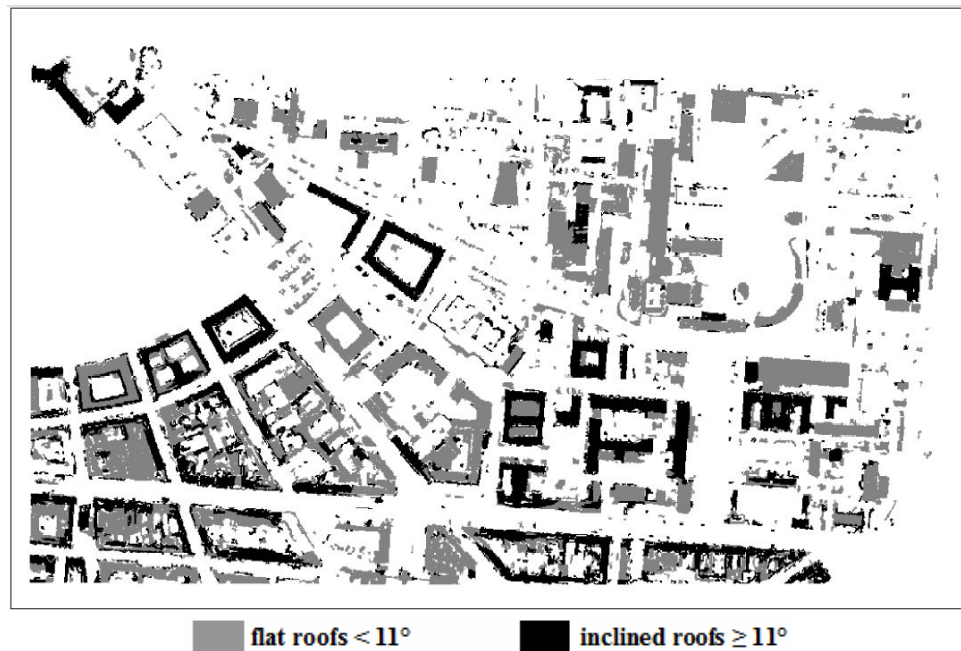
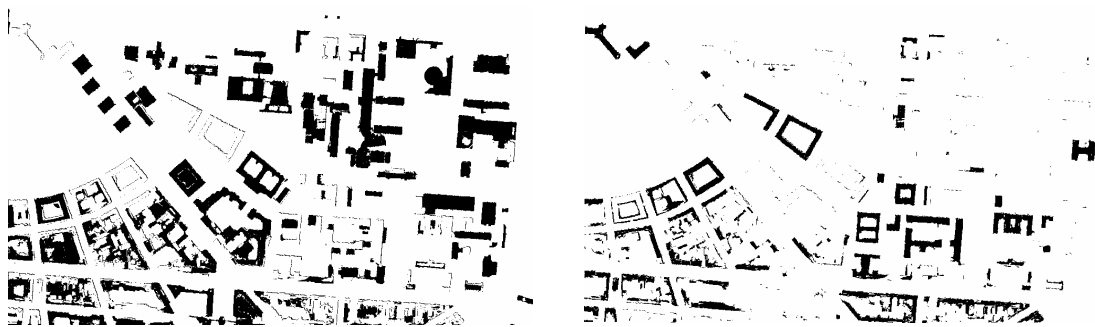


Figure 24: classified map of flat and inclined roofs



Mask of flat roofs. Flat roofs displayed in black

Mask of inclined roofs. Inclined roofs displayed in black.

Figure 25: Final masks of flat and inclined roofs

To create the final masks used in the classifications, the pixels of flat roofs were clipped with the building mask containing only buildings in the study area (as was described above, non-buildings had been manually removed). The same was done for pixels of inclined roofs. The resulting masks can be seen in Figure 25.

3.4.2 Selection of training areas

Training areas are groups of pixels or material spectra that are used as representative classes in classifications which are used to train the classifier. The selection of the training areas for this study was done user-defined from the hyperspectral image with the building mask. Generally, care was taken to select training areas which are representative for the study area and as homogeneous as possible.

It was determined from the reference dataset that the following roof materials are present in the image: red roofing brick tiles, slate, stoneplate, gravel, bitumen, aluminium, copper, zinc, vegetation and two different metals (metal 1 and 2) for which no name of the material could be determined but which are spectrally unique.

The training areas were manually selected in the software ENVI 4.7. ENVI lets the user specify the training areas in form of regions of interest (ROI). These ROIs can then be converted to spectral libraries. For each material at least one ROI in the form of rectangular polygons with several pixels was defined. Some materials required the definition of a second or third ROI due to their variations in colour, age and illumination. With the ROIs, it was tried to represent the different characteristics of the materials. For example for red roofing tiles, three ROIs were selected, each representing a different characteristic of the material: bright red tiles, relatively young; older, more weathered red tiles and dark red tiles. Attention was given to select the ROIs as homogeneous as possible, meaning that they should not include other roof structures like chimneys, roof windows and different materials. However, because of the original spatial resolution of the hyperspectral data of 4 m and because of the nature of the roofs, most of the ROIs contain boundaries and thus mixed pixels. Therefore, in reality the ROIs contain a mixture of purer pixels, which most purely represent the roof materials, and of mixed pixels. Figure 26 shows the ROIs for the different roof materials in the image. Table 6 gives an overview of the ROIs in numerical form.

From the ROIs, a spectral library of roof materials was compiled containing the mean of the spectra of the ROIs for every class. The result are 20 classes for the study area which represent 11 roof materials. Figure 27 displays the resulting spectral curves of the training areas.

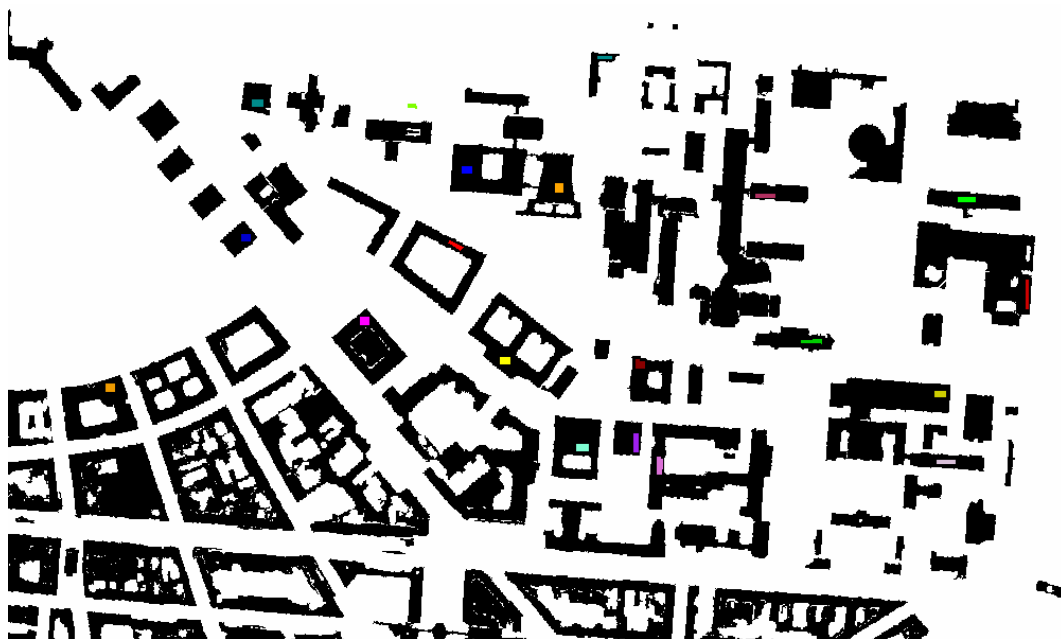


Figure 26: Location of training areas of the roof materials

Table 6: Characteristics of the training areas

Roofing material		ROI	Number of pixels
mineral	slate	slate	70
		slate bright	75
	roofing tile	red tile bright	52
		red tile weathered	62
		red tile dark	55
	stone slab	stone slab 1	63
		stone slab 2	56
	gravel	gravel 1	64
gravel 2		72	
metals	zinc	zinc 1	77
		zinc 2	39
	aluminium	aluminium	63
		aluminium bright	60
	copper	copper bright	63
		copper dark	68
	metal 1	metal 1	68
metal 2	metal 2	65	
organic	roofing felt (bitumen)	bitumen 1	72
		bitumen 2	75
vegetation	vegetation	vegetation	28

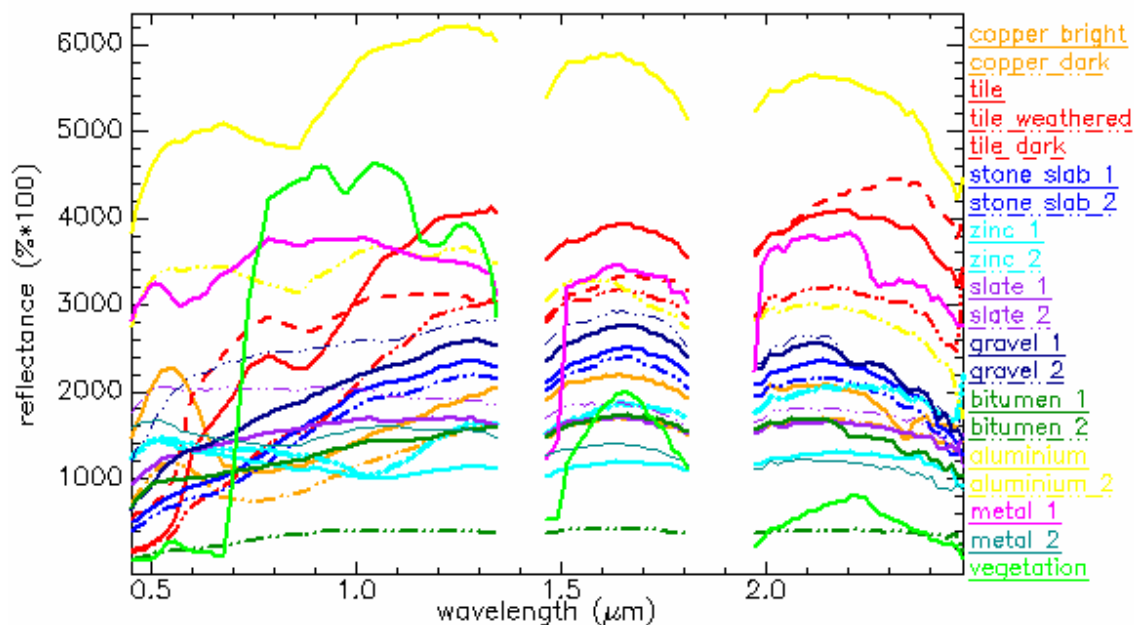


Figure 27: Spectral reflectance curves of all training areas (mean of the pixel values per area)

The spectral library was used as input of the training vectors to the SAM classification. For the SVM classifier, a class image is required as input for the training classes. A class image is an ENVI classification image where ROIs were converted (ITT VIS, 2009).

3.4.3 Workflow of image classification

Pixel-based classification was performed using Spectral Angle Mapper and Support Vector Machines. The theory of the classification algorithms was already explained in chapter 2.3. The detailed analysis of the classification results including parameter search for the classifiers will be described in the next chapter (chapter 4 - Results). The following paragraphs list the steps performed to obtain the classification results.

Spectral Angle Mapper

The Spectral Angle Mapper classifier of the software ENVI 4.7 was used for classification. For the determination of the spectral similarity between a training spectrum and an image spectrum, a maximum angle threshold in radians can be entered. This angle is the maximum acceptable angle between a training vector and the pixel

vector. Pixels with an angle larger than the specified maximum angle threshold are not classified (unclassified pixels) (ITT VIS, 2009).

Several options for using the maximum angle threshold are available in ENVI: the user can determine one angle threshold for all classes. The second option is to define an angle for each class, thereby being able to assign different thresholds for different classes. The output of the SAM classification is the classified image and a set of rule images. Rule images represent the spectral angle in radians between each training spectrum and each image pixel (ITT VIS, 2009). One rule image is delivered for each training class. The lower the spectral angles in the rule image, the better the match is to the training spectra. The rule images were used in return to improve the training areas. To determine the final training classes which proved to classify the image best, an iteration of classification and improvement of the training areas was done.

With the final training area, the classifications of the HyMap data were performed. To find the best angle threshold, classifications with several angle thresholds were tested.

After each classification, the 20 classes were condensed to the final 11 classes. No further post-classification was done. A flowchart of the processing steps can be found in Figure 28.

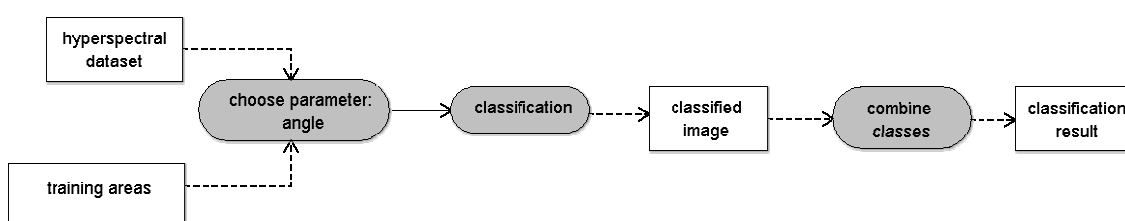


Figure 28: Flowchart of SAM classification

Support Vector Machine

For the Support Vector Machine classifier, the tool imageSVM, a non-commercial product from the Geomatics Lab of the Humboldt-Universität zu Berlin, was used (van der Linden, et al., 2009). imageSVM is a tool for the support vector machine classification programmed in IDL. It can therefore be incorporated in the ENVI/IDL environment. For the training of the SVM, imageSVM uses LIBSVM by Chih-Chung

Chang and Chih-Jen Lin. LIBSVM is an open-source tool for support vector classification, regression and distribution. For an introduction on LIBSVM see Chang & Lin (2011).

SVM is also integrated in the software ENVI itself as one of several other classification tools. However, after an analysis of the possibilities of choosing the parameters for classification, it became apparent that the parameters in ENVI can only be entered user-defined without any knowledge if these are actually the best parameters for the classification. The search of the optimal parameters would therefore be more trial and error. In imageSVM however, the parameters can be searched using cross-validation, thereby providing a high probability of finding the best possible parameters for the support vector classifier.

To be able to compare the performance of the SVM and SAM classifier, the same training areas were used for both classifiers.

ImageSMV uses a two-step approach whereby the classifier is parameterised first. The parameters are then used for the classification. But before the parameter search can be done, the hyperspectral dataset needs to be scaled first. The scaling is necessary to provide suitable values for the parameterisation of the classifier. The pixel values in the image are scaled between 0 and 1. Several options for scaling are available. For this study, the linear scaling was chosen based on the statistics of all bands. This option is also the recommended one for single spectral datasets (van der Linden, et al., 2009). The other option is to scale each band based on individual band statistics.

Next, the support vector classifier needs to be parameterised. imageSVM uses the Gaussian radial basis function kernel (RBF kernel). The user needs to specify a kernel parameter $g (= \gamma)$ (this controls the width of the kernel) and the regularization parameter C . The ideal parameters g and C for a classification depend on class distribution in feature space and the data range, and is different from one dataset to the other. The software provides the possibility to enter ranges of parameters and to test pairs of g and C to find the parameters with the best performance using a grid search (cross-validation). As was described in chapter 2.3.2, this is a common strategy for testing the best values for the two parameters. For the cross-validation, a standard and advanced option can be chosen. The classification was done for both options. In the advanced

option the user enters the range of the cross-validation search, as well as the number of folds. The classification for this study was done with different parameters and these results were then compared. A flowchart in Figure 29 shows the steps of the workflow.

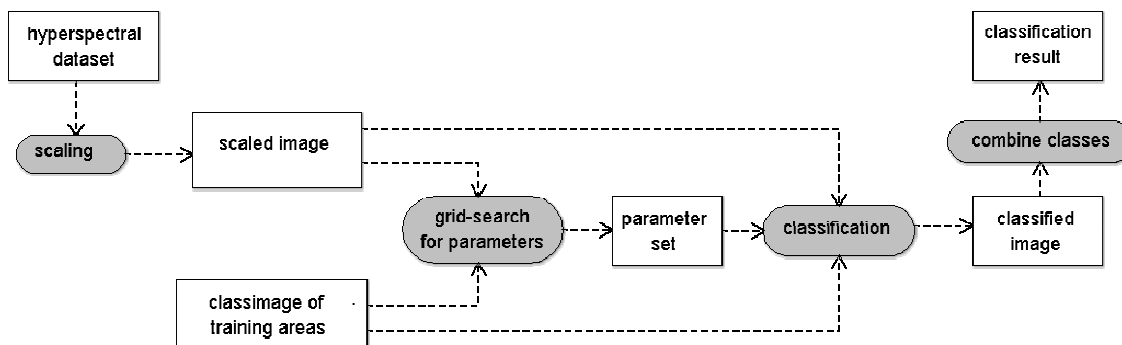


Figure 29: Flowchart of SVM classification.

Incorporation of slope into classification

As the question should be answered if the incorporation of slope information in the classification improves the classification result and thus proves useful for the classification of roof materials, both classifiers were tested by adding slope information to the classification. As the slope dataset and hyperspectral dataset have a different value range, the classification was done with a two-step approach, using the binary roof masks (flat and inclined) described in chapter 3.4.1.

Figure 30 displays the workflow: The hyperspectral dataset was clipped with the flat roof mask and with the inclined roof mask resulting in two input datasets for the SAM and SVM classifier. Next, the training data was divided up into materials for inclined roofs (slate and tiles) and materials for flat roofs (stone slab, gravel and bitumen). Some materials are not restricted to flat or inclined roofs and are therefore included in both training area datasets. These were all metal roofs and vegetation. The reason for vegetation to be included for flat and inclined roofs is, that in the case of trees still inside the mask area, it can not be determined whether the pixel would fall in the flat or inclined category. Green roofs are naturally only to be expected in the flat category.

Finally, these two images were classified. To receive one final classification image, the two classification results with flat and inclined roofs need to be combined again. This was done using band math with the expression $(\text{band 1} \cdot 10) + (\text{band 2} \cdot 200)$. The

constants were introduced to receive different class values for all classes and thus still being able to distinguish the sub-classes. This resulted in a grey scale image, not an image of type “classification” which is needed for further post-classification in ENVI. To obtain a classification image with the final class values (class values 1 to 11 corresponding to the different materials) as is the case for the classification without inclination information, ROIs were therefore created containing all pixels of the same class value. These were then exported to a classimage und finally, the classes were combined again to contain the 11 classes of roof materials. The result is a classification image in which each roof pixel was classified with a training class corresponding to its inclination.

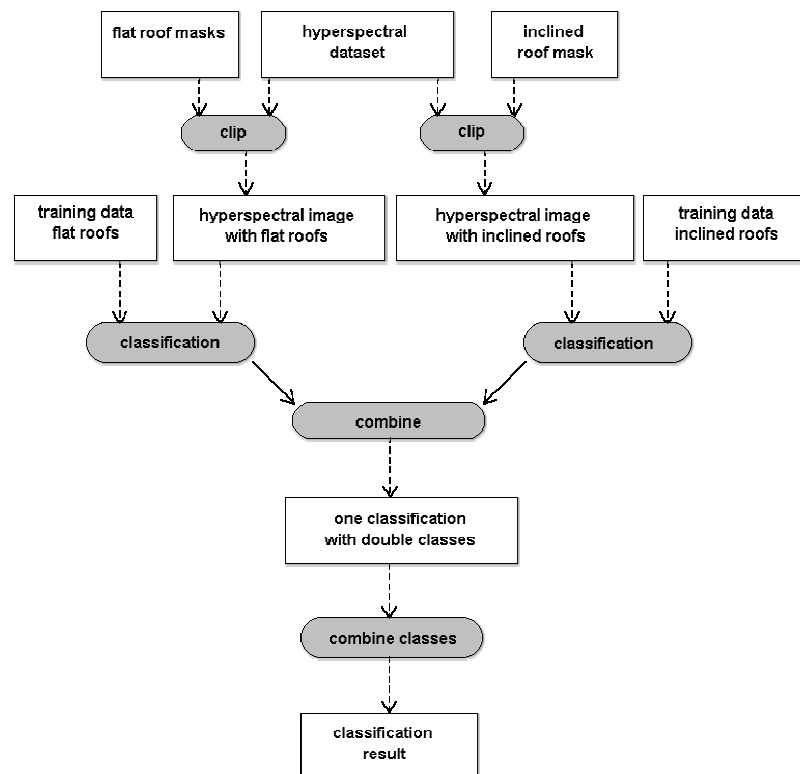


Figure 30: Flowchart of classification workflow with roof inclination

3.4.4 Validation concept

Validation of the classification results is done in two ways: visually by comparing the different classification images and qualitatively by accuracy assessment. Below, a description of the accuracy assessment concept and workflow is given. The results are then analysed in chapter 4.

The goal of accuracy assessment is to assess the reliability of the results and to give information about the quality of the resulting roof material maps.

In this study, the qualitative assessment of the classification results is done on the basis of the campus reference dataset described in chapter 3.3.2. A confusion matrix is calculated for every classification result. A confusion matrix is a table where reference data are related to the corresponding pixel value (thematic class) of the classified image.

ArcGIS 9.3 is used for the comparison of the classification results and the reference dataset. Before the reference dataset can be used for accuracy assessment, however, the training areas need to be geometrically clipped from it. This is necessary because the areas that were used to train the classifier should not be used for testing the result. Training and testing on the same dataset would result in overestimation of the classification accuracy (Congalton, 1991). Figure 31 shows a detail of the reference dataset with the clipped regions of the training areas are.

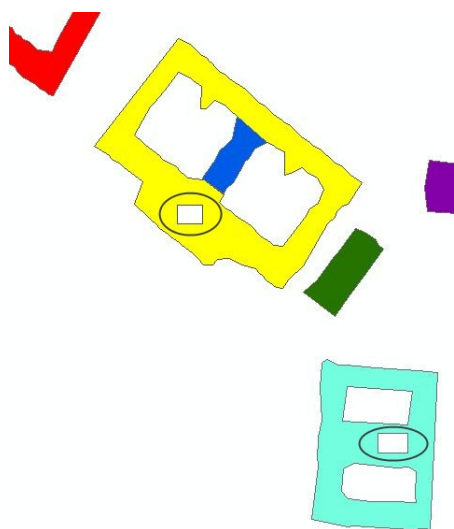


**Figure 31: Detail of the reference dataset with the training areas clipped.
The clipped areas are marked with a black circle**

For the validation in ArcGIS, the classification results are exported from ENVI into the format ‘Geotiff’, to be able to be displayed in the GIS software. The classification results are then converted to points by the tool ‘raster to point’: each cell in the input raster dataset is converted to a point in the output feature. The point is created in the centre of the cell it represents, with an attribute containing the pixel value, i.e. the thematic class (ESRI, 2009). Next, the resulting point features are geometrically intersected with the polygons of the reference dataset. The result is a point shapefile

which contains the features which overlap in both layers, including the attributes (i.e. classes) of both layers. This means that if the point centre of a pixel is inside a polygon of the reference dataset, then it is included in the accuracy assessment. A model for this workflow was created using the Model Builder in ArcGIS. The model is displayed in Figure 32. With this result, the class values of the classification result can be compared to the class values of the reference dataset. The data table of the resulting dataset is thus queried to fill the table of the confusion matrix in Excel.

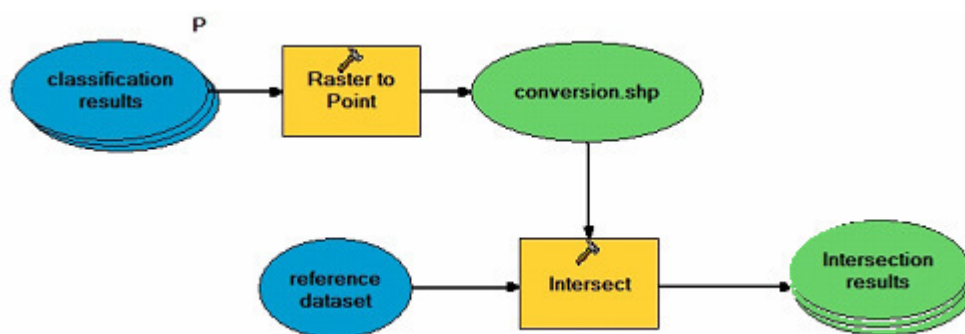


Figure 32: Model in ArcGIS for the calculation of the data basis for the confusion matrix

The final result is a confusion matrix for each classification result. Several measures can be derived from a confusion matrix table which make a statement about the accuracy of the classified image. They are explained below (Congalton, 1991):

The producer's accuracy answers the question how well a certain class can be classified. The probability of a reference pixel being correctly classified can be derived from this percentage.

$$\text{Producer's accuracy} = \frac{\text{total number of correct pixels in a class}}{\text{total number of reference pixels of that class}}$$

The result shows the proportion of pixels in reality which were classified as another class (error of omission).

The probability that a pixel which was classified in the image actually represents that thematic class on the ground, is termed user's accuracy. It provides information on the reliability of a classification and is calculated in the following way:

$$\text{User's accuracy} = \frac{\text{total number of correct pixels in a class}}{\text{total number of pixels classified in that class}}$$

This gives the error of comission, i.e. the proportion of pixels falsely assigned to another class.

The overall accuracy of a classification can also be derived from the confusion matrix Showing the percentage of correctly classified pixels to the overall number of pixels.

The Kappa coefficient is an additional measure of agreement describing the correlation between the classification result and the reference data with values between 0 (rarely below 0) (i.e. all agreement between the reference data and the classification result are by chance) and 1 (i.e. there are no chance agreements between the reference data and the classification result). It is calculated

$$\hat{K} = \frac{N \sum_{i=1}^r x_{ii} - \sum_{i=1}^r (x_{i+} * x_{+i})}{N^2 - \sum_{i=1}^r (x_{i+} * x_{+i})}, \quad (\text{Congalton, 1991}) \quad (13)$$

- r = number of rows in the matrix
- x_{ii} = number of pixels in row i and column i
- x_{i+} = total of all pixels in a row (classification)
- x_{+i} = total of all pixels in a column (reference data)
- N = total number of pixels in the matrix

The fact has to be taken into consideration is, that when validating the classification results using reference data, it is assumed that the reference data are representative for the whole study area as well as being a correct and accurate representation of reality. This would mean that differences between reference data and classification result are errors in the classification result, not in the reference data. This might, however, not always be true, as the reference data might not be completely accurate (Congalton, 1991, Foody, 2002). However, validation using reference data is well established (Foody, 2002) and is therefore also used for this study.

4 Results

The classification results are analysed both visually and quantitatively with confusion matrices. First, the results of the classification without roof inclination are presented, followed by the classifications with roof inclination. The classified images of all reviewed results can be found in the **Appendix A** along with statistics (**Appendix B**) and confusion matrices (**Appendix C**). Where it is applicable for the analysis, some detail of the classification result will also be presented in the text.

4.1 Classification results without roof inclination

4.1.1 SAM

Parameter search


As described above, several classifications were tested using different angles of SAM. The angle is a threshold stating how many pixels stay unclassified (maximum acceptable angle between vectors). A classification with an angle 0.1 rad left more than 25% of all pixels unclassified. An angle of 0.3 rad left only appr. 1.2% of pixels unclassified. However, these unclassified pixels concentrated on a few buildings meaning that some buildings were underrepresented. The angle of 0.5 rad proved best from a visual and statistical point of view with no pixels unclassified.

Additionally, SAM was performed with different angles for each class. For determining the angles, the rule images were used and several different angles for each class were determined. Exemplarily, the angles of one attempt are shown (Table 7). This classification for example showed an overclassification of vegetation and many pixellated roofs for aluminium and slate.

However, the classification with different angles did not improve the accuracy but actually always showed overclassification of some material. Therefore, angle 0.5 rad was chosen for further analysis.

Table 7 : Angles used in the SAM classification with detail from resulting classification. Classes are combined (legend Figure 33)

class	angle (in rad)	class	angle (in rad)
stone slab 1	0,07	gravel 2	0,08
stone slab 2	0,07	bitumen 1	0,11
copper 1	0,16	metal 1	0,14
copper 2	0,12	aluminium 1	0,16
vegetation	0,6	aluminium 2	0,16
slate	0,05	metal 2	0,19
red tile bright	0,15	red tile dark	0,15
red tile weathered	0,19	bitumen 2	0,15
slate bright	0,1	zinc 1	0,2
gravel 1	0,06	zinc 2	0,1



The results with an angle of 0.1 and 0.3 rad and with different angles are not further explained here. All further discussion of results is done on the final angle of 0.5 rad.

Analysis

SAM is a pixel-based classifier. As can be expected, the classification result with an angle of 0.5 rad is pixellated. A clear difference can be seen in the classification between the larger campus roofs and the small residential roofs in the South and Southwest of the image. In general, the campus roofs are more homogeneously classified whereas the small roofs lead to a very blurred image. The visual observations are generally done on the campus roofs because for this part of the image, the reference dataset was created for, and the roof materials are therefore well known.

Tiled roofs are generally quite well classified, not only on the campus but also on residential buildings. However, some pixels at the border of the roof are classified as stone slab. As could be seen from the analysis of the reflectance curve of tiles (see chapter 3.3.1), typical absorption bands are shown, which leads to a good classification with SAM. **Gravel and stone slab** are often confused, meaning that visually there is a strong mix-up between gravel and stone slab. As their material composition is similar, thus are their reflectance curves (Figure 8b), which explains the strong mix-up. The general material on a gravel or stone slab roof, however, is recognized (Figure 33a). The largest amount of confounded gravel pixels is on the stone slab roofs. One major difficulty is the mapping of shadowed materials. Figure 33c shows a gravel roof which was well classified by SAM (see also Figure 7 as comparison). SAM is considered relatively insensitive to illumination effects, and thus proves strong in this point. The **slate roofs** are also not classified very well. In some parts, where the reflectance curves are similar across the roof, the classification is good. But on slate roofs, the different illumination has a strong effect. This can be seen in the upper left part of the image (roof of the Eastern wing of the palace), which is covered with slate.

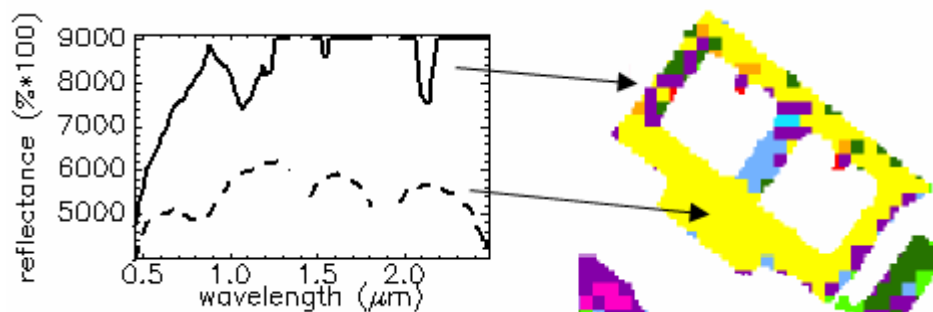


Figure 33: SAM classification examples (angle 0.5 rad)

With SAM, however, it is classified as gravel. Another example is the roof in Figure 33b). The Southern part (brighter) is classified as slate, the northern part as bitumen. The reflectance curves of slate and bitumen are very similar (Figure 8f) and thus making the confusion of these materials more likely. **Bitumen** presents itself overmapped and turns up in small patches on many roofs. Vegetation is also recognized well, either for the remaining trees in the image as well as for some green roofs.

Copper is classified very well, as is metal 1. Metal 2 is also well recognized on the relevant roofs, however, the saw-tooth roofs for which no training area was determined, are classified in this class. Therefore this class is overmapped.

Aluminium does not classify well with the SAM with an angle of 0.5 rad. There are many wrong pixels on the aluminium roofs (Figure 34a). This can best be seen on the large aluminium building in the centre where the western part of the building is strongly confused with slate and some bitumen. The reason for this confusion is reflectance exceeding the sensor capacities, and therefore the aluminium signature is not



a) Aluminium roof (yellow) with many wrongly classified pixels on the west side of the roof due to spectral reflectance that exceeds sensor capabilities. Resulting spectral curves on the left



b) Detail of SAM classification with an angle of 0.5 rad (left) and an angle of 0.1 rad (right). Even when the angle is very small, pixels are already classified as copper (orange) instead of aluminium (yellow).

Figure 34: Wrong classification of pixels on aluminium roofs (SAM, angle 0.5 rad).
For the legend, refer to figure 32

recognizable anymore. A second building with large misclassifications is in the right part of the classification image. This is an aluminium roof that is in part correctly classified as aluminium, in some cases wrongly as copper. The spectral curves of aluminium and copper are not alike, not even when the reflectance is above sensor capacities as is the case on the Southern roof area classified as copper. When comparing this result with the classification of SAM with a small angle of 0.1 rad (Figure 34b), it can be seen that some pixels are already assigned to copper. This means that the two classes are very close in feature space.

4.1.2 SVM

Parameter search

To determine the best set of parameters for the RBF-kernel (i.e. γ and C), a grid-search with internal cross validation was calculated in imageSVM in an iterative process, starting with a coarse range (large steps) and further refining the search with smaller steps to save computational time (Hsu et al., 2009). For this, several searches were done with different search ranges for the grid-search. The grid-search was done in a range of

$$\gamma = 2^{-15} - 2^5 (= 0.000000953 - 256)$$

$$C = 2^{-10} - 2^{20} (= 0.03125 - 262144)$$

with 5 CV-folds meaning that the training dataset is divided into 5 equal parts and each part in turn is classified once.

This resulted in a 99.9198% CV-accuracy (cross-validation accuracy, i.e. the percentage of cases that were correctly classified) with 108 support vectors (SV). The following parameters were found: $\gamma = 2^{-13}$ (=0,000122) and $C = 2^{20}$ (=1048576) (model 1).

Another search range was also done and resulted in different parameters. The search range was:

$$\gamma = 2^{-20} - 2^8 (= 0.000000953 - 256)$$

$$C = 2^{-5} - 2^{20} (= 0,03125 - 262144)$$

With 134 SV and a CV-accuracy of 99.9198% this resulted in the values $\gamma = 2^{-12}$ (=0,000244) and $C = 2^{17}$ (=131072) (model 2).

During the search, several parameter pairs of γ and C were returned that had the same training data accuracy of 99.9198% (highest accuracy achieved). Two of them were mentioned above. This means that there are several models which could be used for classification. The value of γ controls the width of the RBF kernel. If γ is small, then each support vector has a large sphere of influence on the other points. The greater γ is, the higher the risk of overfitting because only the training data are correctly assigned. Figure 35 shows an example of overfitting where, with the same hyperspectral dataset, a large value of γ was chosen for classification. Therefore, in a case where the CV accuracy is the same, the risk of overfitting is minimised when the model with the smallest γ value is chosen. Therefore **model 1** was used for further classification.



Figure 35: Example of overfitting of the training data.
Detail of the SVM classification with the parameter pair: $\gamma = 2^{-40}$, $C = 1000$. The training data (displayed in different colours) are correctly classified, the rest of the pixels are assigned to one class only (red colour)

Analysis

The SVM classification result also shows a pixelated appearance as this is also a pixel-based classifier. The mix-up between **bitumen and slate** is very strong in the image. It is not confined to smaller patches, but bitumen pixels occur on nearly every slate roof in large numbers (see Figure 36a). In this detail, it can be seen that bitumen is very overmapped, whereas the tile roof and aluminium roof in the building block are well recognized. It can be seen that the classification of **aluminium** is much better. The roofs

do not appear pixellated but quite homogeneous. Especially the complicated roof on the right part of the image is classified extremely well (Figure 36b).



a) Slate roof (purple) with many clusters of wrongly classified bitumen pixels (green).
SVM classification left, reference right



b) Aluminium roof (yellow). SVM classification left

Figure 36: SVM classification examples

Vegetation, however, is hardly recognized not even the trees next to buildings that remained in the image from the buiding mask.

The **gravel** roofs classify quite weakly. Especially in the Eastern part of the image, many parts of gravel roofs were classified as bitumen and stone slab, and some even as slate. And the shadowed parts of the gravel roof shown in Figure 33c are classified as bitumen. Shadowed parts therefore, did not classify well with SVM.

For the SVM classification it can be said from the visual analysis that aluminium classifies well, as does stone slab and tiles. Gravel, however, is not correctly recognized in most cases. Bitumen and slate are overmapped and very often confounded. There are two complete roofs that are classified as slate but are actually bitumen.

4.1.3 Visual Comparison

First, a visual comparison of the two classification results was done. It is apparent that both results have some roofs that are very homogeneously classified but the majority of roofs is very pixellated. **Aluminium** is well recognized with SVM. The classification result appears not pixellated for this class. The two buildings that SAM partly confused with copper, are very homogeneous for the SVM classification (Figure 37a). **Stone slab** is also visually better classified with SVM. There are still some wrong pixels but less than in the SAM classification. However, one roof in the North of the image was classified completely wrong: as bitumen instead of stone slab. SAM, on the other hand, recognized this roof very well.

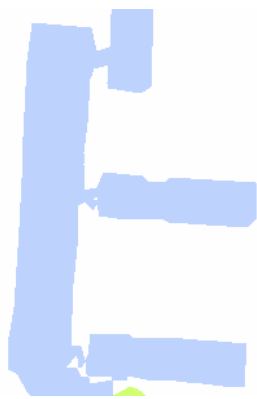
The difference between the two results is most evident for the **shadowed gravel roof**. Figure 37b contrasts the two examples, where SAM classifies some less illuminated pixels as stone slab but the rest of the roof on this building correctly as gravel, SVM does allocate mainly bitumen to these shadowed parts. The building appears much more pixellated than in the SAM result. It can be said that SVM does not deal well with shadowed areas. As the shadowed areas show low reflectance, the SVM classifier assigns these pixels to classes with the lowest reflectance without distinct absorption bands. These are the classes bitumen and slate. A training area was not introduced for shadowed parts of the image, which might have improved the classification for SVM. However, that way it is obvious that the SAM result shows a very good classification of shadowed areas.

The metals **zinc** and **metal 1**, as well as tiles were classified relatively uniform in both results. **Copper** looks slightly over-represented with pixels classified as copper on roofs of other material.

Something that stands out is that for both classifications there are buildings where the borders of the roofs are misclassified while the roof tops are correctly assigned. Figure 38 shows some examples. This is most likely due to the fact that the pixels at the borders of the roofs show a spectral mixture of the roof material and ground surface, especially as the hyperspectral data have a spatial resolution of 4m. This is even more pronounced for the SVM than for the SAM result. With the wrongly classified roof border pixels, it can be made out where the mask has cut the original dataset.



a) SAM result for aluminum roof (left) and SVM result for aluminium roof (right). SVM classifies aluminium correctly and very homogeneously



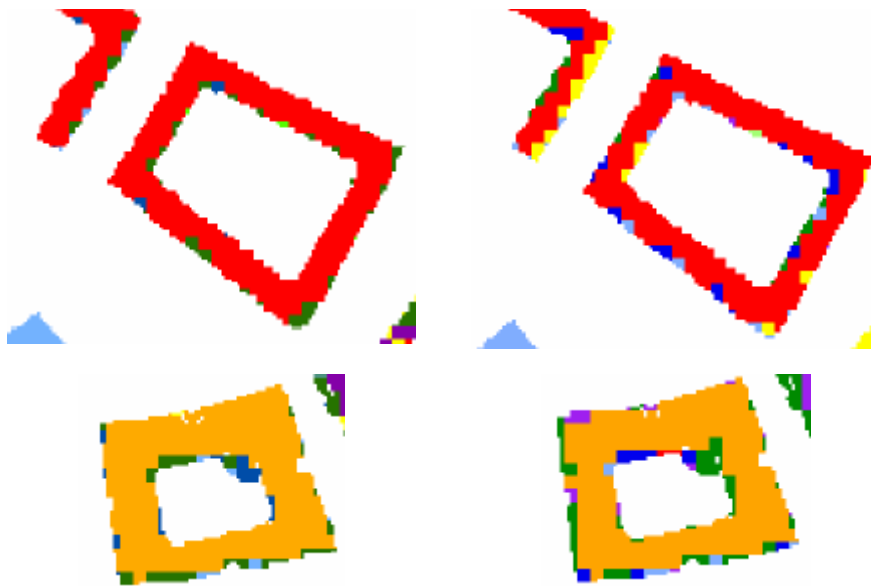
Reference

SAM result

SVM result

b) Comparison of shadowed gravel roof

Figure 37: Visual comparison of SAM and SVM classification of selected roofs



SAM result

SVM result

Figure 38: Example of wrongly classified roof border pixels. Example of tile roofs in the upper row, example of a copper roof below.

There is one building that is very wrongly classified by both SAM and SVM (see Figure 39). It shows the difference that the illumination and the reflectance curve makes. It is a relatively flat aluminium roof (only slight inclination). On the west side, the reflectance of aluminium was correctly recognized. On the east side, the response exceeds the sensor's capabilities. The curve is very flat and therefore resembles the curve of slate or bitumen again (not considering the intensity of reflectance). Thus, SAM classifies these pixels as slate. SVM, on the other hand, classifies this upper part of the building correctly. The lower part of the building is again shadowed by another building, leading to the classification of this part of the building as metal 2, slate or gravel in both results.

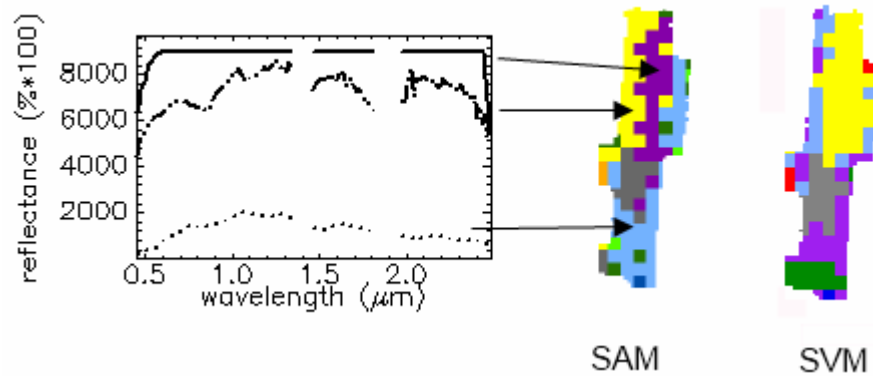


Figure 39: Different reflectance signatures of an aluminium roof leading to wrong class assignment

4.1.4 Quantitative comparison

The quantitative comparison was done using confusion matrices. They were calculated for all classification results discussed here. The confusion matrices and the statistics can be found in **Appendix B** and **C**.

SAM shows an overall accuracy of 70.48% with a kappa index of 0.64, showing a substantial agreement. With 59.06%, the overall accuracy of SVM is about 10% lower than that of SAM, the kappa index of 0.52 indicating a moderate level of agreement (Table 8).

Table 8 : Overall accuracy for SAM and SVM result

classifier	Overall-Accuracy (%)	Kappa-Coefficient	Average producer's accuracy (%)	Average user's accuracy (%)
SAM	70.48	0.64	69.72	61.31
SVM	59.06	0.52	60.38	60.29

SAM has the highest producer's accuracy for metal 1 (92.72%), tile (88.72%) and also gravel (78.00%) (see Table 9 for accuracies for every class with SAM and SVM classification). They also have similarly high user's accuracies. This shows that these classes were classified well. There are several classes which have high user's accuracy, like aluminium with about 89% but much lower producer's accuracy (appr. 54%) indicating that only about half the pixels of the reference area were classified correctly. Slate is another example which has low user's accuracy (appr.47%) but 20% higher producer's accuracy. It is overmapped, mostly at the expense of aluminium. On the other hand, with 77% producers accuracy copper classifies moderately well but is confused with aluminium. Only about 42% of pixels called "copper" are actually copper. The ratio is similar for bitumen, vegetation and metal 2 which classify with around 60% producer's accuracy but have extremely low user's accuracies. The low user's accuracies of some classes are the reason for the average user's accuracy of 61% which is 8% lower than the producer's accuracy (see Table 8).

The distribution of the percentages of classes is different for SAM and SVM (see **Appendix B**, statistics for complete classification results). SAM has about 28% gravel compared to 15% for SVM. This can be explained by the large number of pixels that were not mapped on the shadowed gravel roof. Bitumen is proportionally higher in the

SVM classification (appr. 17%) than in the SAM classification (appr. 12%). This confirms the visual analysis where bitumen seems very prominent in the image of SVM.

SVM, although having a lower overall accuracy, recognizes aluminium pixels in a more reliable way than SAM. Aluminium has a moderately high producer's accuracy of appr. 71%, but the reliability that an aluminium pixel actually is aluminium is above 90%. Gravel and stone slab both have low producer's accuracies, stone slab even an equally low user's accuracy of appr. 50%. It can be seen that there is a lot of confusion between the classes gravel, stone slab, slate and bitumen, which leads to an extremely low accuracy of appr. 30%, respectively 13% for slate and bitumen. Average producer's and user's accuracies lie at about 60%.

Table 9 : Producer's accuracy of the classes for SAM and SVM
Positive difference between SAM and SVM is marked in bold letters (i.e. SVM classified better)

Classes	Producer's accuracy (in %)			User's accuracy (in %)		
	SAM	SVM	Difference SVM-SAM	SAM	SVM	Difference SVM-SAM
Copper	77.10	71.19	-5.91	42.39	70.01	27.62
Tile	88.72	75.26	-13.46	95.96	96.64	0.68
Stone slab	56.86	54.90	-1.96	69.22	50.22	-19.00
Zinc	67.12	58.61	-8.51	97.35	89.05	-8.30
Slate	67.58	68.01	0.43	47.59	29.59	-18.00
Gravel	78.00	43.64	-34.36	76.41	29.59	-6.09
Bitumen	59.54	37.83	-21.71	31.59	13.30	-18.29
Metal 1	92.72	82.63	-10.09	81.70	92.75	11.05
Aluminium	54.63	71.48	16.85	89.54	91.27	1.73
Vegetation	60.97	19.17	-41.8	19.57	39.90	20.33
Metal 2	63.71	81.45	17.74	23.10	20.14	-2.96

From the accuracies it can be seen that SAM gave better results in producer's accuracy and was better in 8 of 11 classes. SVM shows significantly higher accuracy for aluminium and metal 2 there. In user's accuracy, there is only an improvement for SAM in 6 from 11 classes. For 5 classes, mainly copper, metal 1 and vegetation, SVM significantly improved the accuracy. By contrast, stone slab, slate and bitumen were better classified with SAM on the whole. The problem with SVM classification is the high confusion between gravel, bitumen and slate which was also evident from the visible comparison. Compared with the statistic of the reference dataset (see **Appendix B**), slate was very much overmapped (more than double the amount of pixels) for SVM

(appr. 15% instead of 6%). With SAM overmapping happened mainly in the classes slate and bitumen which showed about 3% more percentage than the reference dataset. On the other hand, aluminium was undermapped.

4.2 Classification results with roof inclination

Another question which should be answered in this study is whether the incorporation of roof inclination in the classification process of SVM and SAM improves the classification accuracy. Theoretically, the accuracy should be improved because some materials only occur on inclined roofs, others only on flat roofs. Thus the mix-up of these materials should be less pronounced, if not disappear. In the classification results without inclination information it has become evident that the materials bitumen and slate are mixed-up, as well as gravel and slate. The confusion between gravel and stone-slab or bitumen cannot be solved with this method because both materials are found on flat roofs.

4.2.1 SAM

Analysis

As described in chapter 3.4.3, the classification was split. First the inclined roofs, then the flat roofs were classified with the corresponding training areas. Some different values (single values for all classes) were again tested but again the angle 0.5 rad proved to give the best result visually and so this result was kept for further analysis.

Differences can be seen in the results of SAM with and without roof inclination. There is an improvement in the classification of **slate** roofs which means that it is not mixed-up anymore with bitumen. It also contains less pixels of other classes (Figure 40). **Aluminium** also shows some less wrongly classified pixels on the aluminium roofs. There is not much visual change, though, in the classification of copper, gravel and stone slab. The reason for this might be that copper is included in both mask and therefore would not profit from inclination information, and gravel and stone slab have hardly been confused with inclined roof materials in the first SAM classification.

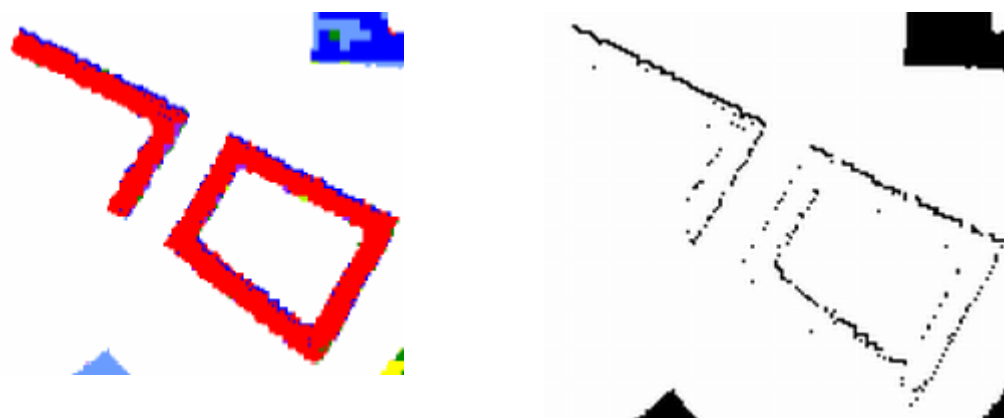


**Improvement of the classification of slate (purple) by the incorporation of inclination information.
Left, SAM without inclination, right SAM with inclination**

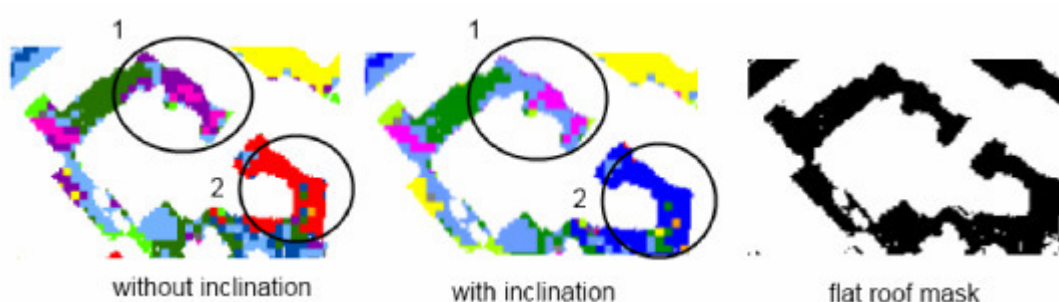
Figure 40: Improvement of the classification due to inclination

Some degradation in classification can also be noticed. First, it can be seen that some inclined roofs are “framed” by flat pixels (Figure 41a). For these pixels, SAM assigns the class “stone slab”. This is explained by the fact that the inclination mask at the border of some inclined roofs like tiles consists of “steep” inclination parts (=roofs) and flat part (= ground) which results in an inclination below 11° and thus in the labelling as “flat”. It is peculiar that some roofs which classified well in the first classification without roof inclination are now mixed-up with stone-slab. This was analysed and the reason is that the inclination mask is erroneous in these parts. It accounts roofs as flat roofs where there are inclined roofs. The Figure 41b displays some buildings with these effects (with and without inclination), along with the inclination mask in these parts. These two features proves that the mapping of roof materials responds to the inclination, so much so that errors of the inclination masks are added to the classification.

It can be summarized that visually this classification looks more homegenous than the one without inclination information. However, the parts of buildings which were wrongly classified, because the inclination mask is wrong in these cases, lowers the classification accuracy.



a) Border pixels of stone slab (blue) on tile roofs (red) on the left side. Corresponding detail of flat roof mask right. The flat pixels in the mask frame the inclined roof.



Some building parts that are inclined (marked with circle) are classified as flat. Example of a slate roof (1) and a tile roof (2) which are classified as gravel (1) and stone slab (2).



Tile roof, mostly correctly classified without inclination, is classified as stone slab in those parts that are labelled "flat" in the inclination mask

b) Effect of errors in roof mask

Figure 41: Effects of inclination mask on the classification

4.2.2 SVM

Parameter search

The SVM classification was also done separately for inclined roofs and for flat roofs with the separated training areas. The processing steps were, to use the previously scaled original image (that was used for the SVM classification without inclination information) and mask the roofs accordingly. It is important to use the same scaled

image to make the results comparable. Then a parameter search was done for each dataset with the same flat/inclined training areas as for SAM. The grid search was done for the following range of γ and C :

$$C = 2^{-15} \text{ to } 2^{40}$$

$$\gamma = 2^{-32} \text{ to } 2^{32}$$

For inclined roofs the parameter search yielded the following values, using 41 support vectors: $\gamma = 23.2831$ and $C = 30000$, but giving only 47% accuracy in cross-validation. The grid search for flat roofs gave 100% CV accuracy and the parameters were $\gamma = 0.00048$ and $C = 32768$ with 100 SV.

The question was why the CV accuracy is so low for inclined roofs and no other search for parameters helped to improve this value. The reason is that not all training areas that are theoretically valid for inclined roofs lie on top of a roof in the mask of inclined roofs. This was not a problem for the SAM classification because ENVI allows the input of training areas in the form of a spectral libraries for SAM, but imageSVM only uses classimage created from ROIs. After the parameter search, it became evident that some ROIs that should occur in both inclination masks actually only existed for the mask of flat roofs. Therefore, the training areas were reduced for the inclined roofs to only contain training areas for tile, slate, copper and zinc.

With the reduced training areas the grid-search for inclined roofs was run again, with the same search range. This improved the CV accuracy significantly. The resulting parameters were $\gamma = 0.00048$ and $C = 32768$ using 217 support vectors.

After parameter search, the two classifications were processed and the results combined to yield the final classified image.

Analysis

For the classes stone slab, gravel, tiles, metal 1 and metal 2 no significant change can be seen compared to the classification without inclination. Some improvement can be seen for bitumen roofs: there are several buildings which were formerly classified wrongly, mostly as slate, which are now correctly classified. Figure 42 shows an example of a bitumen roof.

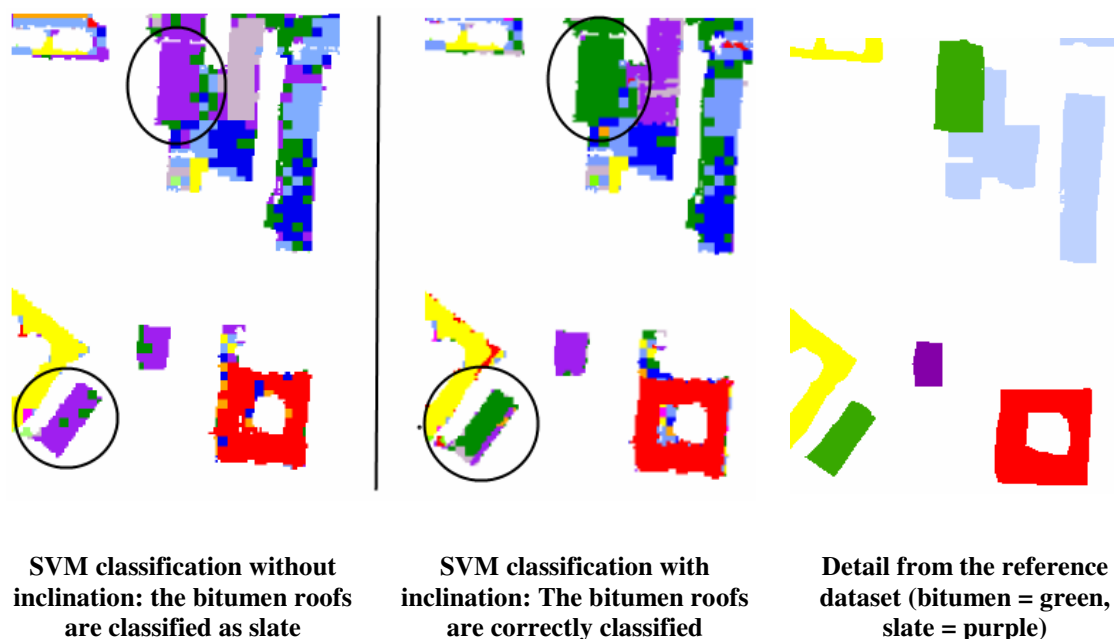


Figure 42: Comparison of a detail of the classification with and without inclination.

The same problem as described for the SAM result with inclination information can also be seen for the SVM result: the erroneous inclination masks for some buildings lead to an assignment of pixels to the wrong class. Additionally, the shadowed areas are still wrongly classified, but the class has changed. Zinc is over-represented because some part of slate roofs are now classified as zinc. The shadowed part of the above mentioned gravel building, which was formerly classified as bitumen, is now largely classified as zinc.

4.2.3 Improvement of slope mask

In order to find out whether there was no significant improvement when inclination information was used for the classification because the hypothesis is wrong or because the errors in the inclination are responsible for this, a manual inclination mask was created. This was used as a kind of cross check to be able to assess the result of the classification with inclination and to find out whether inclination really does improve classification accuracy.

The manual inclination mask was created by adding the slope information “flat” or “inclined” to the reference vector dataset and afterwards converting the data to raster to create two masks in ENVI. The manual masks are displayed in Figure 43.

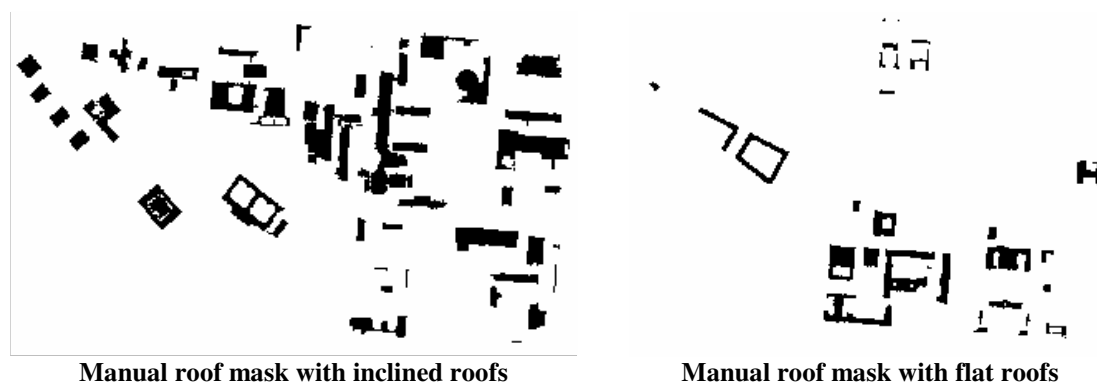


Figure 43: Manual inclination mask

With these masks, the hyperspectral image was again clipped for the SAM classification. The same was done for SVM, using the scaled hyperspectral image instead. The classification of SAM and SVM was repeated. For SAM, the angle of 0.5 rad was used again, for SVM a new parameter search was done with the same training areas as described for the first try minus copper 2 on the flat roofs because the training area was outside the image created by the mask. The grid-search resulted in the parameters $\gamma = 2^{-11}$ ($=0.00048$) and $C = 2^{14}$ ($=16384$) for flat roofs and $\gamma = 2^{-11}$ ($=0.00048$) and $C = 2^{15}$ ($=32768$) for inclined roofs.

4.2.4 Visual Comparison

The visual comparison is described for the results of the classification with inclination of the two classifiers and for each classification result with and without inclination to find out whether the classification could be improved.

First, the SAM classifications with the original inclination dataset and the manually created dataset are compared. It can be seen that the “border” problem is solved indicating that the inclination information has an impact on classification. The classification of the inclined roofs that were originally termed as “flat” by the inclination mask, are correctly classified again. This was to be expected after the inclination was corrected.

The SVM classifications with the manually calculated inclination and the original dataset do not differ much. However, as SVM was also influenced by the errors in the inclination mask, the building parts confused as “flat” were again classified correctly.

The problem with the aluminium roofs, which were classified in the southern roof area as “copper” (Figure 37a) in the SAM classification remains the same for the SAM classification with the manual inclination mask. SVM still does classify this roof well. The aluminium roof that was described in Figure 39 was also not improved by the inclination information. This slope is an inclined roof and the mix-up with slate remains. The SVM result is better in this respect. The problem with the shadowed gravel roof for the SVM classification, however, is also still apparent.

It can thus be observed that the corrected inclination does lead to an improvement of the classification results, both for SAM and SVM. The classifications are less pixellated, the roofs are clearer and more homogeneously assigned to their class. The problems with low reflectance materials that are on flat roofs, i.e. bitumen and gravel, of course remain.

4.2.5 Quantitative comparison

The quantitative comparison was done between the classifications without inclination and the classifications with the original inclination masks, as well as the ones with the corrected manual inclination mask. The confusion matrices and the statistics can be found in **Appendix B and C**. Please refer to Table 11 and Table 12 for the discussed accuracies.

For the SAM classification an improvement in overall accuracy can be seen for the classification with the manual inclination masks which lies at about 4.5%. The Kappa index also increased by 0.06 to 0.70 (see Table 11). The producer’s and user’s accuracies for all classes are compared for the classifications with inclination, the ones with the original inclination mask and the one with the manual inclination mask (see Table 12). For SAM, the improvement was greatest for slate which gained about 20% in producer’s and 26% in user’s accuracy. User’s accuracy for bitumen and stone slab was improved by about 7%. For three classes, vegetation, metal and zinc the accuracy stayed the same. It can be observed that producer’s accuracy improved for all classes. In user’s accuracy, however, 5 out of 11 classes showed a degradation in accuracy which was highest for zinc (-5.24%).

Table 10 : Overall accuracy for SAM and SVM result in comparison with and without inclination information for the roofs

classification	Overall accuracy (%)	Kappa-Coefficient	Average producer's accuracy (%)	Average user's accuracy (%)
SAM	70.48	0.64	69,72	61,31
SAM slope original	70.05	0.64	70,67	60,46
SAM slope manual	74.95	0.70	74,44	63,98
SVM	59.06	0.52	60,38	60,29
SVM slope original	59.12	0.52	62,86	54,61
SVM slope manual	63.83	0.58	66,90	63,55

This general improvement cannot be seen for the classification with the original pixel-based inclination masks. The errors in classification that were observed during the visual analysis are also reflected in the confusion matrix. For many classes, accuracy actually dropped a little. The same tendency can be seen for the SVM classifications: the improvement of accuracy cannot be observed for the classification with the original inclination mask. Basically, overall accuracy stays basically the same, as does the Kappa index. For the classification with the manual mask, accuracy increases just like for SAM by 4.77% to 63.83%. The Kappa index also rises to 0.58%. The accuracy of the classes was improved. Copper, zinc and slate gained more than 10% in user's accuracy, and apart from copper and aluminium, producer's accuracy also improved. This was very much the case for bitumen and slate which improved by appr. 36% and 28% respectively. Slate shows an improvement in user's accuracy almost equally distinct as with the producer's accuracy.

It can be observed that the producer's and user's accuracies for SAM and SVM increased about 4% for both classifications with the manual inclination mask. When looking at the statistics compared with the reference areas (**Appendix B**), it can be seen that for SAM, bitumen is still overmapped, as is vegetation, and aluminium undermapped by appr. 4%. Other percentages changed slightly as well but not significantly. For SVM, a very distinct undermapping of gravel occurred. Instead of the appr. 30% of the reference areas, the SVM classification with manual mask only assigns appr. 20%. Bitumen, on the other hand, is severely overmapped by 10%.

**Table 11 : Comparison by class of producer's accuracy (in %) (with and without inclination)
Positive difference between the classification without inclination and with manual inclination mask
("slope manual") is marked in bold letters**

classification	copper	tile	stone slab	zinc	slate	gravel
SAM	77,10	88,72	56,86	67,12	67,58	78,00
SAM slope original	77,77	79,49	55,82	68,05	70,43	78,07
SAM slope manual	79,38	96,26	57,04	67,12	87,57	79,78
Difference (SAM slope manual - SAM)	2,28	7,54	0,18	0	19,99	1,78
SVM	71,19	75,26	54,9	58,61	68,01	43,64
SVM slope original	67,02	72,42	55,00	64,17	59,53	43,47
SVM slope manual	59,96	83,51	56,67	60,90	96,36	44,33
Difference (SVM slope manual - SVM)	-11,23	8,25	1,77	2,29	28,35	0,69

classification	bitumen	metal 1	aluminium	vegetation	metal 2
SAM	59,54	92,72	54,63	60,97	63,71
SAM slope original	57,21	92,72	60,03	60,97	76,81
SAM slope manual	61,25	92,72	59,93	60,97	76,81
Difference (SAM slope manual - SAM)	1,71	0	5,3	0	13,1
SVM	37,83	82,63	71,48	19,17	81,45
SVM slope original	69,75	82,63	68,52	25,64	83,27
SVM slope manual	74,10	82,98	68,1	24,38	84,63
Difference (SVM slope manual - SVM)	36,27	0,35	-3,38	5,21	3,18

Table 12: Comparison by class of user's accuracy (in %) (with and without inclination).

classification	copper	tile	stone slab	zinc	slate	gravel
SAM	42,39	95,96	69,22	97,35	47,59	76,41
SAM slope original	37,72	97,82	58,88	91,57	64,06	75,91
SAM slope manual	39,30	98,23	76,57	92,11	74,07	77,75
Difference (SAM slope manual - SAM)	-3,09	2,27	7,35	-5,24	26,48	1,34
SVM	70,01	96,64	50,22	89,05	29,59	70,32
SVM slope original	65,27	90,57	52,33	39,27	45,77	68,68
SVM slope manual	86,13	91,82	54,49	99,31	54,54	75,18
Difference (SVM slope manual - SVM)	16,12	-4,82	4,27	10,26	24,95	4,86

classification	bitumen	metal 1	aluminium	vegetation	metal 2
SAM	31,59	81,70	89,54	19,57	23,1
SAM slope original	35,31	78,61	82,33	19,14	23,69
SAM slope manual	38,39	79,80	84,93	19,16	23,52
Difference (SAM slope manual - SAM)	6,8	-1,9	-4,61	-0,41	0,42
SVM	13,30	92,75	91,27	39,90	20,14
SVM slope original	21,33	61,97	91,10	50,23	14,19
SVM slope manual	21,46	80,89	92,70	27,69	14,86
Difference (SVM slope manual - SVM)	8,16	-11,86	1,43	-12,21	-5,28

Generally, it can be concluded that in the case of the pixel-based inclination mask from laserscanning data, the introduction of inclination did not lead to improvements in the overall accuracy compared to the classification without inclination. The expected improvement can only be reached with the manual mask where the errors of the pixel-based one were corrected for.

5 Summary and conclusions

In this chapter, the results of the study are summarized and assessed. An outlook is given to show in which direction future work could lie.

In this study, the ability of roof material mapping with hyperspectral data was assessed. Analyses of the spectral reflectance curves of various urban materials was given, with special stress on roof surfaces. It was shown that roof surfaces like copper, tiles, aluminium or zinc show distinct absorption features where others have a very uniform reflectance curve. This leads to problems in classification because similar reflectance curves are hard to distinguish. To remove the confusion between roof and ground surfaces, a roof mask was applied to the hyperspectral dataset to being able to concentrate on the roofs. With this dataset, two classification methods, Spectral Angle Mapper (SAM) and Support Vector Machines (SVM), were compared.

The other hypothesis of this study was that the incorporation of roof inclination should improve the classification result. For the example of slate this would mean that it can be better classified when roof inclination is considered, because the corresponding materials, with which slate might be mixed-up, exist on flat roofs. For this task, two binary masks were applied on the hyperspectral dataset, which were derived from the laserscanning dataset, and two classifications were performed with the “flat” and the “inclined” hyperspectral dataset. It was found that accuracy of the classification results for both classifiers did not improve. It could be determined that the reason for this was the erroneous inclination dataset where parts of inclined roofs were labelled as flat and vice versa. However, with the classification results it could be shown that a correlation exists between inclination and classification accuracy of some classes because in the case of tiled roofs for example, which were classified well with SAM and SVM in the first attempt without inclination, the accuracy was decreased when the inclination dataset was introduced to classification. To test this proposition, a manual inclination mask was created with which the classifications were repeated. The classification accuracy of the SAM and SVM result were increased by about 4.5%. The increase in accuracy for slate was thereby most significant with more than 20% in user’s and producer’s accuracy for both methods.

Contrary to other studies, which compared SVM to other classifiers like Decision Trees, Artificial Neural Networks, Spectral Angle Mapper or Maximum Likelihood and which found that SVM performed better or at least equally well (Huang, et al., 2002; Foody & Mathur 2004; Melgani & Bruzzone, 2004; Pal & Mather, 2004), this could not be found in this study. The comparisons in literature were done using multispectral but also hyperspectral data for the classification of land-cover maps, with classes like vegetation, built-up, water, etc.. With the more detailed level of material mapping of roofs in this study, Spectral Angle Mapper, however, outperformed the Support Vector Machine classifier. The SAM result gave an overall accuracy of 70.48%, that is about 11% higher than the SVM result (59.06%). When inclination was included (the manual corrected masks), then the overall accuracy was increased to 74.95% for SAM and 63.83% for SVM. SAM, in general shows higher user's and producer's accuracy for most classes. The great strength of the SAM was the ability to distinguish shadowed areas better than SVM could. With SAM, most pixels in the shadowed area were classified correctly, the wrongly assigned pixels just small compared to SVM which had a large number of wrongly assigned pixels due to this reason. SAM, however, encountered severe problems when reflectance was exceeding sensor capabilities. SVM proved more stable in this point, which could be seen in the case of aluminium for which SVM delivered a user's accuracy of over 90%.

This study showed, that both classifiers are suited to map roof surfaces. Further work in this respect could be done by testing different SVM parameters to obtain better classification results or to evaluate if different training areas, especially the incorporation of a shadow class, does improve the accuracy of SVM. Parameterwise, the performance of SVM with a kernel based on the spectral angle instead of the Euclidean Distance (i.e. the RBF-kernel) could be evaluated, which is in literature reported as being scale invariant contrary to Euclidean distance (Fauvel, et al., 2006). Due to the variation in illumination, this might be advantageous for urban studies. The results could be compared to results with the RBF-kernel to see if the better performance of the Spectral Angle Mapper can be transferred to the Support Vector Machine approach.

For both classification methods, it might be interesting to evaluate the classification results when not a binary mask for roof and ground, or for flat and inclined roofs is used, but when the laserscanning dataset is directly included in the hyperspectral dataset. It could be added as an additional image band. To be able to do this, the hyperspectral dataset and the laserscanning band need to be scaled first to derive feasible results.

This study has also pointed out how important the quality of datasets is in the classification process. The laserscanning dataset of roof inclination, which was pixel-based, showed some wrong values for inclination and this led to misclassifications. The classification results might be further improved by not using a binary roof mask but derive roof segments derived from the laserscanning dataset, which are then classified with SAM and SVM. This might improve accuracy and the pixellated appearance of the classification results because it levels out some roof structures and thus the roofs might be classified more homogeneously.

Literature

- Albertz, J., 2009. Einführung in die Fernerkundung. 4. Aufl. Darmstadt: Wissenschaftliche Buchgesellschaft.
- Baldrige, A. M., Hook, S. J., Grove, C. I. & G. Rivera, 2008. The ASTER Spectral Library Version 2.0. *Remote Sensing of Environment*, 113 (4), pp. 711-715.
- Ben-Dor, E., Kruse, F. A., 1995. Surface mineral mapping of Makhtesh Ramon Negev, Israel using GER 63 channel scanner data. *International Journal of Remote Sensing*, 16 (18), pp. 3529-3553.
- Ben-Dor, E., 2001. Imaging Spectrometry for urban applications. In: F. D. Van der Meer, & S. M. De Jong, eds. *Imaging spectrometry. Basic principles and prospective applications*. Dordrecht: Kluwer Academic Publishers. Chapter 9.
- Ben-Dor, E.; Levin, N. & Saaroni, H., 2001. A spectral based recognition of the urban environment using the visible and near-infrared spectral region (0.4-1.1 μm). A case study over Tel-Aviv, Israel. *International Journal of Remote Sensing*, 22 (11), pp. 2193–2218
- Bennett, K. P. & Campbell, C., 2000. Support Vector Machines: Hype or Hallelujah? *SIGKDD Explorations*, 2 (2), pp. 1-13.
- Berdahl, P. & Bretz, S. E., 1997. Preliminary survey of the solar reflectance of cool roofing materials. *Energy and Buildings*, 25 (2), pp. 149- 158
- Bhaskaran, S., Forster, B. & Neal, T., 2001. Integrating Airborne Hyperspectral Sensor Data with GIS for Hail Storm. Post-Disaster Management. 22nd Asian Conference on Remote Sensing 5-9 Nov 2001, Singapore.
<<http://www.crisp.nus.edu.sg/~acrs2001/pdf/178bhask.pdf>> (last accessed 2011-02-05)
- Burges, C. J. C., 1998, A tutorial on support vector machines for pattern recognition. *Data Mining and Knowledge Discovery*, 2, pp. 121–167.
- Campbell, J.B., 1996: Introduction to remote sensing. 2nd ed. London: Taylor and Francis
- Chabrillat, S., Goetz, A. F. H., Krosley, L., & Olson, H. W., 2002. Use of hyperspectral images in the identification and mapping of expansive clay soils and the role of spatial resolution. *Remote Sensing of Environment*, 82, pp. 431–445.

- Chang, C.-C. & Lin, C.-J. 2011. LIBSVM: a Library for Support Vector Machines. <www.csie.ntu.edu.tw/~cjlin/papers/libsvm.pdf> (last accessed 2011-03-30).
- Clark, R.N., G.A. Swayze, A.J. Gallagher, T.V.V. King, & W.M. Calvin, 1993. The U.S. Geological Survey, Digital Spectral Library: Version 1: 0.2 to 3.0 microns, U.S. Geological Survey Open File Report 93-592, <<http://speclab.cr.usgs.gov/spectrallib.html>> (last accessed 2011-03-30)
- Clark, R. N., 1999. Spectroscopy of rocks and minerals and principles of spectroscopy. In: A. N. Rencz, ed., 3rd ed. Remote sensing for the Earth Sciences: Manual of Remote Sensing, Vol. 3., pp. 3–52. Chichester: John Wiley and Sons Inc.
- Cloutis, E.A., 1989. Spectral reflectance properties of hydrocarbons: Remote-sensing implications. *Science*, 245, pp. 165-168.
- Cocks, T., Jenssen, R., Stewart, A., Wilson, I. & Shields, T., 1998. The hymap airborne hyperspectral sensor: the system, calibration and performance. Proceedings of the 1st EARSeL Workshop on Imaging Spectroscopy, Zurich, Swiss.
- Congalton, R. G., 1991. A review of assessing the accuracy of classification of remotely sensed data. *Remote Sensing of Environment*, 37, 35–46.
- Crowley, J. K., 1993. Mapping playa evaporite minerals with AVIRIS data: a first report from Death Valley, California. *Remote Sensing of Environment*, 44, pp. 337-356.
- DIN, 2008. Deutsches Institut für Normung. <<http://www.din.de>> (last accessed 2011-03-23)
- Dixon, B. & Cancade, N., 2008. Multispectral land-use classification using neural networks and support vector machines: one or the other, or both? *International Journal of Remote Sensing*, 29, pp. 1185-1206
- ESRI, 2011. ArcGIS Desktop-Help 9.3. <http://webhelp.esri.com/arcgisdesktop/9.3/index.cfm?TopicName=What%27s_new_in_ArcGIS_9.3> (last accessed 2011-03-30)
- Fauvel, M., Chanussot, J. & Benediktsson, J. A., 2006. Evaluation of kernels for multiclass classification of hyperspectral remote sensing data. IEEE International Conference on Acoustics, Speech and Signal Processing. ICASSP 2006 Proceedings., pp. 813-816

- Foody, G. M., 2002. Status of land cover classification accuracy assessment. *Remote Sensing of Environment*, 80, pp. 186–201.
- Foody, G.M., & Mathur, A., 2004. A relative evaluation of multiclass image classification by support vector machines. *IEEE Transactions on Geoscience and Remote Sensing*, 42, pp. 1335-1343.
- Gamba, P. & Houshmand, B., 2000. Hyperspectral and IFSAR data for 3d urban characterization. *IGARSS 2000 Proceedings, Honolulu*. CD-ROM.
- Goetz, A. F. H., Vane, G., Solomon, J., & Rock, B. N., 1985. Imaging spectrometry for Earth remote sensing. *Science*, 228, pp. 1147–1153.
- Goetz, A. F. H., 2009. Three decades of hyperspectral remote sensing of the Earth: A personal view. *Remote Sensing of Environment*, 113 (Supplement 1), pp. S5–S16.
- Greiwe, A. Bochow, M. & Ehlers, M., 2004. Segmentbasierte Fusion geometrisch hochaufgelöster und hyperspektraler Daten zur Verbesserung der Klassifikationsgüte am Beispiel einer urbanen Szene. *PFG*, 6, pp. 485-494.
- Grütze, D., 2007. *Bau-Lexikon*. München: Carl Hanser Verlag.
- Heiden, U., Roessner, S., Segl, K. & Kaufmann, H., 2001: Analysis of Spectral Signatures of Urban Surfaces for Their Identification Using Hyperspectral HyMap Data. *IEEE/ISPRS Joint Workshop on Remote Sensing and Data Fusion over Urban Areas*, 8.-9. Nov. 2001. Rome, Italy.
- Heiden, U., Segl, K., Roessner, S., Kaufmann, H., 2007. Determination of robust spectral features for identification of urban surface materials in hyperspectral remote sensing data. *Remote Sensing of Environment*, 111 (4), pp. 537-552.
- Herold, M., Roberts, D.A., Gardner, M.E. & Dennison, P.E., 2004. Spectrometry for urban area remote sensing—Development and analysis of a spectral library from 350 to 2400 nm. *Remote Sensing of Environment*, 91 (3-4), pp. 304-319.
- Herold, M. & Roberts, D. A., 2010. The spectral dimension in urban remote sensing. In: T. Rashed, C. Jürgens, eds. 2010. *Remote Sensing of Urban and Suburban Areas*. Dordrecht: Springer. pp. 47-65.
- Hostert, P., 2010. Processing Techniques for Hyperspectral Data. In: T. Rashed, C. Jürgens, eds. 2010. *Remote Sensing of Urban and Suburban Areas*. Dordrecht: Springer. pp. 165-179.

- Huang, C., Davis, L. S. & Townshend, J. R. G., 2002. An assessment of support vector machines for land cover classification. *International Journal of Remote Sensing*, 23 (4), pp. 725–749.
- Hunt, G. R., 1977. Spectral signatures of particulate minerals in the visible and near infrared. *Geophysics*, 42 (3), pp. 501–513.
- Hyvista, 2011. HyVista Corporation. <<http://www.hyvista.com>> (last accessed 2011-03-30)
- ITT VIS, 2009. ENVI 4.7 Users' Guide.
- Ivanciuc, Ovidiu, 2007. Applications of Support Vector Machines in Chemistry. *Reviews in Computational Chemistry*, 23, pp. 291-400.
- Janz, A., van der Linden, S., Waske, B., Hostert, P., 2007. imageSVM - a user-oriented tool for advanced classification of hyperspectral data using support vector machines. In: I. Reusen, J. Cools eds. Proc. 5th Workshop EARSeL SIG Imaging Spectroscopy. Bruges, Belgium. <http://theearselsigis.vgt.vito.be/CD/Posters/Janz_final.pdf> (last accessed 2011-03-30)
- Kruse, F. A., Lefkoff, A. B., Boardman, J. B., Heidebrecht, K. B., Shapiro, A. T., Barloon, P. J., & Goetz, A. F. H., 1993. The Spectral Image Processing System (SIPS) - Interactive Visualization and Analysis of Imaging Spectrometer Data. In: *Remote Sensing of Environment, Special issue on AVIRIS*, 44, pp. 145 - 163.
- Lacherade, S., Miesch, C., Briottet, X. & Le Men, H., 2005. Spectral variability and bidirectional reflectance behaviour of urban materials at a 20 cm spatial resolution in the visible and near-infrared wavelengths. A case study over Toulouse (France). *International Journal of Remote Sensing*, 26 (17), pp. 3859–3866.
- Landgrebe, D., 1999. Some Fundamentals and Methods for Hyperspectral Image Data Analysis. SPIE International Symposium on Biomedical Optics (Photonics West), San Jose California, January 23-29. <<http://dynamo.ecn.purdue.edu/~landgreb/Bios99.pdf>> (last accessed 2011-03-30)
- Lemp, D. & Weidner, U., 2004. Use of hyperspectral and laser scanning data for the characterization of surfaces in urban areas. *IAPRSIS*, Vol. 35, Part B (Comm. VII), CD-ROM
- Lemp, D. & Weidner, U., 2005: Improvements of roof surface classification using hyperspectral and laser scanning data. *Proceedings URBAN 2005*, Arizona. CD-Rom.

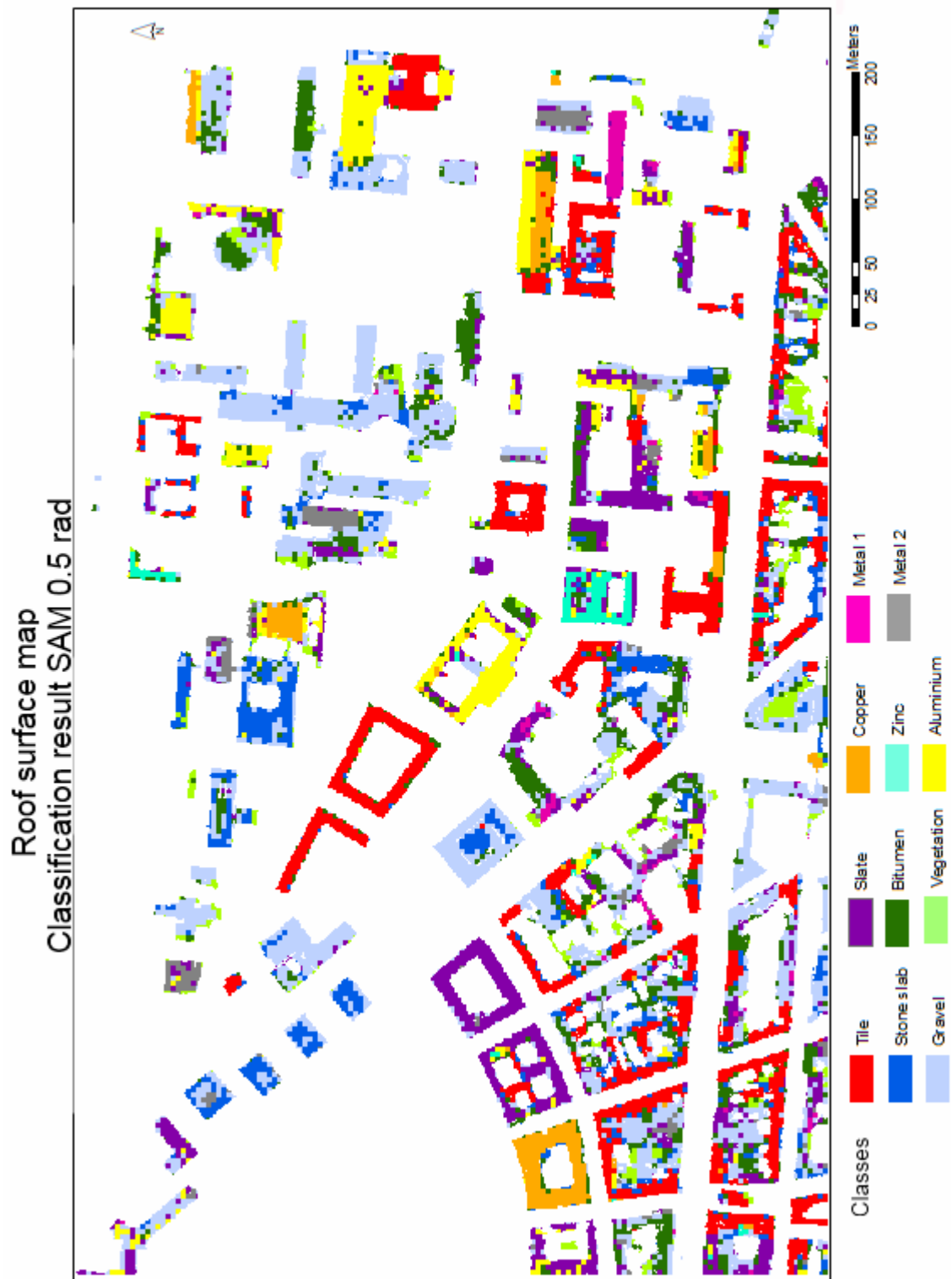
- Lillesand, T.M. & Kiefer, R.W. (1994). Remote sensing and image interpretation, 3rd ed. New York:John Wiley and Sons, Inc.
- M. Middleton, M., Arkimaa, H., Hyvönen, E., Närhi, P., Kuosmanen, V. & Sutinen, R., 2009. Classification of boreal mire biotypes with hyperspectral airborne HyMap in Finland. Proceedings of the 6th EARSeL SIG IS workshop, 16 - 19 March 2009, Tel-Aviv, Israel. <
<http://www.earsel6th.tau.ac.il/~earsel6/CD/PDF/earsel-PROCEEDINGS/3045%20Middleton.pdf>> (last accessed 2011-02-03)
- Madhok, V. & Landgrebe, D., 1999. Supplementing hyperspectral data with digital elevation. IGARSS 1999, Hamburg. CD-ROM.
- Mather, P. M., 1996. Computer processing of remotely-sensed images. An introduction.Chichester:John Wiley & Sons.
- Mather, P. M., Pal, M., 2003. An assessment of the effectiveness of decision tree methods for land cover classification. Remote Sensing of Environment, 86, pp. 554–565.
- Mather, P. M. & Tso, B., 2009. Classification methods for remotely sensed data. 2nd ed. Boca Raton: Taylor & Francis Group
- Mather, P. & Koch, M., 2011: Computer Processing of remotely-sensed images. An introduction. 4th ed. Chichester: Wiley-Blackwell.
- McMorrow, J.M., Cutler, M.E.J., Evans, M.G., & Al-Roichdi, A., 2004. Hyperspectral indices for characterizing upland peat composition. International Journal of Remote Sensing, 25, pp. 313-325.
- Meister, G., Rothkirch, A., Spitzer, H. & Bienlein, J., 2000. BRDF field studies for remote sensing of urban areas. Remote Sensing Reviews, 19, pp. 37-57.
- Melgani, F., & Bruzzone, L., 2004. Classification of hyperspectral remote sensing images with support vector machines. IEEE Transactions on Geoscience and Remote Sensing, 42, pp. 1778-1790.
- Moreira, R.C. & Galvao, L. S., 2010. Variation in spectral shape of urban materials. Remote Sensing Letters, 1 (3), pp. 149-158.
- Pal, M., Mather, P. M., 2003. Support vector machines for classification in remote sensing. International Journal of Remote Sensing, 26 (5), pp. 1007-1011.

- Pal, M., Mather, P. M., 2004. Assessment of the effectiveness of support vector machines for hyperspectral data. *Future Generation Computer Systems*, 20, pp. 1215-1225.
- Pal, M., & Mather, P.M., 2006. Some issues in the classification of DAIS hyperspectral data. *International Journal of Remote Sensing*, 27, pp. 2895-2916.
- Plaza, A., Benediktsson, J.A., Boardman, J.W., Brazile, J., Bruzzone, L., Camps-Valls, G., Chanussot, J., Fauvel M., Gamba, P., Gualtieri, A., Marconcini, M., Tilton, J. C. & Trianni, G., 2009: Recent advances in techniques for hyperspectral image processing. *Remote Sensing of Environment*, 113 (Supplement 1), pp. S110-S122
- Roessner, S., Segl, K., Heiden, U., & Kaufmann, H., 2001. Automated differentiation of urban surfaces based on airborne hyperspectral imagery. *IEEE Transactions on Geoscience and Remote Sensing*, 39 (7), pp.1525–1532.
- Schiefer, S., Hostert, P. & Damm, A., 2006. Correcting brightness gradients in hyperspectral data from urban areas. *Remote Sensing of Environment* 101, pp. 25-37.
- Small, C., 2003. High spatial resolution spectral mixture analysis of urban reflectance. *Remote Sensing of Environment*, 88, 170-186.
- Smith, G.M. & Curran, P.J., 1996. The signal-to-noise ratio (SNR) required for the estimation of foliar biochemical concentrations. *International Journal of Remote Sensing*, 17 (5), pp. 1031-1058
- Subramanian, S., Gat, N, Sheffiled, M., Barhenb, J., Toomarianc, N., 1997. Methodology for hyperspectral image classification using novel neural network. *Algorithms for Multispectral and Hyperspectral Imagery III*, SPIE Vol. 3071--Orlando, FL, April 1997. www.techexpo.com/WWW/opto-knowledge/NNET.pdf (last accessed 2011-01-30)
- Taha, H., 1997. Urban climates and heat islands: albedo, evapotranspiration, and anthropogenic heat. *Energy and Buildings*, 25 (2), pp. 99-103.
- Van der Linden, S., Rabe, A., Okujeni, A. & Hostert, P., 2009. *imageSVM classification, Application Manual: imageSVM version 2.0*. Berlin: Humboldt-Universität zu Berlin.
- Van der Meer, F., 1996. Metamorphic facies zonation in the Ronda peridotites: spectroscopic results from field and GER imaging spectrometer data. *International Journal of Remote Sensing*, 17 (9), pp. 1633-1657.

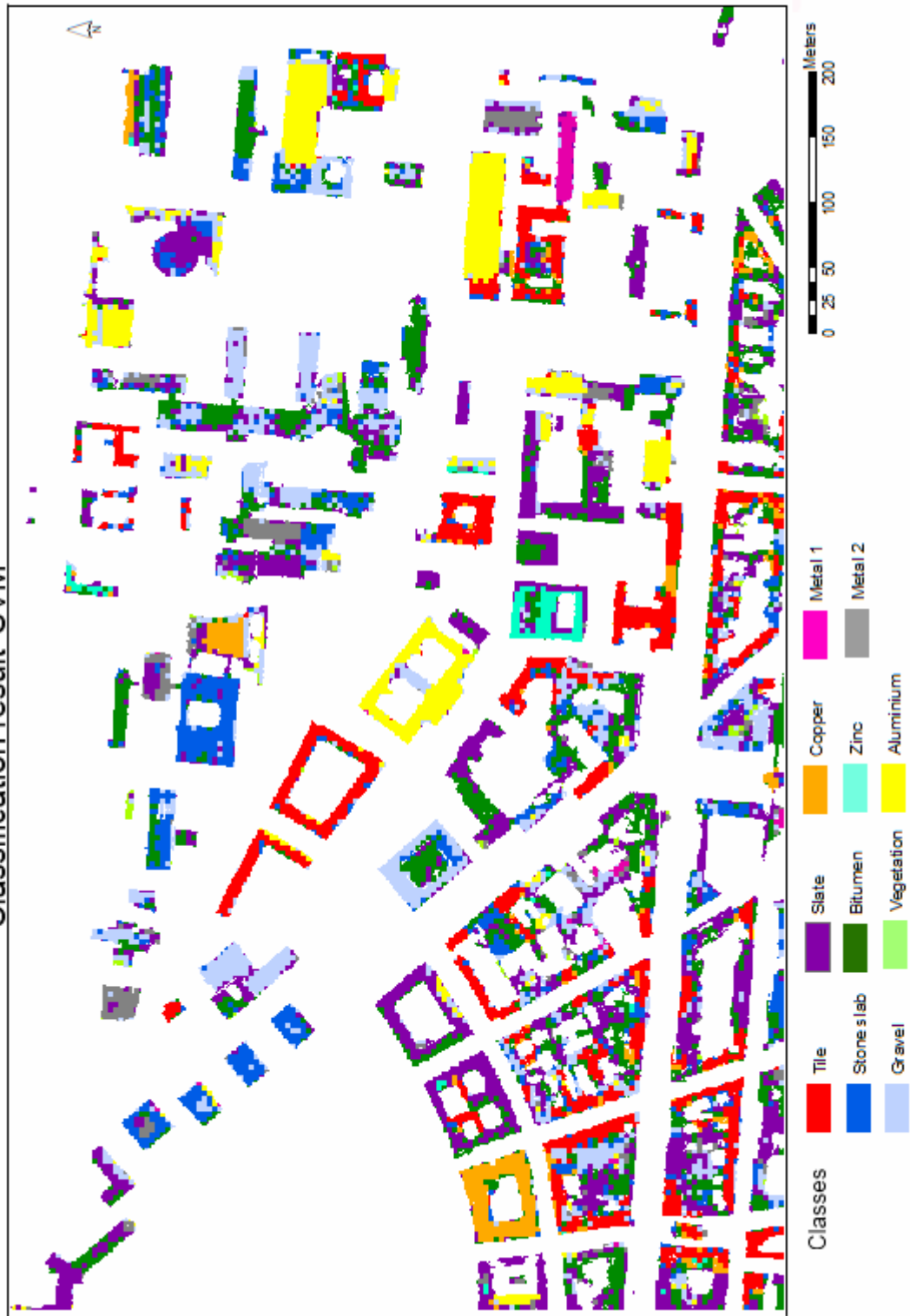
- Van der Meer, F., de Jong, S. & Bakker, W., 2001. Imaging Spectrometry: Basic analytical techniques. In: F. D. Van der Meer & S.M. De Jong eds. *Imaging spectrometry. Basic principles and prospective applications*. Dordrecht: Kluwer Academic Publishers. Chapter 2.
- Van der Meer, F., 2004. Analysis of spectral absorption features in hyperspectral imagery. *International Journal of Applied Earth Observation and Geoinformation*, 5, pp. 55–68
- Vögtle, T., Steinle, E., 2005. Flugzeuggetragenes Laserscanning. In: H.-P., Bähr, T. Vögtle eds. *Digitale Bildverarbeitung*. 4th ed. Heidelberg: Wichmann, pp. 29-45.
- Wang, Y. Y. and Li, J., 2008. Feature-selection ability of the decision-tree algorithm and the impact of feature-selection/extraction on decision-tree results based on hyperspectral data. *International Journal of Remote Sensing* 29 (10), pp.2993–3010.
- Waske, B., Benediktsson, J. A., Arnason, K. & Sveinsson, J. R., 2009. Mapping of hyperspectral AVIRIS data using machine-learning algorithms. *Canadian Journal of Remote Sensing*, 35 (Supplement 1), pp. S106-S116.
- Weidner, U., Brand, S., 2005. Hyperspektrale Erderkundungssensoren. In: H.-P., Bähr, T. Vögtle eds. *Digitale Bildverarbeitung*. 4th ed. Heidelberg: Wichmann, pp. 19-28.
- Weidner, U., Lemp, D., Voskamp, M., Abbt-Braun, G., Bähr, H.-P. & Frimmel, F.H., 2005. Anwendung von Fernerkundungsmethoden zur Schadstoffbilanzierung in Urbanen Gebieten. In: *Wissenschaftlich-technische Jahrestagung der DGPF 2005*, Rostock. CD-ROM.
- Wormuth, R., Dierks, K. & Fleischmann, H.D., 2007. Dächer. In: Dierks, K. and Wormuth, R. eds., *Baukonstruktion*. 6. Auflage, Neuwied: Werner-Verlag
- Xiao, Q., Ustin, S. L. & McPherson, E. G., 2004. Using AVIRIS data and multiple-masking techniques to map urban forest tree species. *International Journal of Remote Sensing*, 25 (24), pp. 5637–5654
- Yuhas, R. H., Goetz, A. F. H., Boardman, J. W., 1992. Discrimination among semi-arid landscape endmembers using the spectral angle mapper (SAM) Algorithm. *Summaries of the Third Annual JPL Airborne Geoscience Workshop, JPL Publication 92-14*, 1, pp. 147-149.
<ftp://popo.jpl.nasa.gov/pub/docs/workshops/92_docs/52.PDF> (last accessed 2011-01-13)

Appendices

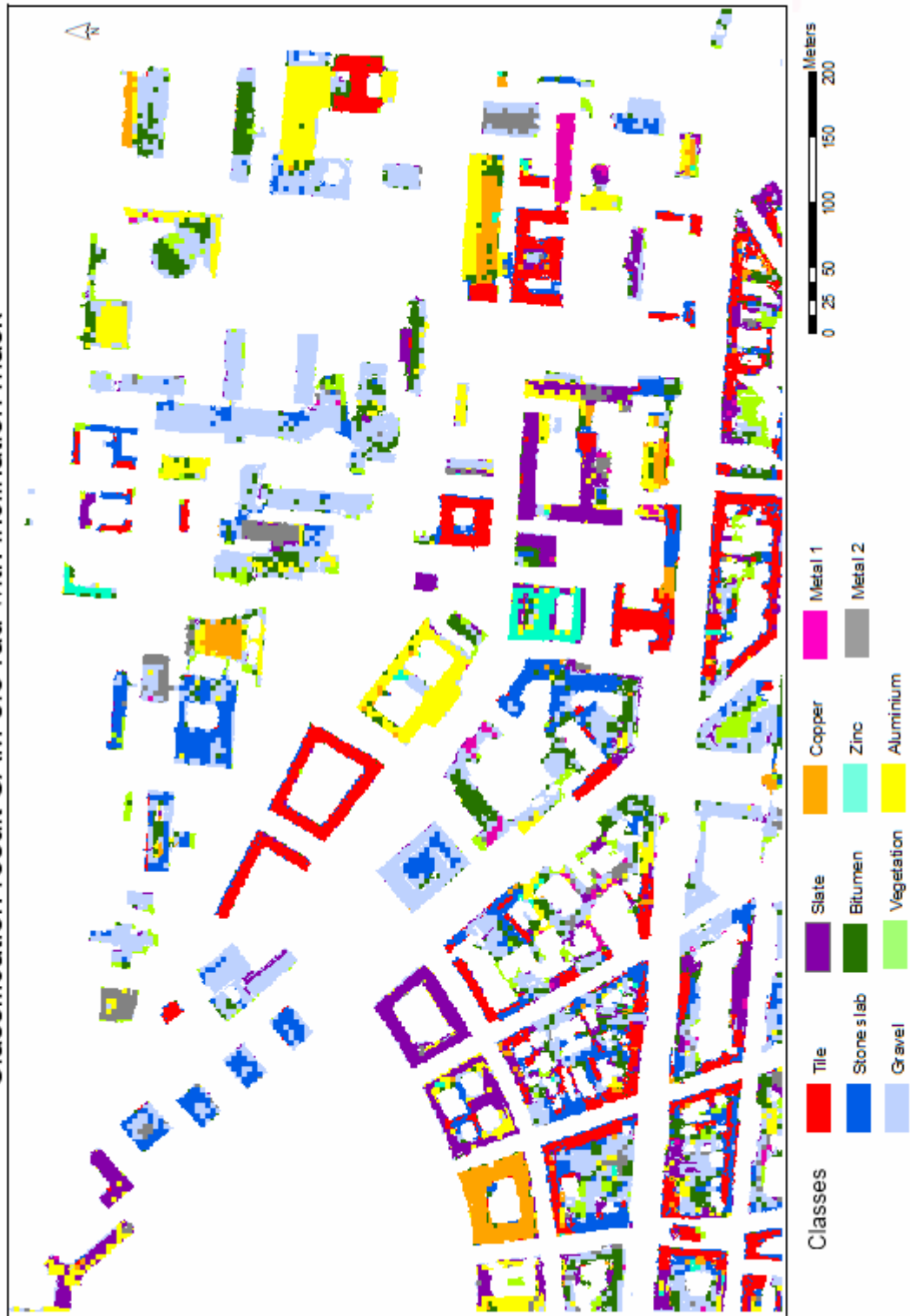
A. Classification results



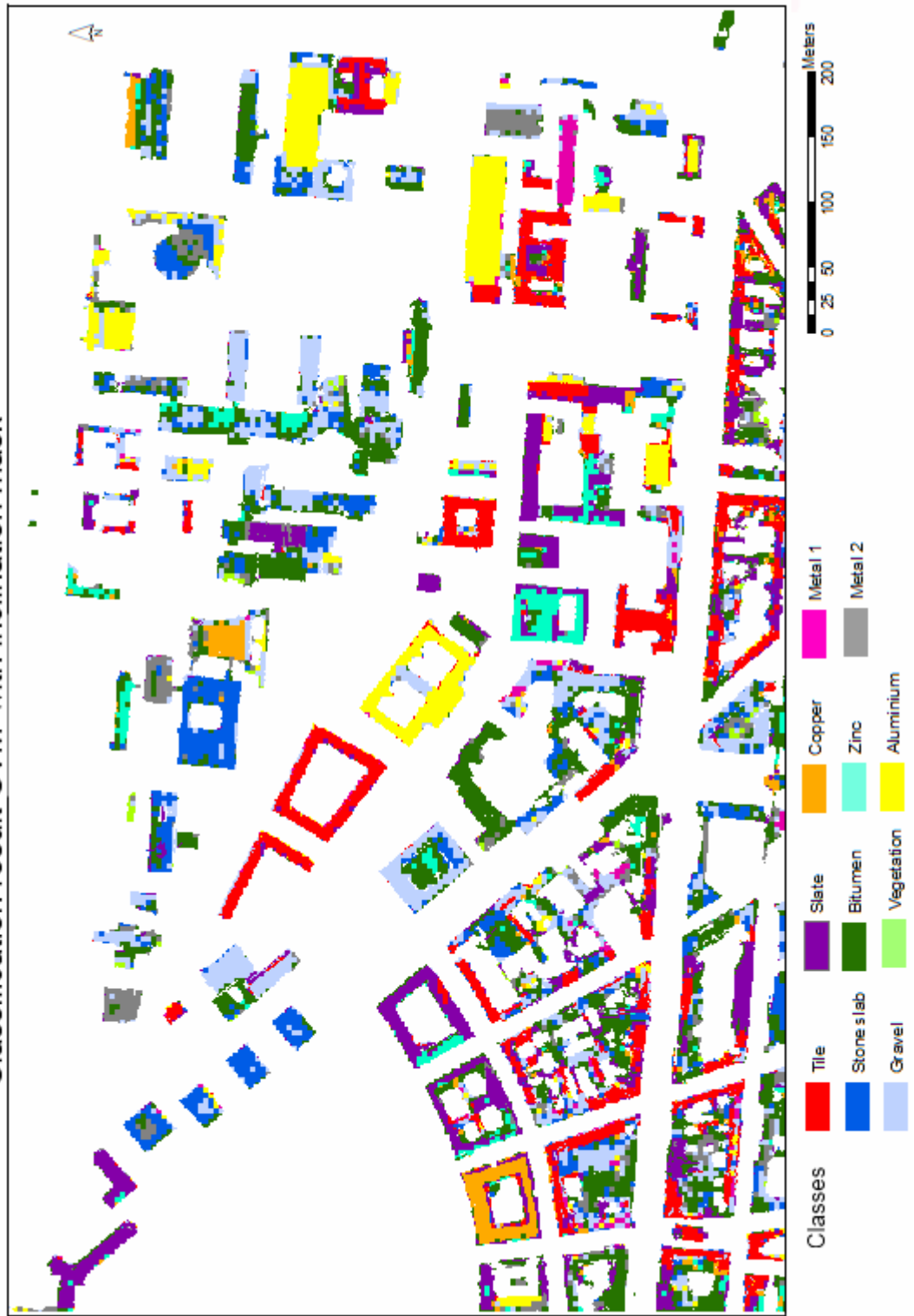
Roof surface map
Classification result SVM



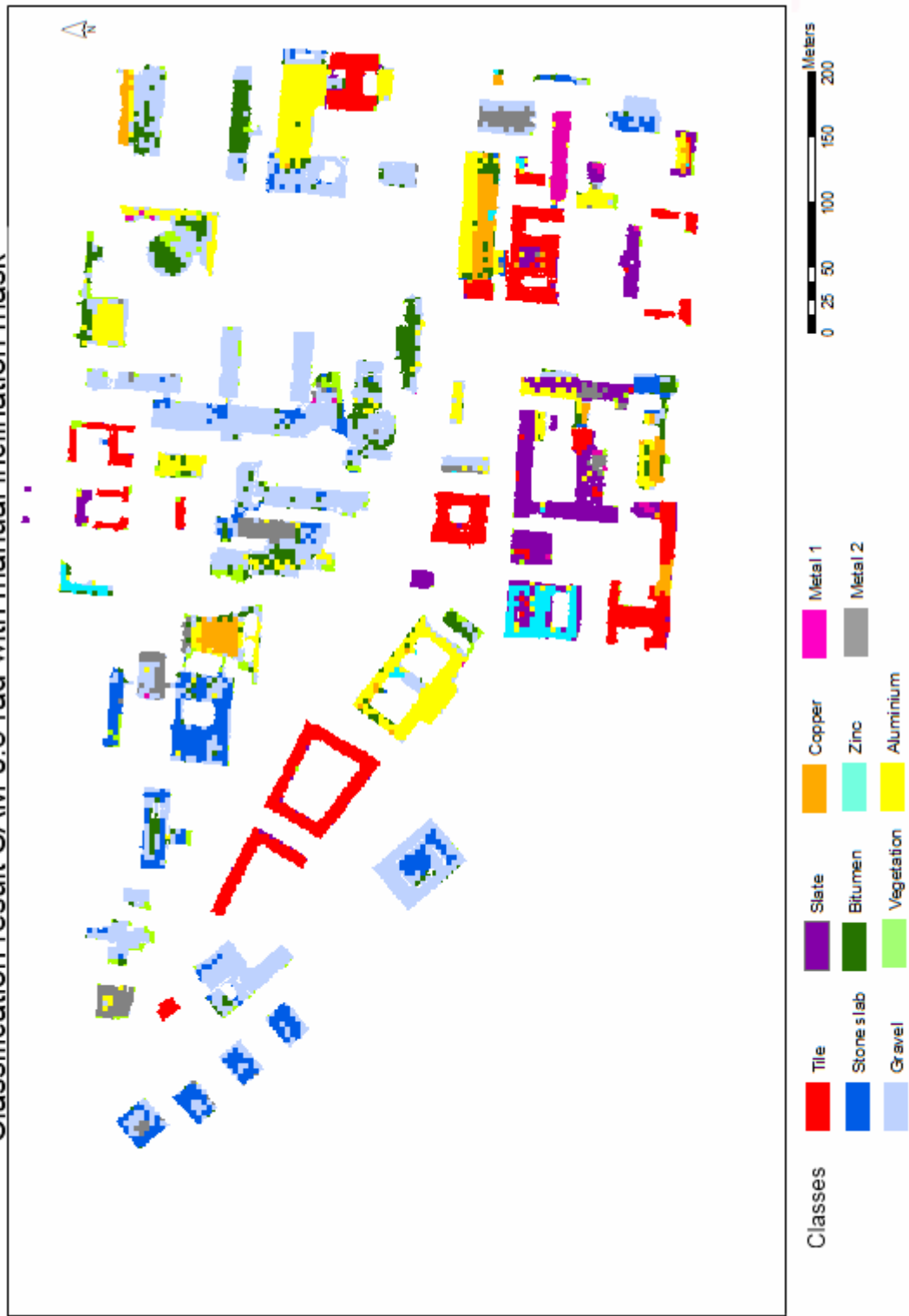
Roof surface map
Classification result SAM 0.5 rad with inclination mask



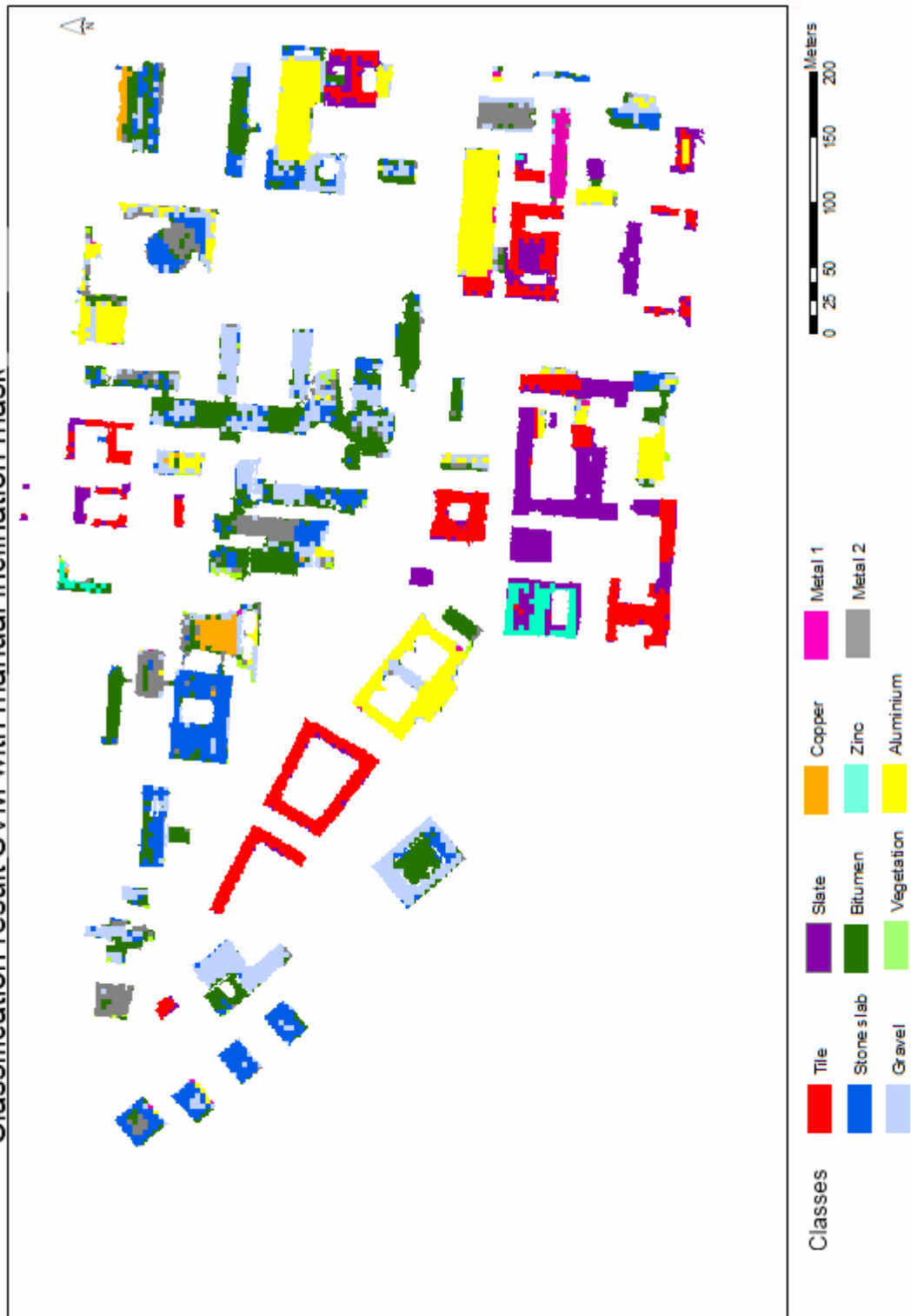
Roof surface map
Classification result SVM with inclination mask



Roof surface map
Classification result SAM 0.5 rad with manual inclination mask



Roof surface map
Classification result SVM with manual inclination mask



B. Statistics of classification results

Statistics of all classification results (sum of pixels and percentage per class):

for original masked hyperspectral dataset:	
number of background pixels	448581
number of roof pixels	151419

for hyperspectral dataset with manual mask:	
number of roof pixels	81811

SAM 0.5 rad		
	Sum of pixels	Percent
Unclassified	0	0,00
Copper	5461	3,60
tile	26990	17,82
stone slab	14102	9,31
zinc	1902	1,26
slate	17752	11,72
gravel	43426	28,66
bitumen	19213	12,68
metal 1	1908	1,26
aluminium	10771	7,11
vegetation	5965	3,94
metal 2	3929	2,59
	151419	100,00

SAM 0.5 rad with inclination mask		
	Sum of pixels	Percent
Unclassified	0	0,00
Copper	6760	4,46
tile	21883	14,45
stone slab	19484	12,87
zinc	2107	1,39
slate	16422	10,85
gravel	42070	27,78
bitumen	15178	10,02
metal 1	2035	1,34
aluminium	14905	9,84
vegetation	5998	3,96
metal 2	4577	3,02
	151419	100,00

SAM 0.5 rad with manual inclination mask		
	Sum of pixels	Percent
Unclassified	203	0,25
Copper	3283	4,01
tile	12762	15,60
stone slab	7123	8,71
zinc	1750	2,14
slate	6771	8,28
gravel	25155	30,75
bitumen	7055	8,62
metal 1	1165	1,42
aluminium	10873	13,29
vegetation	2472	3,02
metal 2	3199	3,91
	81811	100,00

SVM		
	Sum of pixels	Percent
Unclassified	0	0,00
Copper	5804	3,83
tile	22155	14,63
stone slab	16919	11,17
zinc	1812	1,20
slate	35094	23,18
gravel	22858	15,10
bitumen	27144	17,93
metal 1	1145	0,76
aluminium	12458	8,23
vegetation	814	0,54
metal 2	5216	3,44
	151419	100,00

SVM with inclination mask		
	Sum of pixels	Percent
Unclassified	0	0,00
Copper	5046	3,33
tile	20639	13,63
stone slab	16974	11,21
zinc	5646	3,73
slate	21012	13,88
gravel	24325	16,06
bitumen	33503	22,13
metal 1	2395	1,58
aluminium	12241	8,08
vegetation	791	0,52
metal 2	8847	5,84
	151419	100,00

SVM with manual inclination mask		
	Sum of pixels	Percent
Unclassified	0	0,00
Copper	1161	1,42
tile	11647	14,24
stone slab	10869	13,29
zinc	1475	1,80
slate	10270	12,55
gravel	13831	16,91
bitumen	14620	17,87
metal 1	991	1,21
aluminium	10959	13,40
vegetation	643	0,79
metal 2	5345	6,53
	81811	100,00

Statistics of all classification results in reference to the reference areas:

Number of points in reference dataset for each class		
	Sum	Percent
Unclassified		0,00
Copper	1491	2,14
tile	12042	17,30
stone slab	9091	13,06
zinc	2138	3,07
slate	4592	6,60
gravel	21203	30,46
bitumen	3475	4,99
metal 1	852	1,22
aluminium	13785	19,80
vegetation	443	0,64
metal 2	501	0,72
	69613	100,00

SAM 0.5 rad		
	Sum	Percent
Unclassified	144	0,21
Copper	2708	3,89
tile	11118	15,97
stone slab	7423	10,66
zinc	1474	2,12
slate	6512	9,35
gravel	21609	31,04
bitumen	6537	9,39
metal 1	967	1,39
aluminium	8404	12,07
vegetation	1349	1,94
metal 2	1368	1,97
	69613	100,00

SAM 0.5 rad with inclination mask		
	Sum	Percent
Unclassified	144	0,21
Copper	3070	4,41
tile	9772	14,04
stone slab	8567	12,31
zinc	1589	2,28
slate	5042	7,24
gravel	21774	31,28
bitumen	5619	8,07
metal 1	1005	1,44
aluminium	10044	14,43
vegetation	1379	1,98
metal 2	1608	2,31
	69613	100,00

SAM 0.5 rad with manual inclination mask		
	Sum	Percent
Unclassified	144	0,21
Copper	3008	4,32
tile	11785	16,93
stone slab	6731	9,67
zinc	1558	2,24
slate	5422	7,79
gravel	21723	31,21
bitumen	5533	7,95
metal 1	990	1,42
aluminium	9721	13,96
vegetation	1378	1,98
metal 2	1620	2,33
	69613	100,00

SVM		
	Sum	Percent
Unclassified	144	0,21
Copper	1514	2,17
tile	9366	13,45
stone slab	9879	14,19
zinc	1407	2,02
slate	10542	15,14
gravel	13137	18,87
bitumen	9863	14,17
metal 1	759	1,09
aluminium	10788	15,50
vegetation	208	0,30
metal 2	2006	2,88
	<i>69613</i>	<i>100,00</i>

SVM with inclination mask		
	Sum	Percent
Unclassified	144	0,21
Copper	1529	2,20
tile	9616	13,81
stone slab	9498	13,64
zinc	3494	5,02
slate	5964	8,57
gravel	13399	19,25
bitumen	11341	16,29
metal 1	1136	1,63
aluminium	10361	14,88
vegetation	221	0,32
metal 2	2910	4,18
	<i>69613</i>	<i>100,00</i>

SVM with manual inclination mask		
	Sum	Percent
Unclassified	52	0,07
Copper	1038	1,49
tile	10952	15,73
stone slab	9400	13,50
zinc	1311	1,88
slate	8113	11,65
gravel	12503	17,96
bitumen	12001	17,24
metal 1	874	1,26
aluminium	10126	14,55
vegetation	390	0,56
metal 2	2853	4,10
	<i>69613</i>	<i>100,00</i>

C. Confusion matrices of classification results

SAM 0.5 rad

reference \ classification	copper	tile	stone slab	zinc	slate	gravel	bitumen	metal 1	aluminium	vegetation	metal 2	row total	user's accuracy (%)
copper	1148				20				1540			2708	42,39
tile		10669	16		31	15			387			11118	95,96
stone slab	25	735	5138		30	1407			63	25		7423	69,22
zinc			29	1435					10			1474	97,35
slate	16	14	129	423	3099	632	579	62	1446		112	6512	47,59
gravel	64	104	2973	22	395	16512	480		1020	23	16	21609	76,41
bitumen	83	396	414	140	579	1662	2065		1122	76		6537	31,59
metal 1					148	29		790				967	81,70
aluminium	151		111	98	147	187	153		7525		32	8404	89,54
vegetation	2	108	98	11	106	303	191		246	264	20	1349	19,57
metal 2			128	9	31	423			416	45	316	1368	23,10
column total	1489	12026	9036	2138	4586	21170	3468	852	13775	433	496	69469	
producer's accuracy (%)	77,10	88,72	56,86	67,12	67,58	78,00	59,54	92,72	54,63	60,97	63,71		

overall accuracy: 70,48 % Kappa: 0,64

SVM

reference classification	copper	tile	stone slab	zinc	slate	gravel	bitumen	metal 1	aluminium	vegetation	metal 2	row total	user's accuracy (%)
copper	1060	229		67	31				127			1514	70,01
tile		9051			28	26	16		245			9366	96,64
stone slab		1054	4961	21	26	3617	92		77	31		9879	50,22
zinc	24	44		1253					86			1407	89,05
slate	167	222	727	578	3119	3116	1448	86	958	53	68	10542	29,59
gravel	28	306	1089	49	312	9238	191	62	1695	143	24	13137	70,32
bitumen	194	928	2009	143	971	3983	1312		270	53		9863	13,30
metal 1			20			4	8	704	23			759	92,75
aluminium		164	52		60	308	358		9846			10788	91,27
vegetation		13	4			21	29		58	83		208	39,90
metal 2	16	15	174	27	39	857	14		390	70	404	2006	20,14
column total	1489	12026	9036	2138	4586	21170	3468	852	13775	433	496	69469	
producer's accuracy (%)	71,19	75,26	54,90	58,61	68,01	43,64	37,83	82,63	71,48	19,17	81,45		

overall accuracy: 59,06 %

Kappa: 0,52

SAM 0.5 rad with inclination mask

reference classification	copper	tile	stone slab	zinc	slate	gravel	bitumen	metal 1	aluminium	vegetation	metal 2	row total	user's accuracy (%)
copper	1158	70	5		32	50	6		1749			3070	37.72
tile		9559	103		53	5	24		28			9772	97.82
stone slab	25	1899	5044		22	1401			151	25		8567	58.88
zinc			54	1455	4				76			1589	91.57
slate		163	51	381	3230	385	141	4	687			5042	64.06
gravel	64	30	2988	34	416	16528	669	16	990	23	16	21774	75.91
bitumen	71	175	401	89	127	1603	1984		1093	76		5619	35.31
metal 1					160	47		790	8			1005	78.61
aluminium	169	8	148	156	402	318	453	42	8269		79	10044	82.33
vegetation	2	122	98	11	109	303	191		259	264	20	1379	19.14
metal 2			144	12	31	530			465	45	381	1608	23.69
column total	1489	12026	9036	2138	4586	21170	3468	852	13775	433	496	69469	
producer's accuracy (%)	77,77	79,49	55,82	68,05	70,43	78,07	57,21	92,72	60,03	60,97	76,81		

overall accuracy: 70,05 %

Kappa: 0,64

SVM with inclination mask

reference classification	copper	tile	stone slab	zinc	slate	gravel	bitumen	metal 1	aluminium	vegetation	metal 2	row total	user's accuracy (%)
copper	998	90	32	48	39	19	44		259			1529	65,27
tile		8709	4	12	112	76	4	4	693	2		9616	90,57
stone slab		388	4970	12	3	3874	116		102	33		9498	52,33
zinc	128	10	442	1372	726	582	68	9	157			3494	39,27
slate	152	1096	140	529	2730	473	101	3	729		11	5964	45,77
gravel	28	1066	1095	10	105	9202	194	86	1461	128	24	13399	68,68
bitumen	147	188	2022	136	589	5238	2419	22	473	59	48	11341	21,33
metal 1		302	20		16	4	8	704	82			1136	61,97
aluminium		140	52		23	337	370		9439			10361	91,10
vegetation			4			21	29		56	111		221	50,23
metal 2	36	37	255	19	243	1344	115	24	324	100	413	2910	14,19
column total	1489	12026	9036	2138	4586	21170	3468	852	13775	433	496	69469	
producer's accuracy (%)	67,02	72,42	55,00	64,17	59,53	43,47	69,75	82,63	68,52	25,64	83,27		

overall accuracy: 59,12 %

Kappa: 0,52

SAM 0.5 rad with manual inclination mask

reference classification	copper	tile	stone slab	zinc	slate	gravel	bitumen	metal 1	aluminium	vegetation	metal 2	row total	user's accuracy (%)
copper	1182	73			36				1717			3008	39,30
tile		11576			84	7			118			11785	98,23
stone slab	25	10	5154			1407			110	25		6731	76,57
zinc			54	1435					69			1558	92,11
slate	8	212		439	4016	46			701			5422	74,07
gravel	64		3025	23		16889	696	16	971	23	16	21723	77,75
bitumen	26	29	414	87		1691	2124		1086	76		5533	38,39
metal 1					148	47		790	5			990	79,80
aluminium	182	8	147	134	162	250	457	46	8256		79	9721	84,93
vegetation	2	118	98	11	109	303	191		262	264	20	1378	19,16
metal 2			144	9	31	530			480	45	381	1620	23,52
column total	1489	12026	9036	2138	4586	21170	3468	852	13775	433	496	69469	
producer's accuracy (%)	79,38	96,26	57,04	67,12	87,57	79,78	61,25	92,72	59,93	60,97	76,81		

overall accuracy: 74,95 %

Kappa: 0,70

SVM with manual inclination mask

reference classification	copper	tile	stone slab	zinc	slate	gravel	bitumen	metal 1	aluminium	vegetation	metal 2	row total	user's accuracy (%)
copper	894		16	11		16			101			1038	86,13
tile		10056		12	167	33			684			10952	91,82
stone slab		2	5122	12		4039	130		73	22		9400	54,49
zinc				1302				9				1311	99,31
slate	223	1947		627	4425	32			859			8113	54,54
gravel	28	6	1102	10		9400	194	87	1516	144	16	12503	75,18
bitumen	286	13	2437	155		5824	2575	25	564	69	53	12001	21,46
metal 1		18	20			4	8	707	117			874	80,89
aluminium			52			313	374		9387			10126	92,70
vegetation			22			96	45		111	108	8	390	27,69
metal 2	60		268	9		1446	149	24	373	100	424	2853	14,86
column total	1491	12042	9039	2138	4592	21203	3475	852	13785	443	501	69561	
producer's accuracy (%)	59,96	83,51	56,67	60,90	96,36	44,33	74,10	82,98	68,10	24,38	84,63		

overall accuracy: 63,83 % Kappa: 0,58